Proposal to measure the Gravitational Behaviour of Antihydrogen at Rest
GBAR

The GBAR Collaboration

Contact person:
Patrice Pérez (patrice.perez@cea.fr)

List of Authors

G. Chardin, P. Grandemange, D. Lunney, V. Manea
CSNSM, CNRS : UMR8609 – IN2P3 – Université Paris Sud - Paris XI, France

A. Badertscher, P. Crivelli, A. Curioni, A. Marchionni, B. Rossi, A. Rubbia
IPP, ETHZ, CH-8093 Zürich, Switzerland

V. Nesvizhevsky
Institut Laue-Langevin (ILL), 6 rue Jules Horowitz, F-38042 Grenoble, France

P-A. Hervieux, G. Manfredi
IPCMS, 23 rue du Loess, F-67037 Strasbourg, France

P. Comini, P. Debu, P. Dupré, L. Liszkay, B. Mansoulié, P. Pérez, J-M. Rey, N. Ruiz, Y. Sacquin
IRFU, CEA, Saclay, F-91191 Gif-sur-Yvette Cedex, France

A. Voronin
P. N. Lebedev Physical Institute, 53 Leninsky Prospect, 117924 Moscow, Russia

F. Biraben, P. Cladé, A. Douillet, A. Gérardin, S. Guellati, L. Hilico, P. Indelicato, A. Lambrecht, R. Guérout, J-P. Karr, F. Nez, S. Reynaud, V-Q. Tran
LKB, CNRS : UMR8552 – Université Pierre et Marie Curie - Paris VI – Ecole Normale Supérieure de Paris, France
Université d'Evry Val d'Essonne F-91025, France

A. Mohri, Y. Yamazaki
Atomic Physics Laboratory, RIKEN, 2-1 Hirosawa,Wako, Saitama 351-0198, Japan

M. Charlton, S. Eriksson, N. Madsen, D.P. van der Werf
Department of Physics, Swansea University, Swansea SA2 8PP, UK

N. Kuroda, H. Torii
Institute of Physics, University of Tokyo, 3-8-1 Komaba, Meguro, Tokyo 153-8902, Japan

Y. Nagashima
Department of Physics, Tokyo University of Science, 1-3 Kagurazaka, Shinjuku, Tokyo 162-8601, Japan

Contents

1   Introduction

The Einstein classical Weak Equivalence Principle states that the trajectory of a test particle is independent of its composition and internal structure when it is only submitted to gravitational forces. This fundamental principle has never been directly tested with antimatter. However, theoretical models such as supergravity may contain components inducing repulsive gravity (see for example the seminal paper of J. Scherck [J. Scherk 1979], and the discussion in [Nieto 1991]) thus violating this principle.

We propose an experiment to measure the free fall acceleration of neutral antihydrogen atoms in the terrestrial gravitational field.

The basic features of the proposed experiment were expressed in a letter of intent to the SPSC [Pérez 2007], following the original idea of J. Walz and T. Hänsch [Walz 2004]. The originality of this path is to first produce the ultra-cold $\overline{H}^+$ ion before producing the ultra-cold $\overline{H}$ atom: the ion can be cooled down to μK temperatures (i.e. ms^{-1} velocities, and the excess positron can then be laser detached in order to recover the neutral $\overline{H}$ atom and observe its free fall. This process can be set up to minimize momentum transfer in the vertical direction. The temperature achieved in cooling of the $\overline{H}^+$ ion is the source of the main systematic error. The $\overline{H}^+$ ion is produced through the charge exchange process $\overline{p} + Ps \rightarrow \overline{H} + e^-$, followed by $\overline{H} + Ps \rightarrow \overline{H}^+ + e^-$.

The present collaboration is partly composed of groups already involved in antihydrogen experiments at CERN (RIKEN Atomic Physics Laboratory, Swansea University, University of Tokyo , Tokyo University of Science), with successful experience in antiproton and positron manipulation to produce antihydrogen for physics experiments [ALPHA 2010, ASACUSA 2010]. The groups at ETHZ, Swansea University, Tokyo U. of Science and IRFU have experience in low energy positron and positronium physics. LKB is known for its achievements in atomic physics and metrology, using sophisticated laser systems. The IPCMS group is specialized in theoretical plasma physics but has also developed tools to calculate the reactions involved in this proposal. CSNSM possesses expertise with ion trapping. It collaborates with IRFU to adapt a multi-ring Penning trap from RIKEN to the high flux slow positron beam line based on a small electron linac installed at Saclay. The groups from ILL and from the Lebedev Physical Institute work on measuring quantum gravitational levels of ultra-cold neutrons, a technique which may eventually be adapted to slow $\overline{H}$ atoms.

The proposal is organized as follows. The scientific motivation and the aimed for precision are given in section 2. Section 3 contains an overview of the experimental techniques. Sections 4 to 14 describe in detail each of the experimental steps. The general layout of the experiment is presented in section 15. A preliminary cost estimate and schedule together with the task sharing among participating institutes are given in section 16.

2 Scientific motivation

The Einstein Equivalence Principle is at the heart of general relativity. The validity of the Equivalence Principle for antimatter is a basic scientific question, the interest of which is strongly enhanced by the recent observation of the acceleration of the expansion of the Universe which leads to fundamental questions on gravitation theories. This discovery has triggered very large projects in astrophysics. The introduction of Dark Energy to accommodate the observations leads to difficult questions linked with particle physics. In addition, the Universe matter content seems to be dominated by what is called Dark Matter, but its nature and properties are totally unknown. All these experimental facts suggest that our understanding of gravitation is very incomplete.

The classical Weak Equivalence Principle states that the trajectory of a test particle is independent of its composition and internal structure when it is only submitted to gravitational forces. This principle has been tested to a very high precision by many experiments with a great variety of materials and techniques. However, no direct test has been successfully performed with antimatter, although antiparticles are copiously produced by high energy accelerators. In effect, there exists no direct measurement of the interaction of gravity on antimatter.

Indirect tests of the Equivalence Principle for antimatter have been obtained by comparing the properties of particles and their antiparticles or by arguing about the virtual content of the nuclei of ordinary matter. Two particle-antiparticle systems have been studied in great detail with this aim: comparison of the decay parameters of the K0 and $\bar{\text{K}}$0 [CPLEAR 1999], and the simultaneous measurement of p and $\bar{\text{p}}$ cyclotron frequencies [Gabrielse 1999]. However, all these tests rely upon disputable theoretical hypothesis - refer for example to a review on experiments and theoretical arguments [Nieto 1991]. One should finally note that some authors have published a limit on the mass difference between neutrinos and antineutrinos from the time arrival of events from the 1987A supernova explosion [Pakvasa 1989]. This limit assumes that at least one out of the 19 observed events is due to an electron neutrino, the others being antineutrino diffusions, but this hypothesis could not be demonstrated.

The experimental technique is based upon the original idea of T. Hänsch and J. Walz [Walz 2004] to first produce $\overline{\text{H}}^+$ ions and cool them down to a few tens of μK by sympathetic cooling with cold beryllium ions. Then a laser pulse is applied to detach the excess positron and the measurement of the free fall can take place. Several experiments have been envisaged in the past to measure the free fall of charged antiparticles (with positrons and antiprotons), but the weakness of gravitational forces makes the protection against electromagnetic influences extremely hard, and no measurements were obtained. The measurement with antineutrons could not be made because it is very difficult to sufficiently slow them down. A discussion of the possibility to test gravity on positronium shows that it would be very hard to undertake [Mills 2002].

The next simplest form of antimatter is the antihydrogen atom. The AEGIS collaboration at CERN, aims at the measurement of the gravitational acceleration of $\overline{\text{H}}$ atoms, but with a very different technique from that proposed here [AEGIS 2007]. They plan to directly produce ultracold antihydrogen atoms via collisions of ultracold (mK) antiprotons with Rydberg positronium, while we intend to produce ultra cold antihydrogen atoms after the cooling down of $\overline{\text{H}}^+$ ions.

The measurement requires a copious production of antihydrogen at very low velocities.

This is an experimental challenge that we propose to take up with the method suggested by Hänsch and Walz [Walz 2004]. The sympathetic cooling of $\overline{H}^+$ ions down to less than $100\,\mu K$ is an essential element of the method. The precision on the measurement of the gravitational acceleration of $\overline{H}$ atoms is statistically limited and depends upon the temperature of the $\overline{H}^+$ ions. For example, at $10\,\mu K$, a 1 % precision is obtained with 1500 atoms ; this is the aimed precision for the first stage of the experiment. Once the experiment has been set-up and thoroughly tetsed, it could be obtained in a few weeks of running (see section 13). A longer run would allow a measurement at the 10^{-3} level. In the far future, a technique using quantum gravity levels of $\overline{H}$ atoms could yield even better precision (see section 14).

3   Overview of the experimental technique

The GBAR project objective is a direct measurement of the acceleration (named $\bar{\mathrm{g}}$) of antihydrogen atoms in free fall. Its originality is to realize an installation complex which will produce enough extremely slow antihydrogen $\overline{\mathrm{H}}^+$ ions and then antihydrogen atoms to make the measurement possible.

As mentioned above, the principle of the experiment is to produce ultra-cold $\overline{\mathrm{H}}^+$ ions and then detach the positron in excess to observe the free fall of the neutral atom. The steps needed to perform the gravitation experiment have been proposed in [Pérez 2007]. They are as follows:

- Production of an intense flux of fast positrons (few MeV) from the interactions on a thin tungsten target of a 10 MeV electron beam produced in a small accelerator.

- Selection of the positrons and suppression of the electron and gamma background with a magnetic separator.

- Moderation of the positrons down to a few eV.

- Accumulation of the positrons inside a high field Penning-Malmberg trap, where they cool down to a few meV and are then ejected in less than 100 ns onto a porous silica target to form a dense ortho-positronium cloud.

- Excitation of the positronium to gain a large factor on their cross-section for the production of $\overline{\mathrm{H}}^+$.

- Interaction with the very low energy antiproton beam extracted from the Antiproton Decelerator (AD) followed by the ELENA ring at CERN: this produces antihydrogen atoms and $\overline{\mathrm{H}}^+$ ions.

- Accumulation of the $\overline{\mathrm{H}}^+$ ions and sympathetic cooling down to $10\,\mu\mathrm{K}$.

- Photodetachment at threshold of the excess positron and measurement of the free fall of the antihydrogen atom.

On a longer term, a higher precision on the measurement of $\bar{\mathrm{g}}$ could be reached by doing the spectroscopy of gravitational levels of $\overline{\mathrm{H}}$, in a way inspired by the work done with ultra-cold neutrons (see section 14).

The time needed to accumulate 10^7 slow antiprotons from the AD with its present performance is about 20 minutes. It will be less with the foreseen ELENA ring. To eventually attain a precision on the acceleration of $\overline{\mathrm{H}}$ atoms better than 1 % in a few weeks of beam demands the realization of a positron source producing several 10^8 slow positrons per second. Such a source is being developed by Irfu at Saclay. A prototype has demonstrated the feasibility of such a source [Pérez 2010].

Table 1 below summarizes the expected performance and efficiency of each step. The values given will be explained in the following sections. We only comment briefly here on the various steps:

The electron linac characteristics are based on the experience acquired with the demonstrator (see section 4). The main improvement needed is a higher energy to obtain a higher positron yield.

The slow positron production is discussed in section 5. It is necessary to moderate positrons to very low energies to capture and accumulate them. The moderation efficiency is an important parameter in the process. It will be measured with the existing demonstrator using a tungsten moderator downstream of the target. The aimed efficiency is 5×10^{-4}. A solid neon moderator may bring this value above 10^{-3}.

The direct injection of slow positrons from the linac-selector-moderator system into the existing Penning-Malmberg trap should allow storing of some 2×10^{10} positrons. Indeed, the storage of 2×10^{10} electrons in a potential well of 1 kV, and of some 10^6 positrons in a nearby well of only 50 V, have been demonstrated by the RIKEN group [Oshima 2004]. The aimed positron storage is a realistic extrapolation of the present performances thanks to the positron beam characteristics (see section 6). The development of a new trap with high field (potential well of 10 kV) should allow storing of some 10^{11} positrons. The design and realization of such a high field trap is financed in the framework of the ANR POSITRAP project [Pérez 2010].

The efficiency of positronium extraction from porous silica samples has been demonstrated at low intensity at CERN [Liszkay 2008], and at an instantaneous intensity about 10^{11} times higher at UCR in the USA [Cassidy 2010] (section 8). This intensity is the maximum intensity which can be obtained presently with a radioactive source, although it is still about 100 times lower than the goal here. Further developments are planned at Saclay. The positronium cloud characteristics and the reaction chamber in which positronium interacts with the antiprotons are described in section 8.

The antihydrogen production cross section from the interaction of antiprotons with positronium is increased by a factor of around n^4, where n is the principal quantum number of the excited positronium state. However, since the aim is to maximize the $\overline{H}^+$ production, the n value needs to be optimized, as well as the energy of the incident antiprotons, because the $\overline{H}^+$ production proceeds in two steps: $\overline{p} + Ps \rightarrow \overline{H} + e^-$, followed by $\overline{H} + Ps \rightarrow \overline{H}^+ + e^-$. Various possibilities for the deceleration of antiprotons are discussed in section 7. The estimation of the values of the cross-sections of the $\overline{H}^+$ production reactions is given in section 9, and the excitation of Ps is described in section 10.

The cooling of $\overline{H}^+$ ions down to $10\,\mu K$ needs a dedicated development, although the technique has been demonstrated with heavier ions at low energy: the proposed method is to continuously laser cool beryllium ions in a Paul trap, such that sympathetic cooling then occurs for $\overline{H}^+$ ions introduced in the same trap (see section 11). After the cooling process, a laser pulse at threshold is produced to detach the excess positron (section 12), and the free fall measurement follows (section 13). The estimated efficiencies of those steps lead to a useful $\overline{H}$ atom rate which allow s a 1 % measurement of $\bar{g}$ in a few weeks of running. The realization of a more efficient positron moderator and of a higher field trap for the storing of more positrons, as mentioned above, would increase this rate by a large factor, since it varies as the square of the positron rate, allowing a higher precision on $\bar{g}$.

Electrons

Linac frequency	300 Hz	Mean current	0.2 mA	Pulse current	0.33 A
Pulse duration	2 µs	Electrons per pulse	4.2×10^{12}	Electron rate (s^{-1})	1.25×10^{15}

Positrons

Production efficiency (at 10 MeV)	5.5×10^{-4}	Transport efficiency	80 %
Fast positrons per pulse	1.8×10^{9}	Fast positron rate (s^{-1})	5.5×10^{11}
Moderation efficiency	5×10^{-4}	Slow positrons per pulse	9.2×10^{5}
Slow positron rate (s^{-1})	2.8×10^{8}		

Positron storage

Trapping efficiency	70 %	Injection time	110 s	Stored positrons	2.1×10^{10}

Positronium

Production efficiency	35 %	Tube section	1 mm^2	Tube length	1 cm
Positronium density	7.4×10^{11} cm^{-3}	Loss fraction from Ps decay	0.5		

Antihydrogen positive ions

Antiprotons per pulse	6×10^{6}	Deceleration and bunching efficiency	80 %
Production cross section of the $\overline{H}$ atom	4.4 10^{-16} cm^2	Production cross section of the $\overline{H}^+$ ion	8.8 10^{-15} cm^2
$\overline{H}$ per pulse	3.9×10^{2}	$\overline{H}^+$ per pulse	0.32

Antihydrogen atoms

$\overline{H}^+$ Trapping efficiency	100 %	Cooling efficiency	70 %
cold $\overline{H}^+$ per pulse	0.2	Photodetachment efficiency	99 %
Detector acceptance	65 %	$\overline{H}$ events per pulse	0.14
$\overline{H}$ event rate (s^{-1})	1.3×10^{-3}		

Table 1: Expected efficiencies and performances.

4 Production of fast positrons

The positrons needed for the production of positronium are obtained in two steps. The first step is the creation of positrons, in which they are emitted with a large range of kinetic energies. The second step is the moderation of the positrons, in order to guide and trap them efficiently inside the accumulation trap. Due to the large uncertainty in the moderation efficiency for positrons produced with an accelerator, the number of fast positrons before moderation should be close to 10^{12} e^+s^{-1} for this experiment.

In order to study the fast positron production, a demonstrator facility has been developed at Irfu (Saclay).

4.1 The SOPHI-SELMA demonstrator

4.1.1 Principle

The production of positrons is based on the e^+e^- pair creation process induced by energetic electrons striking a thin target made of high Z material. The pair production cross section increases almost exponentially above the threshold of at 1.2 MeV, but for radiological safety it has been chosen to restrain the beam energy to below 10 MeV (see 4.1.2). The low cross-section is then compensated by an increase of the beam current, within the limits given by the increase of the temperature of the target. The fast positrons (1 MeV energy on average) emitted from the target then impinge upon a moderator to produce the required slow positron beam (few eV energy, see section 5). A magnetic system has been designed to guide positrons onto a region where a solid neon moderator could be installed in order to reach moderation efficiencies of order 10^{-3}. This is an option to increase the nominal rate of slow positron production (see section 5).

4.1.2 The accelerator

For the development of the high intensity positron source, a linac of type LINAX5 has been bought from the Linac Technologies Company (now Getinge). This device is dubbed SELMA (*Source d'électrons pour les matériaux et l'antimatière*). The energy has been chosen such that no material activation occurs, the beam energy being below the neutron production threshold in the surrounding material (concrete). Its main characteristics are:

- Maximun beam energy: 5.5 MeV

- Beam current: 0.15 mA

- Maximum repetition rate: 200 Hz

- Pulse duration: 2 to 4 µs

- Beam size: 1 mm r.m.s. at the exit of the accelerator section

- Beam current stability: ± 3%

A picture of the accelerator is shown in Fig. 1.

The accelerator section is made of 5 cavities working with progressive waves at 3 GHz on pi mode. The RF power is provided by a magnetron (MG5193 from E2V) giving a

Figure 1: The 5.5 MeV demonstrator accelerator.

peak power of 2.3 MW. The exit beam tube of the linac is connected to a vacuum vessel containing the target, around which a magnetic field is created for positron filtering. The linac box has been shielded with iron plates to suppress the fringe field induced by the coils of this positron selector device.

4.1.3 Positron production

The positron production target is a thick (1 mm) tungsten sheet, perpendicular to the beam. It allows a reduced electron background in the fast positron detector described in section 4.2.1. A simulation of the positron production has been made using GEANT3. The positron production efficiency given by the simulation is 1.5×10^{-4} per incident electron for a 5.5 MeV energy. The energy spectrum of the positrons at the target is given in Fig. 2, where the forward and backward components are separately shown.
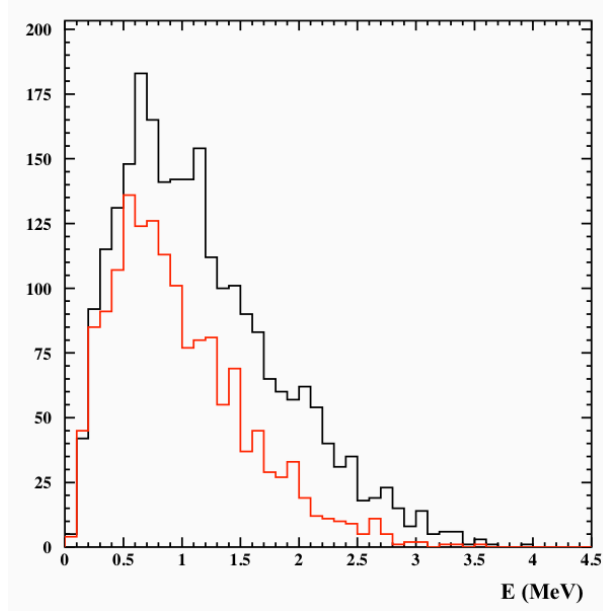
Figure 2: Simulated distribution of the kinetic energy (E) of the positrons produced at the target. In black: positrons emitted in the forward direction; in red: positrons emitted in the backward direction. The vertical scale has arbitrary units.

4.1.4 Magnetic system (SOPHI)

The magnetic field of the SOPHI device (*SOurce de Positons de Haute Intensité*) is designed to help capture the emitted positrons in the target region, to guide them to a dipole field arrangement which charge separates the electrons and positrons, and eventually channel the selected positrons up to the output of the filter, where the moderation can occur. The fields are optimized to select the positrons at the energy where they are the more abundant, i.e. around 1 MeV. The SOPHI magnetic system is composed of a succession of solenoid coils fulfilling the desired task. A first coil, H1, is positioned before the target and helps to channel the electron beam. Behind the target, two coils H2 guide the particles up to the dipole area. The dipole is made of two coils, D1 and D2, of the same type as H2. Then in the direction of the positron deviation, two more coils of H2 type guide the particles up to the output of SOPHI (Fig. 3).

The magnetic field in the dipole area is not a uniform dipole as in standard high energy beam lines. Here the field is weak, a few tens of millitesla. The distortion of the magnetic field lines is enough to eliminate the electrons, whilst maximizing the number of transmitted positrons, owing to their large energy dispersion. The electrons are deviated to the wall of the vessel, and the positrons towards the last H2 guiding coils. The trajectories of the electrons and positrons after the target have been simulated, and the transmission efficiencies up to the exit of the device are given in table 2.

The SOPHI set-up is shown in Fig. 4, before its installation in front of the linac in March 2008. The H1 coil (copper red) is the first on the left (viewed from the side). The D1 coil is clearly visible, and the last H2 coils are seen horizontally above D1. The small tubes in the front distribute the cooling water inside the coils.
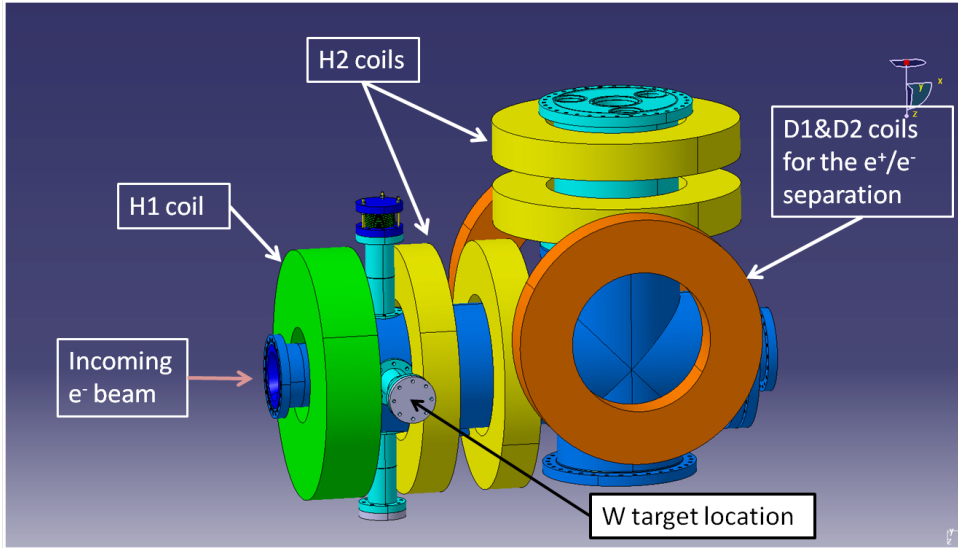
Figure 3: Arrangement of the coils in the SOPHI facility.

Particles/energy range	Efficiency
e^+ (0-1 MeV)	70%
e^+ (1-2 MeV)	76%
e^-	$\leq 10^{-4}$

Table 2: Transmission efficiencies between target and output.
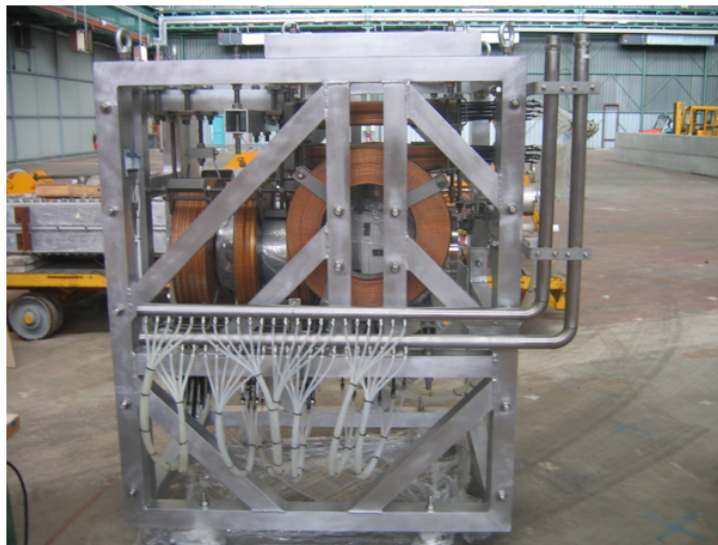
Figure 4: Photograph of the SOPHI device before its installation in front of the linac.

4.2 Results on beam characteristics

4.2.1 Fast positron detection

The fast positron flux produced in SOPHI has been measured using a robust pad detector. This detector is made of 37 aluminium pads ($37 \times 37\,\text{mm}^2$, 5 mm thick) and is located inside the SOPHI vessel, on the exit flange (see Fig. 5a), at the level of the last H2 coil. A grid in front of the pads helps reduce the number of low energy electrons reaching the pads. The charges collected on each pad are read-out with fast ADC's located behind the flange, inside a shielded box. Thorough care has been necessary to ensure an appropriate background level for the charge measurement, accounting for the high gamma ray background, the HF waves emitted by the nearby magnetron linac, and the important electrical power return to the ground.

A GEANT4 simulation of the positron production and transport shows that the positron charges are concentrated on two pads around an eccentric point of the detector, which has effectively been observed. Fig. 5b shows a typical pulse measured on two adjacent detector pads.

a)   b)
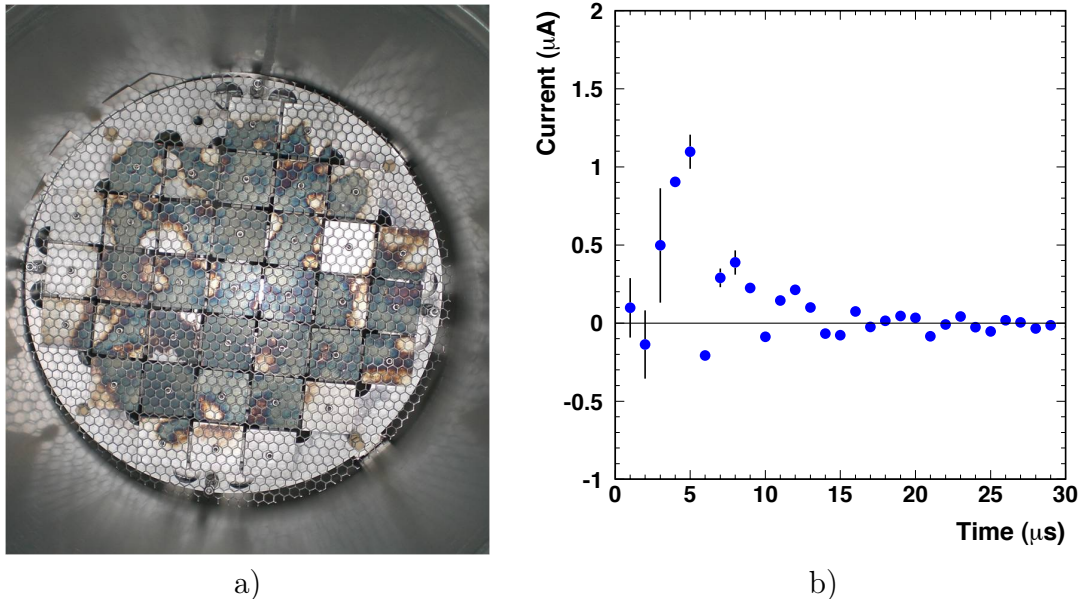
Figure 5: a) Photograph of the pad detector from inside the vessel. The pads are visible behind the grid. b) Highest positron signal collected on adjacent pads. On this scale, one microampere corresponds to 1 picocoulomb.

The maximum positron charge measured on two adjacent pads amounts to about 3.5 pC, which is a factor 5 to 6 below expectations from the nominal performance of the linac. We observed that this charge did not increase linearly with the beam intensity. This has led us to suspect that the actual beam energy was significantly varying with its intensity. This is addressed in the following section.

4.2.2 Beam energy and intensity

A measurement of the beam energy has been conducted using a high precision magnetic spectrometer developed for the AIRIX accelerator within CEA [AIRIX 1993]. The spectrometer measures the evolution of the beam energy during the 4 μs pulse and gives access to the maximum beam energy, as well as to the rise and fall time of the energy within the pulse. The e$^-$ beam energy at different beam intensities is shown in Fig. 6. The measurements show that the beam energy is only 4.3 MeV (see Fig. 6a) at a mean current of 0.11 mA (corresponding to a 140 mA intensity during the pulse). Such a performance gives a prediction of a fast positron intensity in good agreement with our measurement.

a)   b)
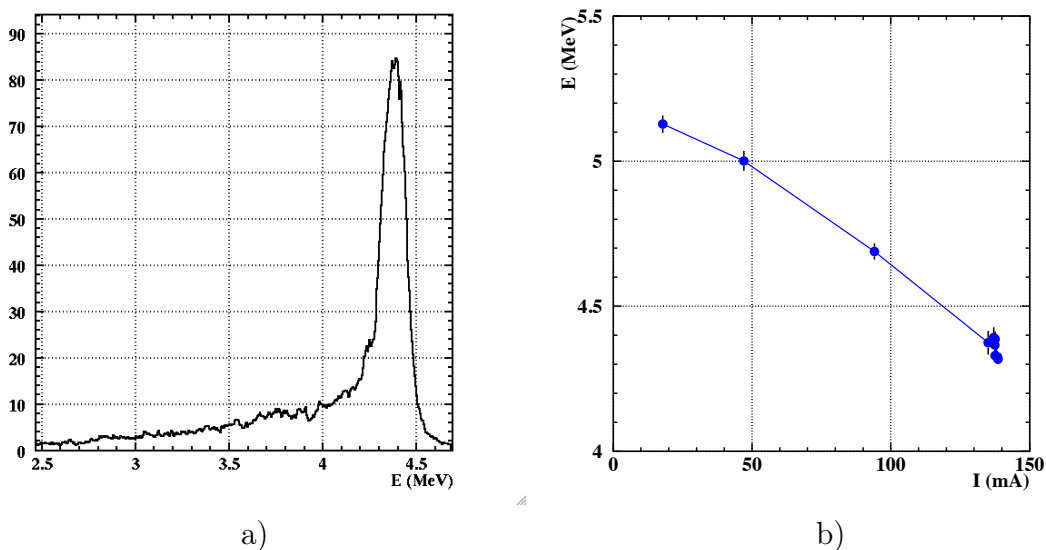
Figure 6: a) Measured spectrum of the beam energy (E) at maximum intensity (the vertical scale is in arbitrary units); b) Peak beam energy as a function of the beam intensity (I) during the pulse.

Because the positron production cross section varies rapidly with the incident electron energy, and since the demonstrator linac energy decreases with intensity, the maximum positron flux achievable with this machine would be obtained with a mean electron current of 0.072 mA (90 mA peak current for 4 μs pulses at 200 Hz). At this intensity, the beam energy is about 4.7 MeV and the positron yield is 7.5×10^{-5}. This leads to a flux of 3.4×10^{10} fast e$^+$s^{-1}.

4.3 Future Linac for the experiment at CERN

The required positron flux to store close to 10^{11} positrons during one cycle of the AD/ELENA complex for the GBAR experiment (see section 3) is not feasible with the present linac. Based on the experience acquired with the demonstrator, the main improvements required for the final apparatus are:

- Maximum possible energy, but staying below 10 MeV, so as to prevent radio activation of materials.

- Higher frequency, about 300 Hz. This parameter is limited by the cooling time of the positrons inside the trap (see section 6).

- Pulse duration reduced to about $2\,\mu s$ to improve the efficiency of the necessary bunching to 80 ns (see section 6).

If enough resources are available, a new machine will be bought from industry. Another possibility will be to upgrade the demonstrator to the maximum possible energy.

5 Production of slow positrons

The positron trap will be loaded with a low energy (< 200 eV) positron beam. A tungsten moderator (stacked tungsten meshes), placed immediately behind the primary positron source, will convert the fast (1 MeV) positrons form the electron target into slow ones, with an expected efficiency of 5×10^{-4}. Transport of particles between the linac-based positron source and the positron trap will be made at low energy, using a longitudinal magnetic field of approximately 8 mT.

5.1 Slow positron beam

Primary positron sources, either based on radioactive decay or pair production, deliver particles with a large energy distribution. In the case of the β^+ decay of the most frequently used ^{22}Na based positron sources, the mean value and maximum of the energy distribution are 182 keV and 546 keV, respectively. The proposed accelerator based positron source of the GBAR project will deliver positrons with a mean kinetic energy of approximately 1 MeV. The energy spectrum extends to more than 3 MeV. Transport and injection of positrons from the linac-based source into the high field positron trap is not possible at this high kinetic energy without considerable loss of intensity, due to the low luminosity of the positron beam created in the electron target. Furthermore, capture of e^+ in the high field trap requires an e^+ beam with low kinetic energy.

The technology to generate and transport what are designated as **slow positrons**, i.e. positrons of energies in the eV to a few keV range, has been developed mostly for the use in slow positron beam-based spectrometers [Schultz 1988]. It is based on the use of moderator materials, which re-emit few eV positrons when they are irradiated by high energy positrons. In the design of the positron source for the GBAR project we will use existing technology. A novel feature of the positron source will be the use of a *low energy* accelerator for the positron generation. In a separate research and development project, we are also working on the construction of a novel solid neon based moderator, in order to increase the attainable moderator efficiency. The baseline design for the HBAR project is a tungsten moderator, installed near the primary positron source.

5.2 Positron moderation

The most efficient way to produce low energy positrons from the primaries in the 100 keV - 1 MeV energy range is by using positron moderators. Solids with negative work function for positrons can be used for this purpose. After implantation into the moderator material, fast positrons first slow down to thermal energy (thermalization). A small part of the thermalized positrons, during their thermal diffusion, can return to the surface before annihilation with an electron of the material. Once at the surface, a significant fraction of the e^+ may be emitted into the vacuum with an energy that corresponds to the work function (typically a few eV). The overall efficiency of the moderation depends on the material, the concentration of positron traps (vacancies, grain boundaries etc) in the bulk, the state of the surface (concentration of surface defects, contamination), the temperature and the incident energy. The moderation efficiency is in the range 10^{-4}-10^{-3} in the case of the most frequently used tungsten moderators but it can reach 10^{-2} for solid neon moderators in optimal configuration.

5.3 Materials used for positron moderation

The most widely used moderator material is tungsten. Its high density ensures that a relatively large portion of the implanted fast positrons reach thermal energy within the range of the diffusion length from the surface. After annealing at high temperature (at 1800 °C or above), the oxidized tungsten surface shows stable moderator efficiency in ultra-high vacuum (less than 10^{-8} mbar). No significant loss in the efficiency is found even after a brief exposure to atmosphere during the transfer between the vacuum chamber used for annealing and the positron source chamber. The moderator efficiency is stable; tungsten moderators have been reported to function for years in a vacuum of 1×10^{-7} mbar. The energy spread of the moderated positrons depends on the quality and contamination of the surface. To maintain a narrow energy distribution, periodic, *in situ*, annealing at high temperature and very good vacuum conditions are needed (Fig. 7).
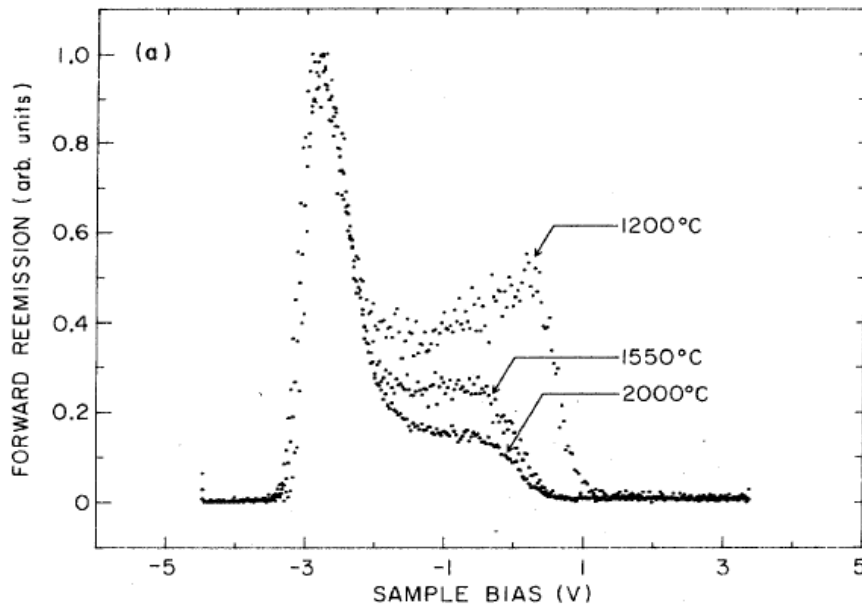
Figure 7: Energy distribution of moderated positrons at a tungsten moderator, after *in situ* annealing at various temperatures in vacuum [Chen 1985]. The kinetic energy of positrons is about $-(e \times \text{bias voltage})$.

Tungsten moderators have been used in slow positron beam systems in different geometries. High quality single crystal moderators in reflection configuration (i.e., when the incoming high energy positrons arrive at the same side of the crystal as the moderated low-energy positrons leave) show the highest moderator efficiency, up to 10^{-3}. Thin single crystal foils (less than 1000 nm thick) or polycrystalline foils (4000-5000 nm) are used in many existing installations with relatively good efficiency ($1 - 2 \times 10^{-4}$). Recently, good moderator efficiency (10^{-3}) was reported using electrochemically etched thin tungsten grids, with $10\,\mu$m wire thickness [Saito 2002], as illustrated in Fig. 8. Linac-based or reactor-based positron sources used complex forms (e.g. venetian blind structure or grid) as moderators, usually assembled from thin polycrystalline foils. The
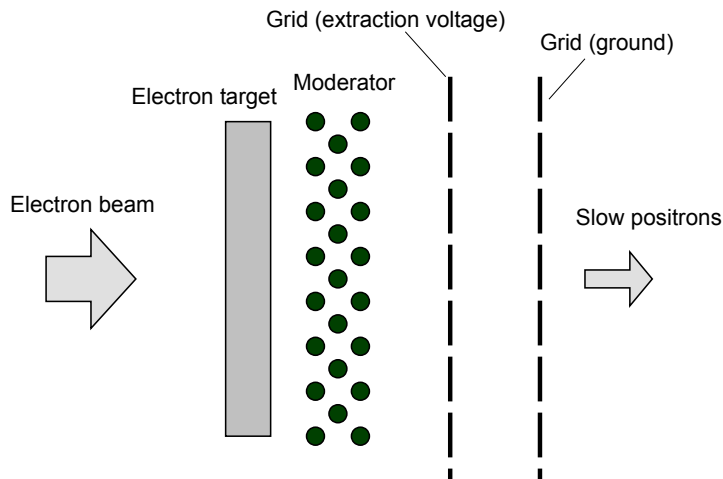
Figure 8: Schematic drawing of a positron moderator made of stacked tungsten meshes.

high intensity positron source at the FRM-II research reactor at Garching (Germany) applies a moderator structure made of platinum, a metal that can be reconditioned at moderate temperature, which is an asset at the working environment near the reactor core. However, platinum moderators are less efficient than tungsten ones in the same geometry.

The highest moderator efficiency attained to date uses solid neon moderators at approximately 7 K temperature. Being an insulator with a large band-gap, the mechanism of positron moderation in neon is different from that of metals. Positrons with an energy below the band-gap value ($E_g = 21.58$ eV) lose energy only through phonon scattering, a process which is far slower than the electron excitation in the same energy range in metals. Many positrons reach the moderator surface before attaining thermal equilibrium. Consequently, the energy distribution of the emitted slow positrons depends on the depth distribution of the implanted fast positrons, i.e. the energy distribution of the primary positron source. With an optimized geometry and a ^{22}Na positron source, up to 1 % moderator efficiency has been reported using solid neon. As the energy of the emitted positrons is determined by the scattering process and not by the positron work function, the energy spread of the moderated positrons in neon is larger than the spread for tungsten (Fig. 9). Solid neon moderators require periodic regeneration of the neon film. The reason is contamination from the imperfect vacuum. Typically, the film has to be regenerated daily.

5.4   Positron moderators in linac-based slow positron sources

The target zone of a linear electron accelerator is a hostile environment for positron moderators. As the most robust and stable moderator material, tungsten has been used in all linac-based slow positron sources to date. The geometry used in these systems is usually a venetian blind structure, often made of relatively thick tungsten foils ($25 - 50\,\mu$m). The advantage of this structure is that most of the moderation takes place in reflection configuration, giving a significantly higher moderation efficiency than that

16
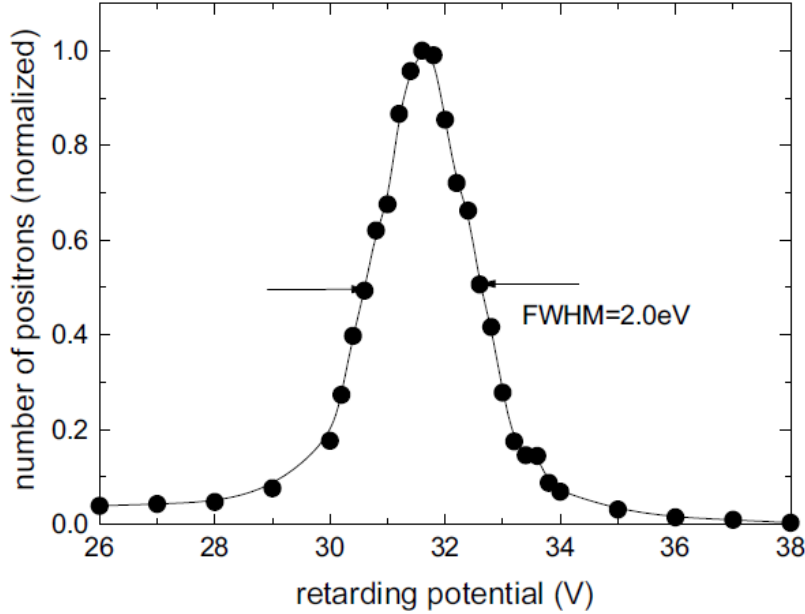
Figure 9: Energy distribution of moderated positrons after a solid neon moderator [Wu 2007].

of the transmission configuration even for very thin (100-1000 nm thick) tungsten foils. The cooled electron target of most linac-based systems puts constraints on the possible geometry of the target-moderator assembly and it is often difficult to access. The primary positron beams in typical linac systems provide slow positrons with relatively large beam diameter (a few cm), rather broad angular spread and broad energy distribution.

Table 3 lists the performance of linac-based slow positron sources realized in the past or in use. As a figure of merit the number of slow positrons is given per electron of the linac beam. The large scattering in the performances show that, in many systems, the electron target / positron moderator assembly was not optimized for efficiency but the construction was influenced by other constraints. At the low electron energy limit, an efficiency of 1.35×10^{-7} was found in a laboratory of Mitsubishi (Japan), for a 18 MeV electron beam [Tanaka 1991].

The moderator efficiency is affected by the very hostile environment in the vicinity of the electron target that is the point of creation of the fast positrons. Point defects may be created in the metal, leading to a shorter effective diffusion length of positrons in the moderator and thereby to lower moderator efficiency. In the case of high energy linacs, defects can also be created by neutrons created in the target. Positron emission from the moderator surface may be hindered by carbon precipitation on the surface, which is reportedly enhanced in the vicinity of the electron target [Suzuki 1998].

There is scant quantitative information on the deterioration of the moderator efficiency in linac-based positron sources. Suzuki et al. found one order of magnitude loss after 1000 hours of irradiation in a system based on a 70 MeV linac [Suzuki 1998]. The moderator efficiency could be partly recovered by annealing the tungsten moderator at 1000 °C in low pressure oxygen. This treatment removes the carbon precipitation from the surface.

Laboratory	Ref.	Electron energy	Slow e^+ / e^-
Livermore	[Howell 1987]	100 MeV	16×10^{-7}
Mainz	[Ley 1985]	120 MeV	3×10^{-7}
Oak Ridge	[Hulett 1989]	180 MeV	0.53×10^{-7}
Giessen	[Ebel 1987]	35 MeV	0.4×10^{-7}
Gent	[Paridaens 1990]	40 MeV	0.32×10^{-7}
Tsukuba (ETL)	[Suzuki 1998]	75 MeV	2×10^{-7}
Mitsubishi	[Tanaka 1991]	18 MeV	1.35×10^{-7}

Table 3: Efficiency of slow positron production at various linac-based positron sources.

To remove the point defects or voids created by irradiation, annealing at 1800 °C or higher is needed.

5.5   Positron moderation for the GBAR experiment

In the moderator installation of the experiment a high efficiency moderator made of a stack of electrochemically etched thin tungsten grids will be used as the tungsten structure that promises the highest moderator efficiency. Its efficiency will be compared with moderators made of thin polycrystalline and/or single crystal foils in transmission geometry. A tentative value of 5×10^{-4} has been taken for the moderation efficiency in table 1.

The energy of the primary electron beam which will be used in the GBAR setup is significantly lower than the electron beam energy in all linac-based slow positron sources constructed so far. The GBAR linac will be a compact, dedicated system, embedded in the experimental area, which does not generate radioactive contamination in the target zone. It provides better accessibility to the electron target and the moderator structure. Consequently, it will be easier to test and validate various moderator structures, materials and complex electron target / moderator assemblies in order to find the most efficient and stable configuration. Development work to improve the slow positron source is planned during the construction phase of the experimental setup.

In the final installation of the GBAR experiment, the electron target zone and the slow positron transfer line will be designed in a way that allows the use of both tungsten and solid neon moderators. Predictably, a large improvement in efficiency could be reached by using solid neon as moderator material. The cryogenic temperature of 7 K necessary for this moderator cannot be attained in the vicinity of the electron target. The fast positrons generated in the electron target can be separated from the much larger flux of electrons by a magnetic system suggested by Perez et al. [Pérez 2004]. A prototype of the magnetic system is installed in Saclay, on a small linac (see section 4). Work has also been started to develop a prototype for the solid neon-based slow positron source. However, the experimental setup described in the present Proposal is based on the assumption that an optimized tungsten structure will be used as moderator.

5.6   Slow positron production efficiency

The production efficiency of fast positrons at the electron target is approximately 5.5×10^{-4} positron for each incoming electron, calculated using a Monte-Carlo simulation for 10 MeV electrons. The estimated value of the moderator efficiency is 5×10^{-4}. The total slow positron production efficiency is the product of these two values, namely around 3×10^{-7} slow positrons for each electron.

O'Rourke *et al.* simulated positron production and moderation for a positron source which uses a 70 MeV linac, installed in Tsukuba, Japan [O'Rourke 2011]. The efficiency given by simulation was scaled to fit the observed value (Fig. 10). For 10 MeV electron energy, the extrapolated curve gives 4×10^{-8} positrons for each electron. The moderator structure of the GBAR experiment will have a significantly higher efficiency than that used in Tsukuba. The tungsten mesh, with $10 - 20\,\mu\mathrm{m}$ wire thickness, has significantly higher specific surface than the $50\,\mu\mathrm{m}$ thick tungsten plates. The higher specific surface increases the moderator efficiency, since the moderation is based on near-surface effects. Furthermore, smaller thickness means that a positron may cross several surfaces before an annihilation or moderation event. The solid angle associated with tungsten in stacked grids is also larger than for plates placed parallel to the beam direction. Finally, annealing of the thin grids can be more complete than the heat treatment of relatively thick tungsten plates. We estimate that up to ten times higher slow positron efficiency can be expected in the GBAR source, which can then provide up to 3×10^{-7} positrons for each 10 MeV electron. The long time stability of the moderator effect is expected to be better at the low energy electron beam of GBAR than that observed in Tsukuba: the energy of electrons scattered by the target is too low to create point defects in the tungsten moderator. Furthermore, there are no neutrons which could also damage the crystal structure.

5.7   Slow positron transport line

Slow positrons from the moderator will be transported between the moderator and the positron trap in a low field (8 mT) magnetic transport line. Adiabatic beam transport conditions ensure low intensity loss and limited deterioration of the beam quality. To inject the positrons into the high field (5 T) trap, the magnetic mirror effect between the $B_{transport}$ magnetic field of the transfer line and the very high magnetic field B_{trap} of the trap has to be overcome. In the adiabatic limit, only positrons with $E_{\parallel}/E_{\perp} > B_{trap}/B_{transport}$ will pass the magnetic mirror and enter the trap, where $E_{\parallel}$ and $E_{\perp}$ are the transverse and longitudinal energy, respectively. With transverse energy approximately 1.5 eV, $E_{\parallel}$ has to be in the order of 1 keV so that the positrons can enter the trap. As will be discussed in section 6, the acceleration from the transport energy (10-200 eV) to the keV energy level that is needed to enter the trap will be provided by a pulsed accelerator field. To adjust the time of arrival of slow positrons at the accelerator stage, the moderator potential will be changed in a way that it forms a buncher with a time focus at the accelerator electrodes, as described in section 6.2.
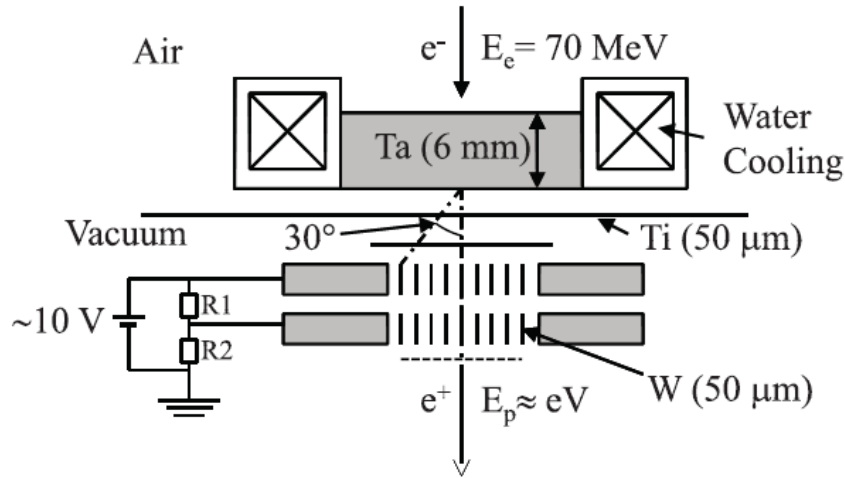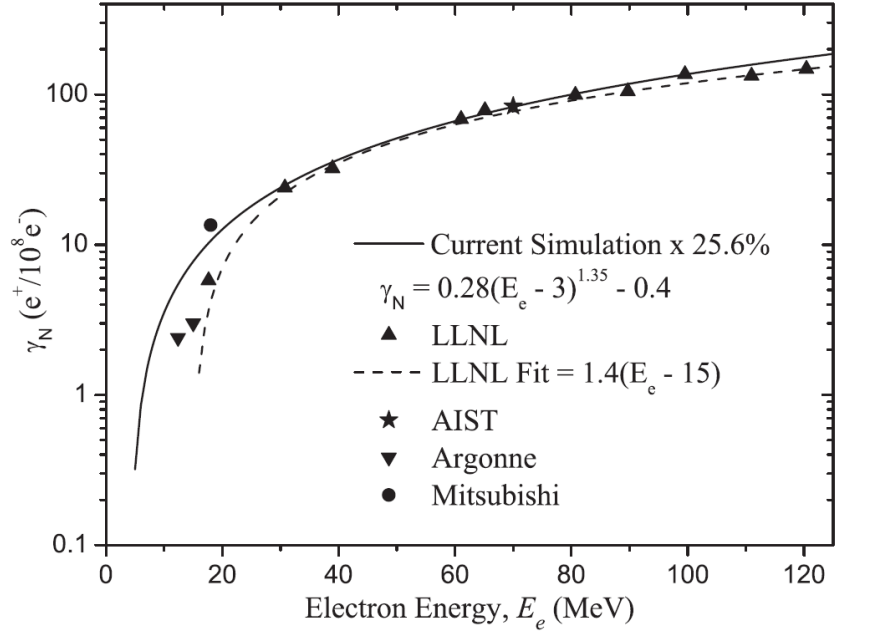
Figure 10: Simulation results for the slow positron production efficiency as a function of the electron beam energy. The simulation results are scaled to fit the efficiency measured at 70 MeV electron energy at Tsukuba. The configuration of the electron target and the moderator, used in the simulation and the measurement is shown below the plot [O'Rourke 2011].
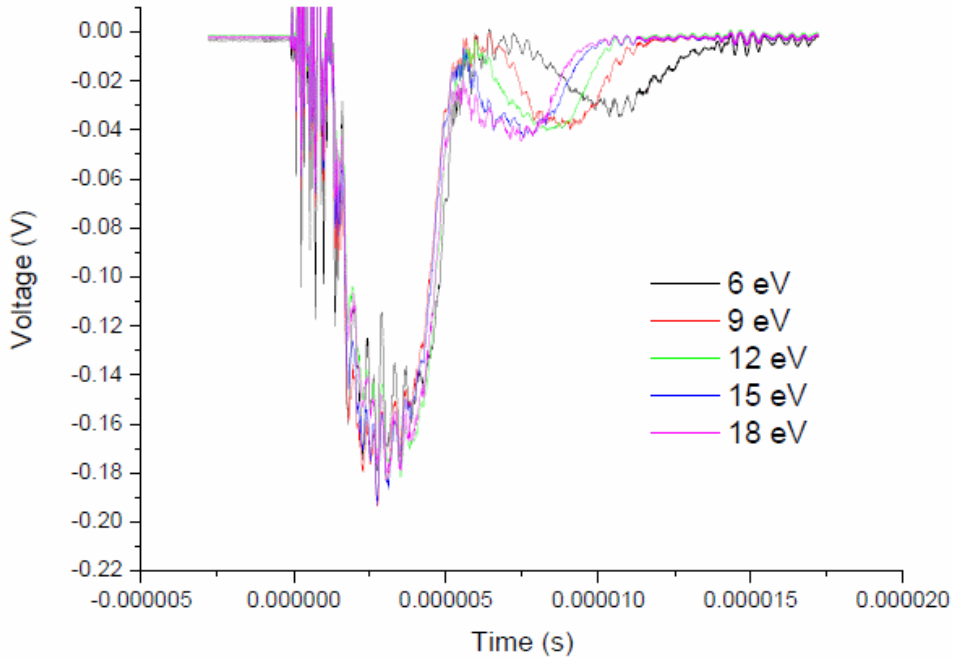
Figure 11: Signal of a scintillation detector at the positron target, outside the radiation shield (see text).

5.8 Observation of the first slow positron signal at the SOPHI-SELMA demonstrator

We have recently observed the first slow positron signal at the linac-based positron source SOPHI-SELMA (see section 4). A single tungsten mesh was used as the positron moderator, after short heating at approximately 2200 K using electrical current flowing through the mesh. The signal of a scintillation detector placed next to an aluminium target outside the radiation shield of the linac is shown in Fig. 11. The curves represent the signal measured at different potentials of the moderator, i. e. at different positron beam energies. The first peak corresponds to gamma radiation from the electron target, leaking through the positron beamline. It does not change significantly with positron energy. The second, smaller peak is identified as signal from 511 keV annihilation gamma photons, created in the aluminum target. The delay between the direct gamma peak and the positron peak depends on the positron energy, reflecting the time of flight (a few µs) of positrons in the transport line . The signal can be unambiguously identified due to slow positrons emitted by the tungsten moderator. Work is underway to improve the moderator efficiency by increasing the number of mesh layers and by improving the annealing procedure.

21

6 Accumulation and ejection of slow positrons

6.1 Description of the method chosen

In order to realize a dense cloud of Ps to serve as a target for antiprotons to produce $\overline{H}^+$ ions, it is necessary to accumulate several 10^{10} positrons and eject them in a short pulse onto an e^+-Ps converter.

The method we propose is to accumulate the slow positrons in the Multi-'Ring Trap (MRT) of the Riken Atomic Physics Laboratory group, in a way inspired by the original scheme demonstrated by some of us [Oshima 2000, Oshima 2004] (Fig. 12).
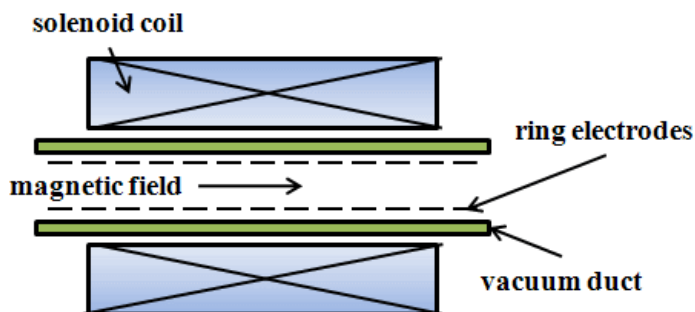
Figure 12: Schematic drawing of a multi-ring trap.

The experimental setup which was used is described in detail in [Oshima 2003], and the MRT in [Mohri 1998, Mohri 2002]. The MRT is embedded in a superconducting magnet to confine the charged particles in the transverse direction. The magnet provides a uniform magnetic field of 5 T over 500 mm. The MRT is made of 27 ring electrodes (21 of 20 mm length equally spaced by 3 mm, 2 of 160 mm and 4 of 270 mm length) allowing the formation of two potential wells along the longitudinal axis, the first one for trapping electrons, the second one for positively charged particles (Fig. 13), so that negative and positive particles can be trapped simultaneously.

The results of Oshima et al. [Oshima 2004] were obtained with the setup we briefly describe now. The slow positron source consisted of a 44 mCi ^{22}Na source and a solid Ne moderator which produced 1.6×10^6 e^+s^{-1}. Due to the magnetic mirror formed at the entrance of the magnet, only 50 % of the positrons were injected into the MRT, because the accelerating entrance voltage was only 500 V. A high density electron plasma ($\simeq 10^{11}$ cm^{-3}) and an ion cloud of H_2^+ had been previously formed in the MRT to slow down the positrons. Downstream of the MRT, the positrons hit a tungsten remoderator and a fraction (13 %) were back-reemitted with a 3 eV energy and a reduced transverse energy distribution (0.2 eV). With a suitable voltage bias on the remoderator, positrons could enter the electron plasma and be sufficiently slowed down to be reflected when they return towards the remoderator after a round trip in the MRT. They were eventually trapped in the second potential well of the MRT, after collisions within the ion cloud. The accumulation efficiency (ratio of positrons hitting the remoderator to trapped positrons) reached 1 %, resulting in the normalized accumulation rate of 3.6×10^2 e^+/s/mCi.

Even with a high activity ^{22}Na source (several tens of mCi) and a higher trapping efficiency, one cannot accumulate several 10^{10} slow positrons in a few minutes. One needs

to gain two orders of magnitude in the positron production rate and reach at least 10 % in the trapping efficiency. This is the reason to accumulate positrons generated with an electron linear accelerator, taking advantage of the pulsed time structure of the beam.

For this purpose, the accumulation process has to be revised. It is expected to be more efficient, since there is no longer need of a remoderator at the downstream end of the MRT. The foreseen scheme is as follows:

- Two potential wells are formed with the ring electrodes to simultaneously store negative and positive particles. The initial wells are 1000 V and 100 V deep respectively (Fig. 14 a).

- An electron gun is moved onto the MRT axis and 2-3 10^{10} electrons are stored in a few seconds. Electrons cool down towards the environmental temperature by synchrotron radiation with a cooling time $\tau[s] \simeq 6/B[T]^2$ [Higaki 2002]. The number of stored electrons has been measured to be proportional to the potential well depth up to 800 V. The mechanism of the accumulation of electrons is described in detail in [Mohamed 2011].

- The electron gun is moved out of the axis.

- Moderated positrons are produced at a varying bias voltage to compress the bunch time (see section 6.2) and guided towards the MRT following 80 mT magnetic field lines. They are reaccelerated to 1 keV to pass the magnetic mirror with close to 100 % efficiency. This is shown by a simulation which has been verified with measurements made with a configuration similar to that of [Oshima 2004] (see Fig. 15). This efficiency depends upon the transverse energy distribution of moderated positrons. The simulation used a Lorentzian function of width 0.6 eV.

- The potential of the entrance electrode is lowered to let positrons enter the magnet (Fig. 14 b).

- By the time they make a round trip, this takes about 85 ns (Fig. 16), the entrance electrode voltage is raised (Fig. 14 c). This time defines the maximum duration of the positron bunches.

- After passing many times through the electron plasma, positrons are trapped in their potential well by Coulomb-collisional damping (Fig. 14 d). Following [Miyamoto 1980], the collision time of a positron having velocity v with an electron plasma of density n and temperature T is given by:

$$\tau_{col}(v,n,T) = \frac{2\pi\epsilon_0^2 m^2 v^3}{ne^4 log(\lambda(v,n,T))} \tag{1}$$

m and e are the electron mass and charge, ϵ_0 is the permittivity of vacuum, and $log(\lambda(v,n,T))$ is the Coulomb logarithm $\simeq log(2\lambda_D/b)$, where $\lambda_D = \sqrt{\epsilon_0 kT/ne^2}$ is the Debye length and b is the minimal impact parameter taken to be $b = \frac{e^2}{4\pi\epsilon_0}\frac{2}{mv^2}$. The decrease in longitudinal velocity is then given by

$$\frac{dv_\parallel(t)}{dt} = -v_\parallel(t)/\tau_{col}(v(t),n,T) \tag{2}$$

By numerical integration of these equations, one gets the time needed to slow down positrons from their initial energy to the plasma temperature, which was measured to be about 0.01 eV in the RIKEN experimental conditions [Oshima 2004]. This cooling time is less than 1 ms for incident energies below 1 keV, as is shown in Fig. 17. Positrons lose enough energy in 3 ms to be trapped before the next burst from the electron Linac arrives, as long as the repetition rate is below 300 Hz. The time needed is actually longer than that shown in Fig. 17, because one must take into account the effective time spent by positrons within the electron plasma (roughly 30 % of the total time).

- The positive well depth is slowly increased during the accumulation process to accept more and more positrons: it is important to maintain a small voltage difference between the injection point and the positron plasma potential to ensure efficient cooling and to keep the round trip time of positrons in the trap small.

- When enough positrons have been stored, the potential level of the positron plasma reaches that of the electron plasma, and electrons flow out of the trap automatically. The electrode potentials are changed to form a unique well increased up to 1000 V for positrons, and the accumulation and cooling of positrons proceeds through the positron plasma already formed.

This scheme has never been realized. It will be tested at Saclay once the MRT and the slow positron beam line will be operational and connected (beginning of 2012).

6.2 The buncher

As described above, the positron bunches must be shorter than 85 ns so that the trap can be closed before the first positrons have made a round trip. With the present prototype Linac, the positron bunch duration is 4 µs (see section 4), and it seems unrealistic to obtain 85 ns pulses at the desired intensity directly from a small accelerator. It is thus necessary to compress the slow positron bunch. This will be realized by applying a varying voltage during the burst on the moderator. With the simulation parameters, the optimum function is (Fig. 18):

$$V(t) = 11 + 14\left(\frac{1}{(1 - \frac{t}{5.86})^2} - 1\right),\tag{3}$$

where t is in µs and V in volt.

The positrons are accelerated progressively with time in the burst to compensate for their late production. Assuming a flat emission intensity during the burst, taking an isotropic angular distribution and an energy spread of 0.7 eV for the emitted positrons, with a slow positron beam line of 13 m with a 8 mT driving magnetic field, simulations show that one can inject more than 40 % of positrons within 80 ns. This is a safe estimate since all the parameters used are pessimistic. This will be measured at Saclay with the demonstrator linac. The effective voltage variation will be optimized with the observed time distribution of the slow positrons. The value used in table 1 page 6 is 70 % because the assumed bunch length of the linac is 2 µs (Fig. 19).

6.3 Positron plasma characteristics

The accumulation scheme relies on the stability of the positron plasma during several minutes. Measurements performed with plasmas containing 1.2×10^{10} electrons at a temperature of 0.01 eV and a density of $10^{17}\,\mathrm{m}^{-3}$ show a lifetime of about 4000 s (Fig. 20). In addition, the rotating wall technique [Huang 1997] allows the compression of the plasma to a diameter d_p of order 300 µm [Oshima 2004] and improves its stability. This has been measured by ejecting the plasma onto a phosphor screen in a region of $B_o \simeq 50\,\mathrm{mT}$ magnetic field downstream of the MRT. The spot can be visualized with a CCD camera. Its observed diameter d_o can be extrapolated to the $B_c \simeq 5\,\mathrm{T}$ central region with the simple relation $d_p = d_o\sqrt{B_o/B_c}$.

6.4 Fast ejection electronics

Because the Ps lifetime is only 142 ns, the positrons must be ejected from the trap onto the e^+-Ps converter in less than about 100 ns to produce a dense Ps cloud. However, to fix ideas, a $1.3\ 10^{10}$ positron plasma has a length of about 15 cm within a parabolic 800 V deep potential well formed by the trap electrodes. At the ejection time, the electrode voltages have to be varied rapidly in a consistent way to produce a short bunch. This process has been tested at RIKEN. The voltage variation of the various electrodes is shown in Fig. 21.

The most dramatic change is 1700 V in 500 ns. One of the circuits used to test the fast ejection mechanism is shown in Fig. 22. After optimization, the measured pulses, Fig. 23, show that 10^9 electrons could be dumped in 20 ns FWHM, and 10^{10} in 76 ns FWHM.

6.5 High capacity trap

In order to take full advantage of the positron flux from the electron Linac and of the antiproton beam from ELENA, and to maximize the antihydrogen production rate, we consider building a higher capacity trap. The number of charged particles which can be confined is known to be proportional to the potential well depth, at least up to a few 10^{10} charges. As mentioned above, more than 10^{10} electrons could be stored for long times in the MRT with a 800 V potential well. The present electrode structure is capable of handling a 2 kV well depth. In order to reach a storage capacity of order 10^{11}, it is necessary to design a new structure with particular care concerning insulation to allow a 10 kV potential well. In addition, it has to be proven that a 10^{11} charges plasma can be compressed and stabilized long enough for the purpose of the experiment. This development has been proposed in [Pérez 2010], and will be pursued along with the demonstration of the new accumulation scheme of positrons from the Linac.
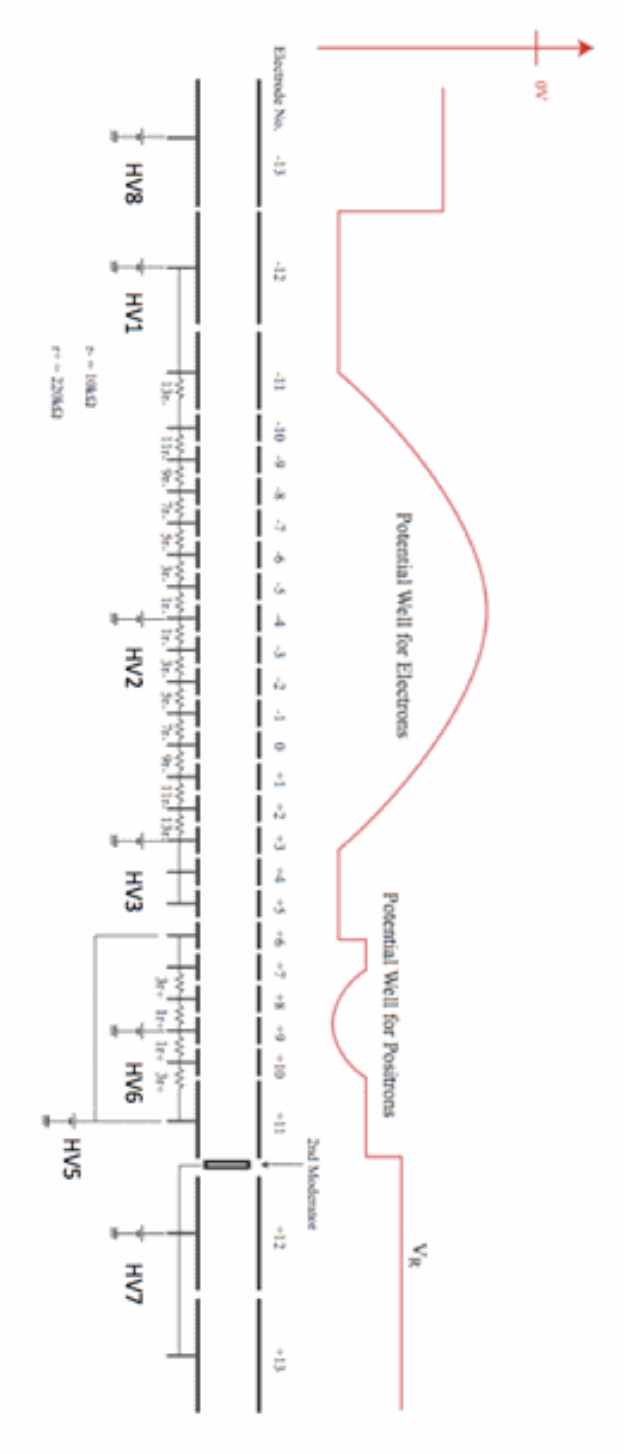
Figure 13: Potential wells formed in the RIKEN MRT for the accumulation of positrons in [Oshima 2004].

26
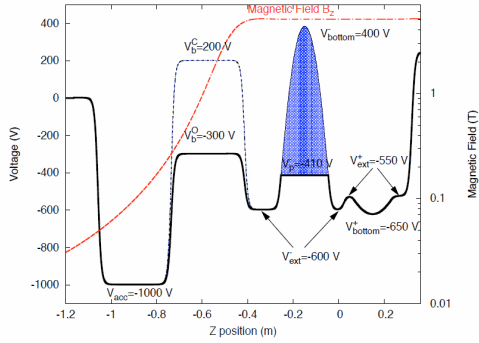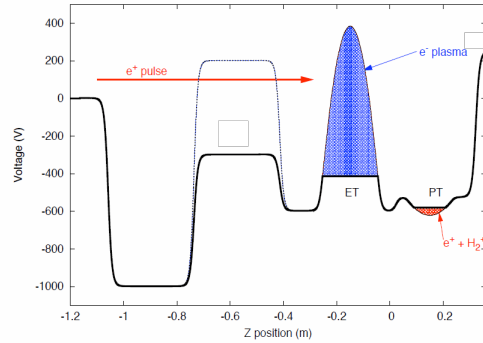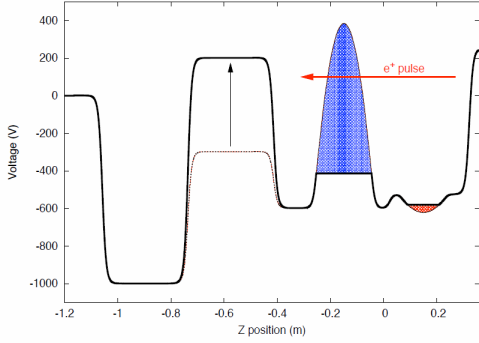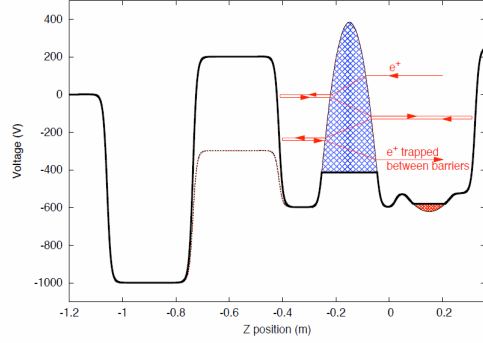
Figure 14: Illustration of the positron trapping scheme. a) Electromagnetic configuration of the trap. V_{acc} is the entrance electrode voltage, for the acceleration of positrons to let them pass the magnetic barrier. V_B^O and V_B^C are the trapping electrode voltages at the injection and trapping stages respectively. The solid line gives the potential on the trap axis at the positron injection stage. The blue dotted line corresponds to the trapping stage. V_{bottom}^- and V_{ext}^- are the potentials of the outer and central electrodes of the electron well. V_P is the electron plasma potential. The shaded area shows the modification of the potential due to the electron plasma. V_{ext}^+ and V_{bottom}^+ are the potentials of the outer and central electrodes of the positron well. The red dotted line gives the longitudinal magnetic field (right scale). b) Injection stage (ET: electron trapping well; PT positron trapping well). c) Trapping stage. d) Moderation process: positrons lose energy in the electron plasma.
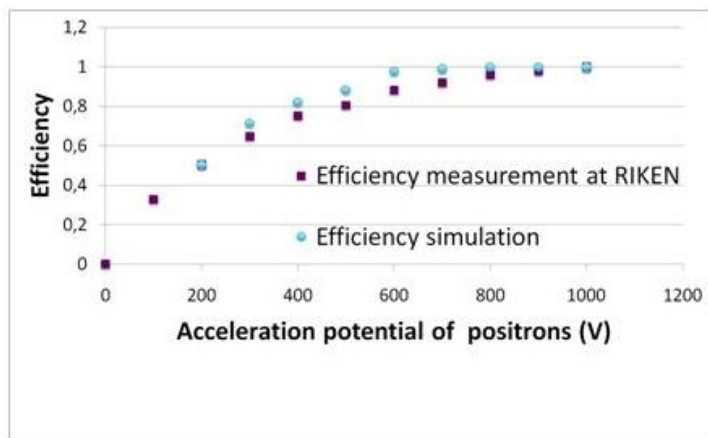
Figure 15: Measurement and simulation of the efficiency for positrons from a ^{22}Na source to pass the magnetic mirror of the RIKEN MRT as a function of the acceleration potential.
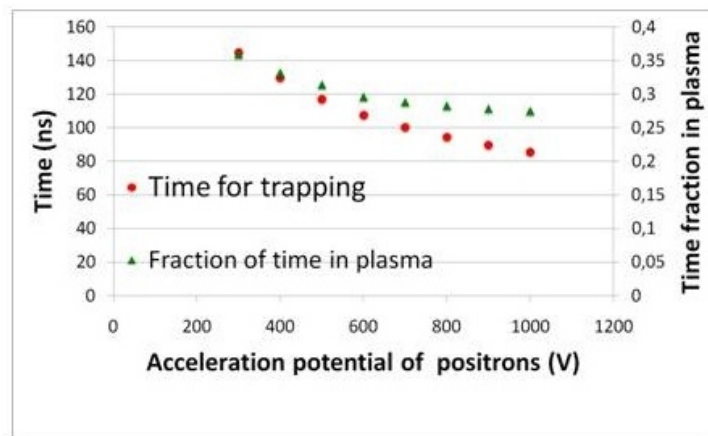
Figure 16: Time for trapping positrons in the MRT (this is the round trip time) and the fraction of time spent by positrons in the electron cloud as a function of the acceleration potential.
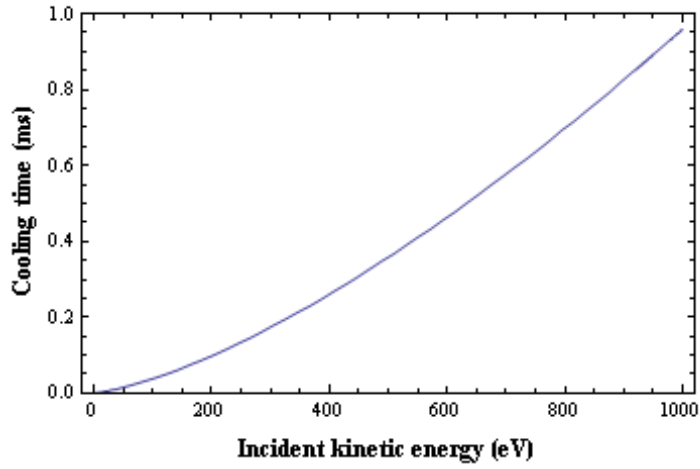
Figure 17: Cooling time of a positron in an electron plasma of density 10^{17} m^{-3} and temperature 0.01 eV, as a function of the positron incident energy.
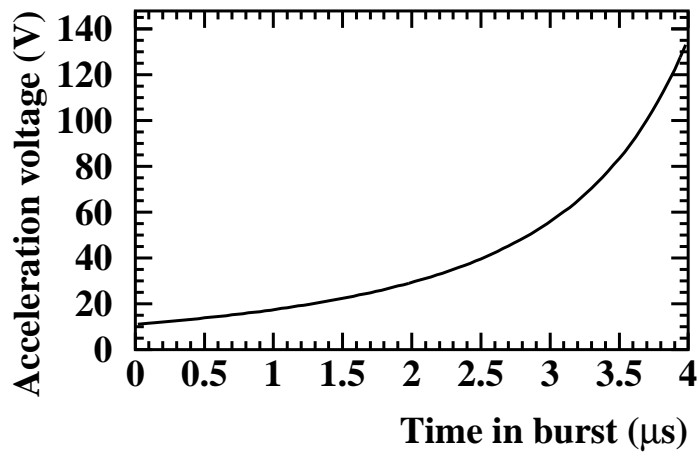
Figure 18: Voltage on the moderator as a function of time in the burst.
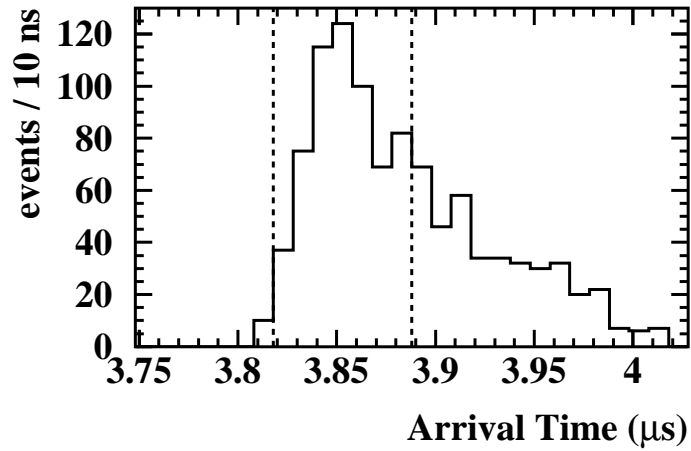
Figure 19: Time of flight distribution of positrons at the entrance of the MRT for a linac bunch length of 2 μs. About 70 % arrive in a 80 ns window around 3.86 μs.
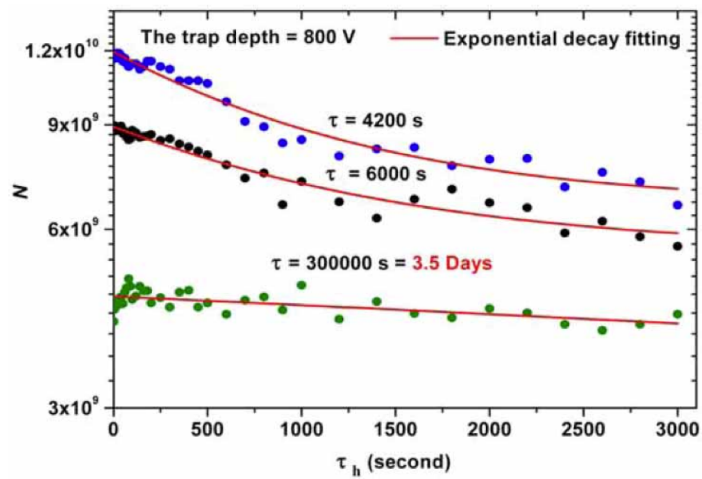
Figure 20: Plasma stability as a function of time and number of electrons [Mohamed 2008].
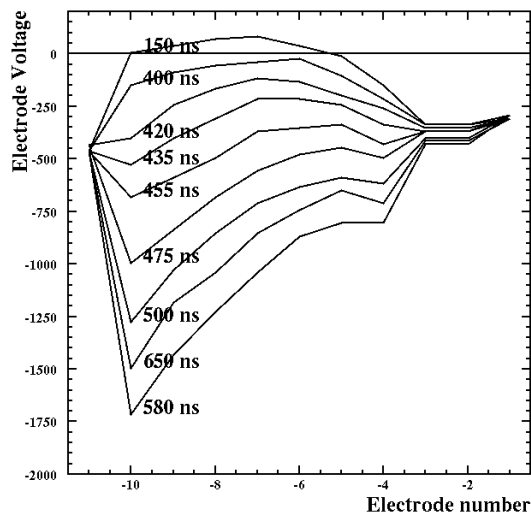
Figure 21: Applied electrode voltages as a function of time. Electrodes are numbered from -13 to +13 as shown in Fig. 13. For the reported results, only the half upstream electrodes voltages are varying. Downstream electrodes are at 0 potential.
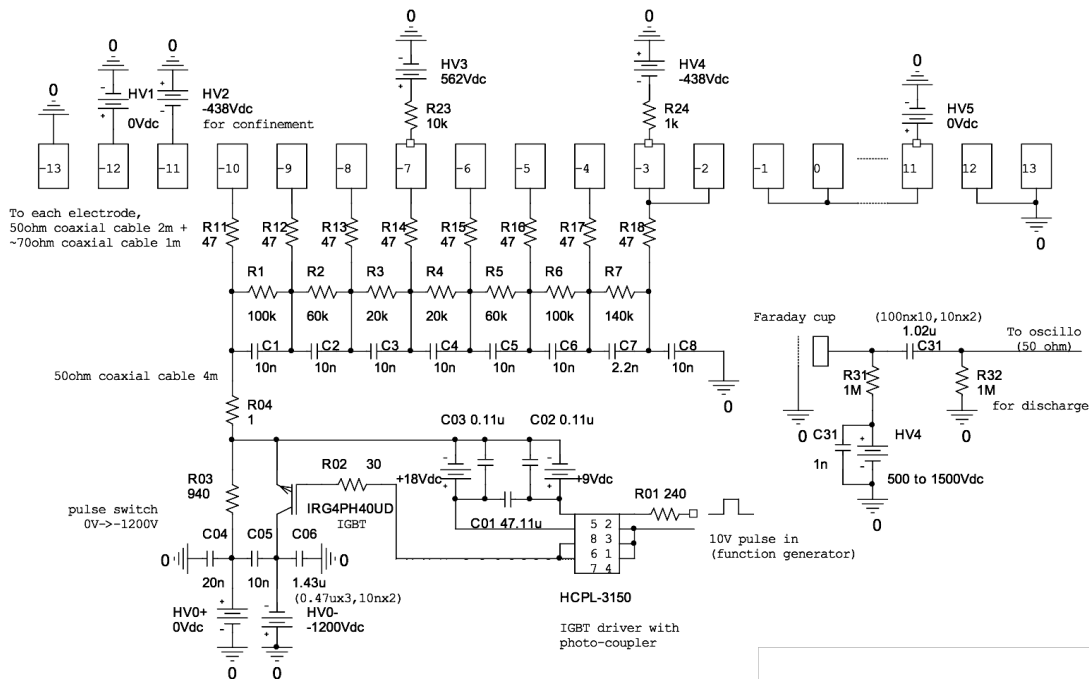
Figure 22: Example electronics circuit used for the fast ejection tests of the electron plasmas.
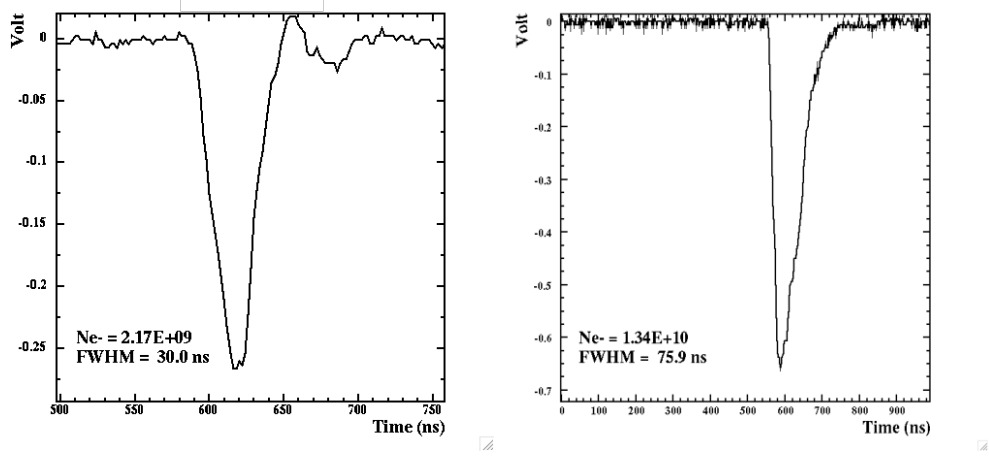
Figure 23: Fast ejection of electron plasmas : observed pulses on a Faraday cup.

7   Production of slow antiprotons

7.1   Requirements for the antiproton beam

In order to produce $\overline{\mathrm{H}}^+$ ions, the processes;

$$\overline{\mathrm{p}} + \mathrm{Ps} \rightarrow \overline{\mathrm{H}} + \mathrm{e}^- \tag{4}$$

$$\overline{\mathrm{H}} + \mathrm{Ps} \rightarrow \overline{\mathrm{H}}^+ + \mathrm{e}^- \tag{5}$$

are assumed. The $\overline{\mathrm{H}}$ production cross section peaks at $\sigma_{\overline{\mathrm{H}}} \sim 1 \times 10^{-15}\,\mathrm{cm}^2$ for incident $\overline{\mathrm{p}}$ with 0.5–15 keV kinetic energy [Humberston 1987, Merrison 1997]. Due to the limited life time of Ps (n=1), the $\overline{\mathrm{p}}$ beam is expected to be in a ≤ 100 ns bunch. Besides, the beam radius should be fit to the size of the Ps cloud. The requirements for the $\overline{\mathrm{p}}$ beam are summarized in Table 4. We discuss here the various possibilities to produce the necessary $\overline{\mathrm{p}}$ beam.

Energy	0.5–15 keV
Intensity	1×10^7
Pulse width	≤ 100 ns
Spot size in diameter	1 mm

Table 4: Requirements for the $\overline{\mathrm{p}}$ beam.

7.2   The AD cycle and the ELENA ring

Fig. 24 shows the AD cycle. At CERN, antiprotons are produced by collision of protons at 26 GeV/c with an Ir block via the reaction $\mathrm{p} + \mathrm{p} \rightarrow \mathrm{p} + \mathrm{p} + \mathrm{p} + \overline{\mathrm{p}}$. A fraction of them are collected at 3.6 GeV/c and stored in the AD ring. The AD cools them by stochastic cooling and with electrons and decelerates them to a momentum of 100 MeV/c or 5.3 MeV in kinetic energy. Then the $\overline{\mathrm{p}}$ are injected to experimental zones as a pulsed beam of typically 3×10^7 $\overline{\mathrm{p}}$ in a bunch length of 150 ns. The overall time duration of the AD cycle varies shot by shot depending on the super-cycle of the PS machine, but is typically 110 s.

The project to build an extension of the AD to decrease further the antiproton beam energy and increase the available slow antiproton beam intensity has been launched. This is the ELENA ring, the parameters of which are taken from [Eriksson 2010]. At every AD cycle, the beam contains 2.5×10^7 $\overline{\mathrm{p}}$, but it is divided into 4 bunches for multiple ejection to four independent experiments at the AD, which results in $\sim 6 \times 10^6$ $\overline{\mathrm{p}}$ for each experiment. We assume that the GBAR experiment would take data after the ELENA ring is built, and with those parameters.

7.3   Direct beam injection from ELENA to the positronium target

We propose in this section a scheme to decrease the ELENA beam energy from 100 keV to 1 keV with good efficiency and little increase in emittance without intermediate
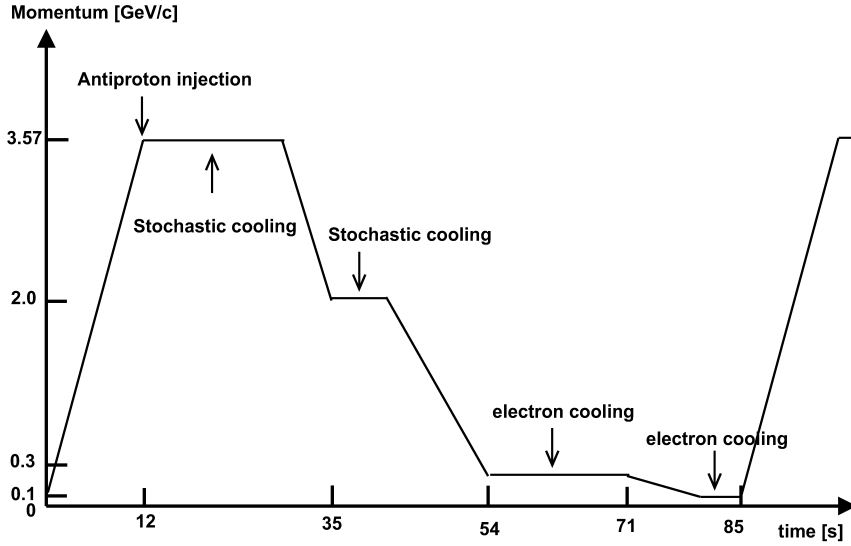
Figure 24: The AD cycle.

trapping of antiprotons. The method, based on experience from cooling and trapping beams of radioactive nuclides, relies on the electrostatic deceleration of the antiproton bunches into a drift tube at 100 kV which is then electrically switched down to 1 kV before the antiprotons exit the tube.

Particle beams are usually transported at ground potential. A beam with kinetic energy E can therefore be stopped by a retarding optical element that is raised to the corresponding potential $V = E/e$. After decreasing the 100 keV ELENA beam to e.g. 1 keV (by setting V to 99 kV), the beam pulse enters a drift tube inside of which the ions feel no voltage gradient. At this moment the voltage of the drift tube can be quickly (in about 200 ns) switched from 100 kV to 1 kV. It is only when exiting the tube that they will feel a gradient, between the drift tube at 1 kV and the following grounded electrode. The scheme is illustrated in Fig. 25.

From the ELENA Design Document [Eriksson 2010], the specified antiproton emittance is 4π mm·mrad at 100 keV. When this beam is slowed down to 1 keV, the emittance will blow up to 40π mm·mrad. Focusing this beam through a 10 mm hole will result in a divergence of 8 mrad and a transverse energy of 8 eV. This moderate divergence can be focused by an einzel lens arrangement (replacing the segmented electrode structure in Fig. 25) into the pulse-down drift tube that follows.

The above discussion considers only the transverse emittance. The longitudinal emittance will also be affected by the deceleration. Again, from the ELENA Design document [Eriksson 2010], the 100 keV bunches will have a duration of 300 ns. This corresponds to a bunch length of 1.3 m. In order to accommodate the increased length after deceleration, it will probably be necessary to use a ramp voltage on the deceleration electrode to modulate the energy spread and achieve a time focus inside the pulsed-down cavity. Again, detailed simulations will allow us to refine the design. This energy spread will be somewhat reduced after the 1 keV re-acceleration. The bunch duration has to be

34
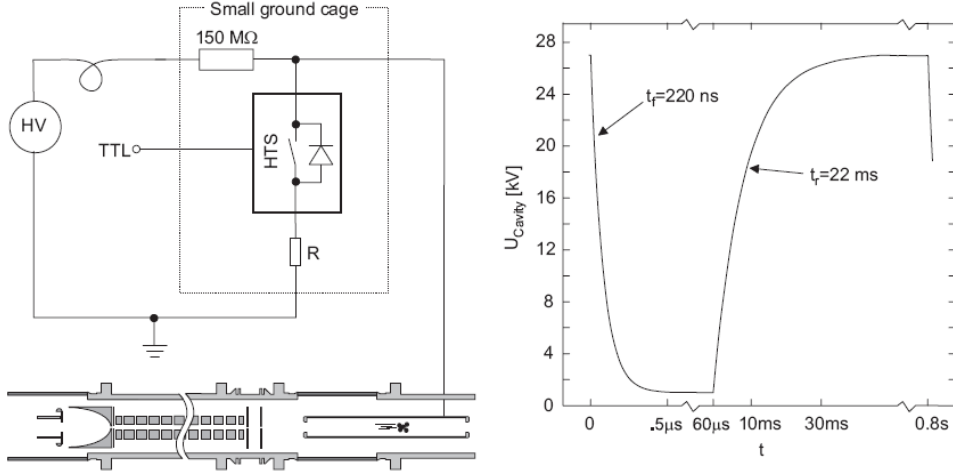
Figure 25: Illustration of a deceleration structure and pulsed drift tube setup for transforming the fast (30 keV) heavy-ion ISOLDE beam into low-energy (2 keV) bunches. The beam enters an RFQ structure (from the left) mounted at a voltage of 30 kV. After confinement by segmented RF electrodes (not required for antiprotons) the pulse enters a drift tube that is connected to high-voltage switching circuit (upper left). While the particles are inside the drift tube (before 60 µs), the pulse-down voltage (right) is applied. Since the particles feel no gradient inside the drift tube, they are only moderately accelerated when they exit. Image is from [Herfurth 2001].

reduced to less than 150 ns to match the Ps target lifetime.

Considerable experience with on-line deceleration systems has shown that heavy-ion beams can be decelerated and cooled in such devices with very good efficiencies (up to 80 % - see [Lunney 2009, Herfurth 2001]). The advantage in the present proposal is the absence of buffer gas (prohibited by risk of annihilation) that considerably eases requirements for confinement and differential pumping. (Note: in Fig. 25, heavy ions with positive charge were used. The new system would of course be designed with negative voltages for antiprotons.)

This scheme is taken as the baseline for the GBAR experiment, at least in a first stage. An 80 % efficiency is assumed in table 1, page 6.

The next sections present a scheme where antiprotons are trapped and cooled before being sent onto the positronium target. This would allow the parallel storage of more positrons in the RIKEN MRT and significantly increase the $\overline{H}^+$ production rate. The trapping of antiprotons would be absolutely necessary without ELENA. For this reason, we describe first a trapping scheme without ELENA as a back up solution, and then with ELENA, as an upgrade possibility.

7.3.1 Accumulation of slow antiprotons from the AD

The energy of the AD beam is very far above the 1-10 keV range needed. Degrader foils, 70 mgcm^{-2}, have been used to reduce the $\bar{p}$ energy from the MeV scale to the keV scale [Gabrielse 1986]. Over 99% of the incident $\bar{p}$ either stop and annihilate within such foils or are too energetic to be trapped, such that the remainder is too low to perform the GBAR experiment. Penning-Malmberg traps, *i.e.* ion traps with static electro-magnetic fields, are commonly used to capture and accumulate energy degraded $\bar{p}$ beams [Gabrielse 1986, Amoretti 2004, Kuroda 2005]. The $\bar{p}$ emerging from the foils are captured in the potential well of a trap. Since the typical trapping efficiency is only 0.1% of the incident $\bar{p}$ number, the so-called stacking technique would be necessary to prepare $\sim 10^7$ $\bar{p}$ in a trap for the GBAR experiment. The antiprotons could be stored in the trap and cooled with a preloaded e$^-$ plasma. Two groups at the AD, the ATRAP and ASACUSA collaborations, demonstrated this technique to obtain 10^7 $\bar{p}$ [Kuroda 2010, Gabrielse 2011].

A possible design of a GBAR trap installed downstream of the AD is inspired by the MRT [Mohri 1998] as shown in Fig. 26. The GBAR trap would consist of a stack of ring electrodes, a superconducting solenoid, and the above mentioned energy degrader in order to confine a large number of $\bar{p}$. It would consist of two parts, which are the catching trap and a manipulation trap. Several incident $\bar{p}$ bunches from the AD are accumulated and cooled in the catching trap (see details in section 7.5). Then they are transferred to the manipulation trap, where the size of the $\bar{p}$ cloud is adjusted to the target Ps cloud. Antiprotons are extracted as a short bunch beam. During this manipulation, other $\bar{p}$ bunches from the AD are simultaneously accumulated in the catching trap, to make an efficient use of the AD output.
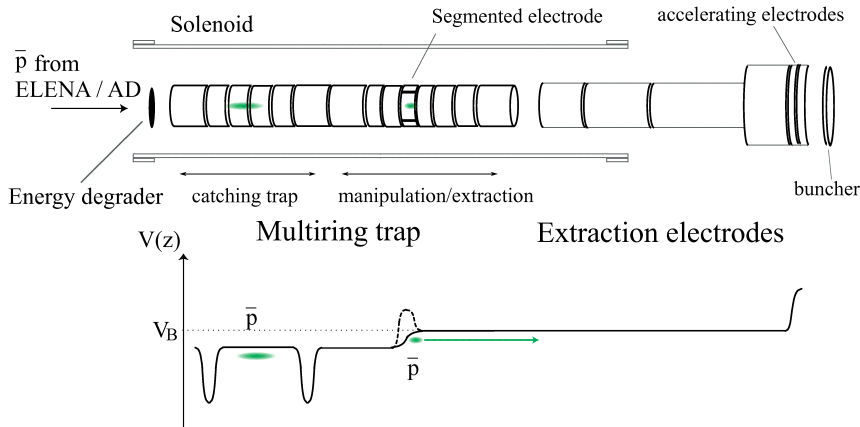
Figure 26: Schematic illustration of a $\bar{p}$ trap for GBAR.

In order to control the size of the $\bar{p}$ cloud in the GBAR trap, the rotating wall technique is applicable [Huang 1997]. For this purpose, one of the ring electrodes in the manipulation trap is segmented into 4 sectors to apply a radio frequency field with phases shifted by $\pi/2$ from one segment to another. A rotating electric potential wall is thereby generated, that

can exchange angular momentum with the plasma, which is thus radially compressed. At the AD experiments [Andresen 2008, Kuroda 2008], $\overline{p}$ clouds in traps are successfully radially compressed with and without e^-. A diameter of about 0.5 mm could be obtained in the ASACUSA MUSASHI trap, a value adequate for the GBAR experiment.

7.3.2 Antiproton trap with ELENA

When ELENA is built, intense $\overline{p}$ beams become available. The above-mentioned GBAR trap remains an effective way to obtain 10^7 $\overline{p}$ at 1 keV energy with ELENA. According to the foreseen parameters of ELENA, as mentioned above, the beam contains 2.5×10^7 $\overline{p}$ shared by 4 experiments, which results in $\sim 6 \times 10^6$ $\overline{p}$ for each experiment. The GBAR trap has a capability to accumulate several $\overline{p}$ pulses from ELENA as discussed above, which enables the provision of a more intense $\overline{p}$ bunch to irradiate the Ps cloud. As in the case of the AD, the GBAR trap would also use the ELENA beam efficiently and accumulate antiprotons readily.

According to the ASACUSA collaboration, the deceleration efficiency with 70 mgcm^{-2} foils for the 5.3 MeV beam of the AD is only 0.1 %. The ejection energy of ELENA is designed to be 100 keV as mentioned above, so that a relatively thin, $\sim 180 \,\mu\mathrm{gcm}^{-2}$, degrader foil is needed [Kuroda 2005], and the efficiency becomes as high as ~ 60 %.

7.3.3 Fast ejection of antiprotons

In order to make a short bunched $\overline{p}$ beam from the trap, a fast extraction scheme needs to be developed. The ASACUSA collaboration succeeded in making a 2 µs long 150 eV $\overline{p}$ beam to transport them to their CUSP trap for synthesizing $\overline{\mathrm{H}}$ atoms [ASACUSA 2010]. This is still too long for the GBAR experiment. To shorten this pulse duration, it will be necessary to develop the technique to obtain a plasma length smaller than 1 cm and an effective way to extract it.

7.4 GBAR trap operation

The procedure to produce a slow $\overline{p}$ beam with the GBAR trap is as follows:

1. The e^- are injected into the GBAR trap and form a non neutral-plasma.

2. From the AD / ELENA, a slow $\overline{p}$ beam is injected into the GBAR trap via a degrader foil.

3. The $\overline{p}$ are captured in the catching trap region and cooled via collisions with the preloaded e^- plasma.

4. Accumulate a number of $\overline{p}$ shots in the catching trap.

5. Once the $\overline{p}$ are cooled, they are transferred to the manipulation trap.

6. A rotating wall field is applied to the $\overline{p}$ cloud to adjust its size.
   At the same time, $\overline{p}$ capture and accumulation are proceeding.

7. A compressed $\overline{p}$ cloud is ejected as a short bunch beam.

As mentioned above, the GBAR trap simultaneously accumulates the $\bar{p}$ bunches during manipulation and ejection. The stacking of AD shots takes ~ 1 hour in order to obtain 10^7 $\bar{p}$ in the case of ATRAP without ELENA, and about 12 minutes in the case of ASACUSA.

The ELENA cycle is foreseen to fit to that of the AD, so the cycle time of the 5.3 MeV/100 keV $\bar{p}$ beam is also 110 s. If the trapping efficiency of the GBAR trap is assumed to be 50 %, 3×10^6 $\bar{p}$ are expected to be trapped, so that, the GBAR trap with ELENA takes 4 AD cycles to obtain 10^7 $\bar{p}$, that is, only $\sim$ 8 minutes. Although the compression with the rotating wall technique takes 100-200 s [Andresen 2008, Kuroda 2008], the beam will be provided every cycle, since the GBAR trap has a capability of accumulating $\bar{p}$ shots simultaneously.
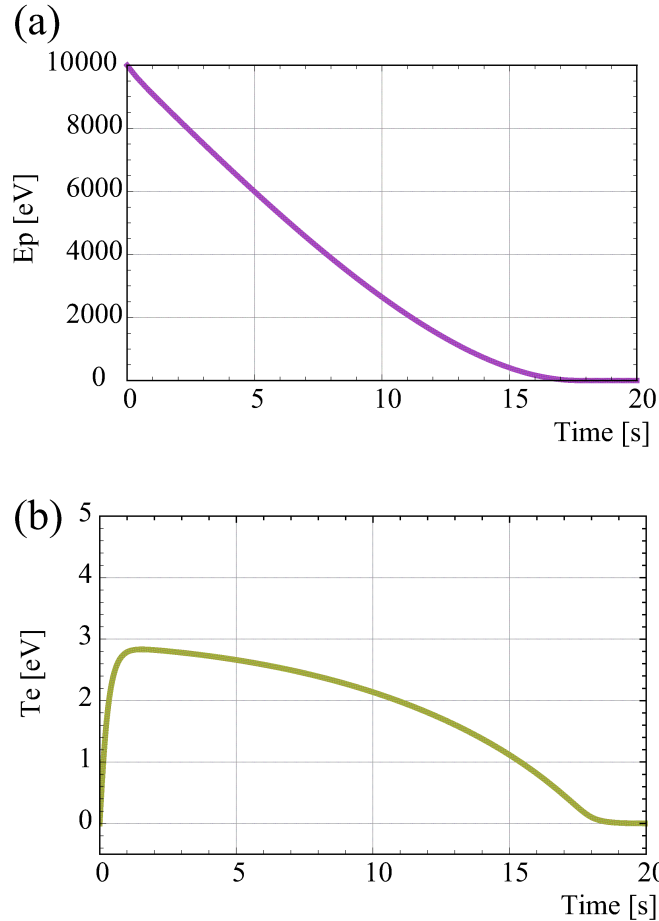
Figure 27: (a) Energy variation of the antiproton beam calculated with a beam deceleration model. (b) Temperature variation of the electron plasma calculated with the beam deceleration model.

7.5 Deceleration of the antiprotons with an electron plasma in a multi-ring electrode trap

The number of $\bar{p}$ is expected to be of the order of 10^7, so that the number density of e^- needed would be $\sim 10^8 \text{cm}^{-3}$ for efficient cooling. The energy exchange rate between an incident $\bar{p}$ beam and an e^- plasma $S(T_e, E_p)$, where T_e is the temperature of the electron plasma and E_p is the energy of the antiproton, can be calculated by following [Sivukhin 1966]. The time evolution of $E_p(t)$ and $T_e(t)$ can be obtained. The result is shown in Fig. 27, under the conditions: $N_{\bar{p}} = 10^7$, $N_{e^-} = 8 \times 10^8$, $n_e = 7.3 \times 10^7 \text{ cm}^3$, $B = 3$ T.

An incident 10 keV $\bar{p}$ beam is cooled within 20 s. The temperature of e^- increases but returns to the original value within 20 s. Once the beam energy is decreased to $E_p \leq e\phi_s$ where ϕ_s is the effective trap potential and e the electron charge, the $\bar{p}$ fall into the trapping well.

8 Production of ortho-positronium

The positron/positronium converter and its environment is one of the key parts of the experiment. Its function is to form a dense positronium cloud from the intense positron pulse arriving from the high field particle trap. Access for the antiproton beam and two counterpropagating laser beams as well as free exit for the created $\overline{H}$ and $\overline{H}^+$ have to be provided. Furthermore, a set of beam diagnostic devices will be installed around the interaction chamber to characterize the incoming beams and the positronium cloud.

8.1 Principle of positron-positronium converter

Positronium (Ps) is the bound state of a positron and an electron. In its ground state, the triplet form (*ortho*-positronium, o-Ps) decays with 142 ns lifetime in vacuum, while the lifetime of the singlet form (*para*-positronium, p-Ps) is as short as 125 ps. Ps is formed in many materials from low energy positrons (at electronvolt or thermal energy) and an electron of the lattice. As the lifetime of *para*-positronium is far shorter than the length of the antiproton pulses that is attainable in the experiment, only *ortho*-positronium will be taken into account in the following discussion.

A dense *ortho*-positronium cloud will serve as a target for antiprotons. Its density has to be sufficiently high to allow the two reaction steps (4) and (5) (page 33) that lead to the formation of the positively charged antihydrogen ion to occur in the cloud with sufficiently high probability. A solid-state converter will be used to form the Ps cloud from a short positron pulse. Positrons will be implanted into the converter material at an energy of a few keV and positronium will be subsequently emitted from the same surface into vacuum. For brevity, we will refer to this component as "positron/positronium converter" in the text. The requirements for the converter material are the following:

- high positron/vacuum *ortho*-positronium conversion efficiency (vacuum *ortho*-positronium yield);

- low positronium kinetic energy (to ensure high effective positron density near the surface);

- good stability under the vacuum condition of the beam line;

- good stability of the conversion efficiency under irradiation and laser illumination;

- if possible, no need for *in situ* treatment (high temperature annealing, cleaving).

Positronium emission upon positron implantation has been found on metal, insulator and semiconductor surfaces. The energy of the emitted Ps depends on the material and underlying physical process. In the case of materials where the work function of positronium is negative, the energy of the directly emitted Ps (may be called "work function positronium") is relatively high, up to a few electronvolts. If positronium is formed from a positron bound in a surface state on the material and is then emitted by thermal detachment, the energy distribution depends on the sample temperature and the Ps binding energy. However, in most cases, significant Ps emission can be observed only at high temperature and the mean kinetic energy of the Ps is more than 0.1 electronvolt. Frequently, emission by both mechanisms can be observed in the same

surface. Positronium emission from metal or semiconductor surfaces is a possible effect that can be exploited in the positron -positronium converter of the GBAR experiment. However, the effect is very sensitive to the condition of the suface, requires very good vacuum and may require regeneration of the surface after a relatively short time.

On the basis of the literature and our previous experiments, we retained another group of materials, porous silica, as the most promising candidate for the function of positron/positronium converter [Liszkay 2010]. Evidence of efficient *ortho*-positronium emission was found in thin nanoporous silica films [Gidley 1999], and the effect has been investigated by several groups. The films are pure SiO_2 structures, containing a network of pores of nanometer size with a different degree of interconnection. A number of such structures have been developed lately, with various, well controlled pore size, porous fraction and symmetry.
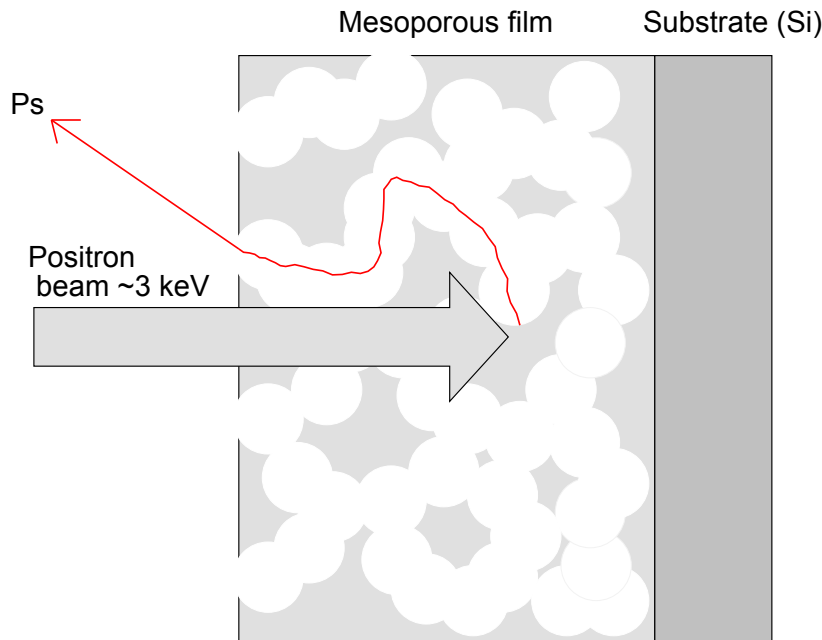
Figure 28: Schema of the positronium emission process from a mesoporous film.

Positrons are implanted in the porous film with a depth distribution that can be described by a Makhovian implantation profile [Schultz 1988]. The mean implantation depth is $\bar{z} = AE^{1.6}$, where E is the kinetic energy in keV, $A \approx 400/\rho$ Å/keV$^{1.6}$, and ρ is the target density in gcm^{-3}. In a highly porous film with approximately 1.2 gcm^{-3} density the mean implantation depth at 3 keV positron beam energy is 193 nm. The microscopic details of positronium creation in the porous film are not entirely known, though the kinetic energy of Ps at its birth in the pores is thought to be more than 1 eV [Nagashima 1998]. In interconnected (open) pores the positronium diffuses in the pores and eventually may reach the surface of the film and escape into vacuum. The energy of the diffusing Ps decreases through scattering processes [Nagashima 1995, Mariazzi 2008], as evidenced by the decrease in the kinetic energy of the escaping Ps with increasing positron implantation energy, i.e. with increasing mean implantation depth. On the basis of positronium time-of-flight measurements the energy of Ps escaping from the pore

system was estimated to be 50 meV or less [Yu 2003].

8.2   Tests of positron-positronium converters

Although a number of papers have been published earlier on positronium escape from nanoporous silica films, the methods used were not sufficiently complete to ensure full characterization of the emitted Ps for the purpose of the converter. There are many possible effects that can hinder positronium from being emitted into vacuum. It can be quenched by the interaction with the SiO_2 surface, by paramagnetic defects on the internal surfaces [Saito 1999] or by chemical effects of contaminating species. It can be trapped in isolated pores of different size, which appear as imperfection of the pore system. In most cases, the positronium yield was experimentally determined from the energy distribution of the annihilation γ radiation, using the 3 γ annihilation fraction. Although this reaction is a reliable fingerprint of the self-annihilation of o-Ps in vacuum, it cannot make distinction between Ps annihilation in vacuum and Ps annihilation with a very long (nearly vacuum) lifetime. Only lifetime measurements can determine the actual intensity of the 142 ns vacuum o-Ps component. In addition, the problem with the existing lifetime studies is that the detection efficiency of the annihilation of the emitted o-Ps is smaller than that of the positron annihilation in the sample. Consequently, the detected lifetime spectrum is distorted and the determination of the vacuum o-Ps fraction is not correct.

To ensure reliable characterization of the films, we set up a system to study both the conversion efficiency and the energy of the emitted o-Ps [Liszkay 2008]. A large (220×210 mm^2, 55 mm thick) BGO detector was used as lifetime detector, which provides a detection efficiency which is largely independent of the place of the annihilation. A TOF detector used BGO crystals with a 5 mm wide lead collimator to determine the kinetic energy of the escaping o-Ps. The start signal for both detectors was supplied by a fast MCP (multichannel plate) electron multiplier, detecting secondary electrons ejected by the impinging positrons.

Based on the experimental results using the combined lifetime-TOF spectrometer, we retained two types of mesoporous silica films as possible candidates for positron-positronium converter materials. Both were grown using a sol-gel method and deposited by spin coating on a glass or silica surface:

- "C film", mesoporous film grown using CTACl (cetyl trimethyl ammonium chloride) as porogen, with 3-4 nm pore size and a CTACl/Si molar ratio of 0.22;

- "F film", mesoporous film grown using Pluronix F-127 as porogen, with 5-8 nm pore size and an F-127/Si molar ratio of 0.016.

The thickness of the films is 300-1000 nm. The positronium yield (fraction of positrons that escape from the film as o-Ps) is somewhat higher in the case of the C film, while the F film is thicker and shows a more stable yield as a function of the incident e$^+$ energy (Fig. 29). In both cases, a beam energy of approximately 3 keV is necessary to ensure that the kinetic energy of emitted Ps falls below 0.1 eV (Fig. 30). The kinetic energy is lower in the case of the F film. The difference is attributed to the higher confinement energy in the smaller pores of the C film [Crivelli 2010].
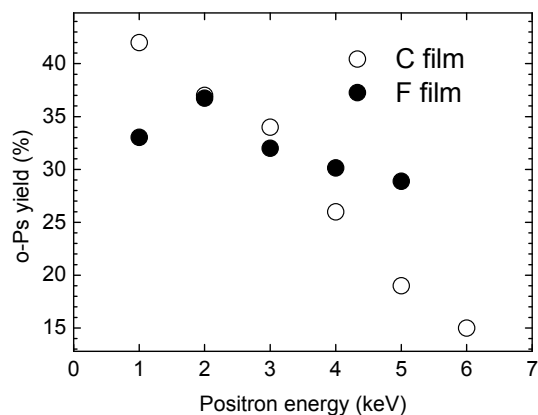
Figure 29: Vacuum ortho-positronium yield as a function of the positron beam energy in two mesoporous films.
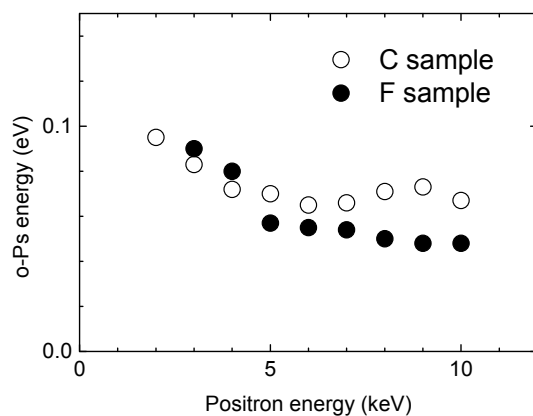
Figure 30: Mean energy of the emitted o-Ps as a function of the positron beam energy in two mesoporous films.

Subsequently, a sample from both film types was characterized by David Cassidy (Univ. of California Riverside, USA) at the high intensity pulsed beam combined with a Ps Lyman α laser [Cassidy 2010]. He found that the o-Ps escape from the C film was strongly suppressed by laser irradiation. The F film reemitted o-Ps with approximately the same yield as in our measurements. The different sensitivity to laser illumination in the test may be related to the fact that the C sample was grown using a cationic detergent, while the F-127 porogen is a non-ionic substance. The loss of positron/positronium conversion efficiency may be related to excitation of defects on the inner pore surface. The films are

43

being investigated by optical methods, in order to identify the origin of the Ps quenching effect. The insensitivity of the F film to laser illumination makes it a better candidate for the purpose of the positron/positronium converter. Further investigations are under way to test new types of films with different pore size, grown with non-ionic porogen, in a search for higher efficiency.

In the final configuration, a pulse containing a few times 10^{10} positrons will be incident on a surface of order of 10 mm^2, giving a few times 10^{11} e$^+$ cm^{-2} positron beam areal density. This is about one order of magnitude higher than the areal density used by Cassidy and Mills in their experiment which demonstrated Ps-Ps interaction and the formation of the Ps$_2$ molecule in similar films [Cassidy 2008]. The Ps-Ps interaction appears as loss of efficiency in the converter film. Further loss can be caused by defect creation by the positron irradiation itself. In the case of a very significant quenching effect due to either Ps-Ps interaction or by defects created or excited by positrons in the internal surfaces, the areal density must be reduced to the level where the effect is tolerable. We are developing a setup that can test the quenching effect of defects created by electron irradiation. In contrast, the effect of Ps-Ps interaction can only be tested at the final configuration, where the entire positron bunch amplitude is available.

8.3   Setup of the positron/positronium converter

Positrons will be ejected from the high field trap in a short (approximately 100 ns) pulse, with the help of a buncher. The beam will be extracted from the magnetic field according to the scheme (Fig. 31) described in [Weber 2010] and [Weber 2011]. In the GBAR setup an improved magnetic shield structure, a "magnetic spider" will be used, similar to the one developed for a positron microbeam in the Broohaven National Laboratory [Gerola 1995] and at LLNL [Stoeffl 1999]. A significant improvement is expected in the quality of the extracted beam and, consequently, in the size of beam spot. In the magnetic field-free region the beam transport will be achieved using electrostatic (Einzel) lenses and an electrostatic mirror. The construction of the electrostatic beamline follows the design of the existing slow positron beam at Michigan State University [Gidley 2001]. In the case of the GBAR positron beamline, the electrostatic mirror is necessary to provide access for the two laser beams, the antiproton beam and the downstream antihydrogen transport line.

The converter structure is a small tube with typically 1 mm inner diameter and 20 mm length, with a mesoporous film on the inner surface (Fig. 32). The actual dimensions will be determined according to the diameter of the antiproton and the positron beam. The cross section of the tube is a square, formed by plates cut from a silicon single crystal wafer. The mesoporous film is deposited on the silicon wafer prior to cutting it to the final shape.

Positrons and antiprotons enter the tube from the opposite direction (Fig. 32). The construction makes use of the large difference between the transport properties of protons and electrons in a low magnetic field. A small coil will be placed in the vacuum chamber, around the converter tube, at the midpoint of the tube and tilted by approximately 10° from the beam axis. The magnetic field deviates the positrons from the axis, but does not significantly change the trajectory of the antiprotons. The deviation of the positron beam is such that the positrons reach the inner surface of the converter tube and form positronium via the mechanism detailed in section 8.1.
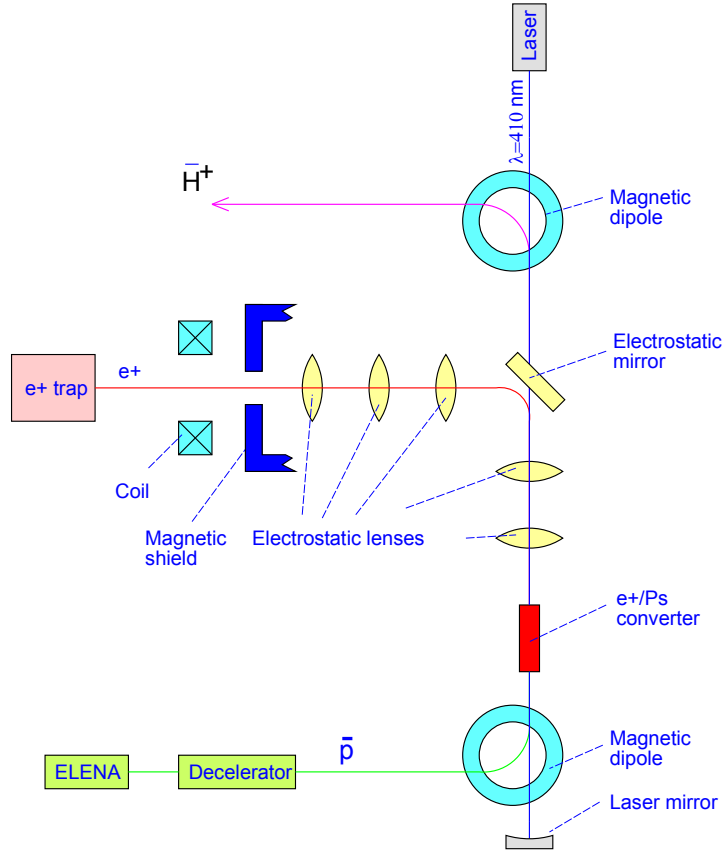
Figure 31: Schematic of the positron beamline after the high field trap and the environment of the positron/positronium converter. The antiproton beam and the created antihydrogen ions are bent by a dipole to leave access for a laser beam. A laser with a mirror provides two counter-propagating beams for the two-photon excitation of the positronium 1S-3D transition. Positrons, ejected from the high field trap in a short pulse, are extracted from the magnetic field and transported by an electrostatic optical system to the positron-positronium converter tube. An electrostatic plane mirror diverts the positrons into the axis of the antiproton beam. After the arrival of the positron pulse, the field of the mirror is removed to let the antihydrogen ions through towards the deflection magnet.

Positronium is reemitted in a broad angular distribution from the porous film. Positronium at 0.1 eV energy flies several cm before annihilation. o-Ps which reaches the surface at the opposite side of the tube is scattered back into the inner volume of the tube, thereby remaining in the interaction volume with the antiprotons. In the interaction with the silicon tube, the probability of quenching is expected to be very low. o-Ps has been observed to survive more than 10^5-10^6 collisions with silica walls in the porous samples, which points to a very low quenching probability in a single collision.
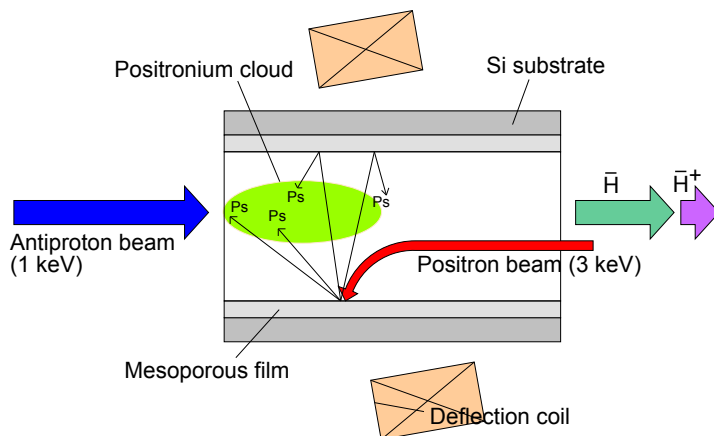
Figure 32: Schematic of the positron/positronium converter structure.

We plan measurements to confirm the very low positronium loss in the scattering process. Consequently, most of the created o-Ps remains in the target tube, forming the o-Ps target cloud. The density of the cloud is of order of 10^{12} Ps cm^{-3}, well below the density where significant Ps-Ps interaction would take place. In table 1, page 6, a loss factor of 0.5 is taken to account for the decay of o-Ps during the interaction time (~ 100 ns) of the o-Ps and the antiprotons.

The created antihydrogen ions will fly on a trajectory that is very nearly the continuation of the trajectory of the antiproton beam. The neutral antihydrogen atoms, 10^3 to 10^4 more numerous than the ions, will be also ejected in a focussed beam. The intense pulsed antihydrogen beam can be exploited for various experiments.

The antihydrogen ions will be ejected in the direction of the electrostatic mirror of the slow positron beamline. Before their arrival, the electric field of the mirror will be switched off to allow the ions to pass. At a few keV energy, $\overline{H}^+$ is relatively slow and there is sufficient time (about 100 ns) to switch off the electric field. The ions will pass through a small hole in the electrodes.

The installation should provide access for two counter-propagating laser beams at the ends of the converter tube, to allow laser excitation of positronium (see section 10). A small dipole will be installed along the antiproton beam line and at the antihydrogen exit point, in order to free up the line of sight of the positronium cloud before and after the converter tube, respectively.

8.4 Further research and development

The presently demonstrated ortho-positronium yield of more than 30 % at an energy below 0.1 eV leaves room for further improvement. Positron-positronium conversion with 100 % efficiency would produce 75 % o-Ps. This theoretical limit is hardly attainable due to the direct annihilation of positrons in the lattice and positronium quenching. A yield of 40-50 % may be possible with improved porous films. The mean energy of the emitted o-Ps appears to be limited by quantum localization of o-Ps in the

pores [Crivelli 2010, Cassidy 2010] and the inefficient energy dissipation [Mariazzi 2008]. Nevertheless, according to experimental results, an energy level below 0.05 eV may be possible while maintaining the yield. We plan to perform further experiments to test new types of porous structures in a search for higher conversion efficiency and lower o-Ps mean kinetic energy.

The highest positron-positronium conversion yield was reported on germanium single crystal surface at high temperature (900 °C) [Soininen 1991]. The authors concluded that up to 96 % of the positrons, implanted into the crystal at low energy, were emitted as positronium. This value corresponds to 72 % positron/ortho-positronium conversion efficiency, although, presumably, at a relatively high mean energy. We plan to test if a germanium surface is compatible with the experimental conditions and if this material is competitive with the porous films as a converter.

A new result shows that very short, intense pulses of positronium can be created using photoemission of Ps from a clean silicon surface [Cassidy 2011]. This method gives potentially better control over the Ps cloud formation. We will consider the use of this effect for the purpose of the positron/positronium conversion.

9 Production of the antihydrogen positive ions $\overline{\mathrm{H}}^+$

9.1 $\overline{\mathrm{H}}$ production cross section estimates

As described earlier in this document, the two processes which determine the rate of antihydrogen ion production are the formation of ground state antihydrogen in $\overline{\mathrm{p}}$-Ps collisions, and its subsequent interaction with a further Ps atom to produce $\overline{\mathrm{H}}^+$,

$$\overline{\mathrm{p}} + \mathrm{Ps} \rightarrow \overline{\mathrm{H}} + \mathrm{e}^- \tag{6}$$

and

$$\overline{\mathrm{H}} + \mathrm{Ps} \rightarrow \overline{\mathrm{H}}^+ + \mathrm{e}^- \tag{7}$$

It was shown many years ago [Humberston 1987], that cross sections for reaction (6), denoted as σ_{H}, are related by detailed balance and charge conjugation to those for Ps formation, σ_{Ps}, in $e^+ - \mathrm{H}$ collisions ($e^+ + \mathrm{H} \rightarrow \mathrm{Ps} + \mathrm{p}$). For hydrogen in a state with principal and orbital angular momentum quantum numbers n_{H} and l_{H}, respectively, and with counterparts for the Ps as n_{Ps} and l_{Ps} the cross section relationship is given by

$$\sigma_{\mathrm{H}}(n_{\mathrm{H}}, l_{\mathrm{H}}; n_{\mathrm{Ps}}, l_{\mathrm{Ps}}) = k^2 \sigma_{\mathrm{Ps}}(n_{\mathrm{H}}, l_{\mathrm{H}}; n_{\mathrm{Ps}}, l_{\mathrm{Ps}}) \frac{(2l_{\mathrm{H}} + 1)}{\kappa^2(2l_{\mathrm{Ps}} + 1)} \tag{8}$$

Here k and κ are the positron and Ps wavenumbers. As such, equation (8) can be rewritten as,

$$\sigma_{\mathrm{H}}(n_{\mathrm{H}}, l_{\mathrm{H}}; n_{\mathrm{Ps}}, l_{\mathrm{Ps}}) = \sigma_{\mathrm{Ps}}(n_{\mathrm{H}}, l_{\mathrm{H}}; n_{\mathrm{Ps}}, l_{\mathrm{Ps}}) \frac{K_e(2l_{\mathrm{H}} + 1)}{2K_{\mathrm{Ps}}(2l_{\mathrm{Ps}} + 1)} \tag{9}$$

where K_e and K_{Ps} are the positron and Ps kinetic energies. These are related via energy conservation in the Ps formation collision as

$$K_e - \frac{R}{n_{\mathrm{H}}^2} = K_{\mathrm{Ps}} - \frac{R}{2n_{\mathrm{Ps}}^2}, \tag{10}$$

where R is the Rydberg energy (13.6 eV). Accurate values for Ps formation cross sections in $e^+ - \mathrm{H}$ collisions are available. Exemplars from recent work are those of Kadyrov and Bray [Kadyrov 2002] who have produced values for Ps(1S), Ps(2S) and Ps(2P) formation from collisions of positrons with H(1S). Thus, cross sections for the production of ground state antihydrogen from antiproton collisions with ground and first excited state Ps can be obtained with confidence. In order for $\overline{\mathrm{H}}^+$ to be formed according to reaction (7) the antihydrogen must be in its ground state, since otherwise there is much excess energy to be removed.

Figure 33 shows the cross sections obtained (we note that they are somewhat smaller than the experimental values of Merrison and co-workers [Merrison 1997] as the latter are total H formation cross sections, whereas the theory is for the H(1S) state only). They have been plotted against $\overline{\mathrm{p}}$ speed, v, in units of the quasi-classical speed of the positron in the Ps atom, v_e, as a universal scale. The latter is given by

$$v_e = \left(\frac{Re}{mn_{\mathrm{Ps}}^2}\right)^{1/2} \sim \frac{1.55 \times 10^6}{n_{\mathrm{Ps}}} \mathrm{m\,s}^{-1} \tag{11}$$

where m and e are the positron mass and charge (the equivalent $\overline{\mathrm{p}}$ energy scale is also given). Thus, a confident value of the cross section $\sigma_{\overline{\mathrm{H}}(1)}$ is about $5 \times \pi a_0^2 = 4.4 \times 10^{-16} \mathrm{cm}^2$.
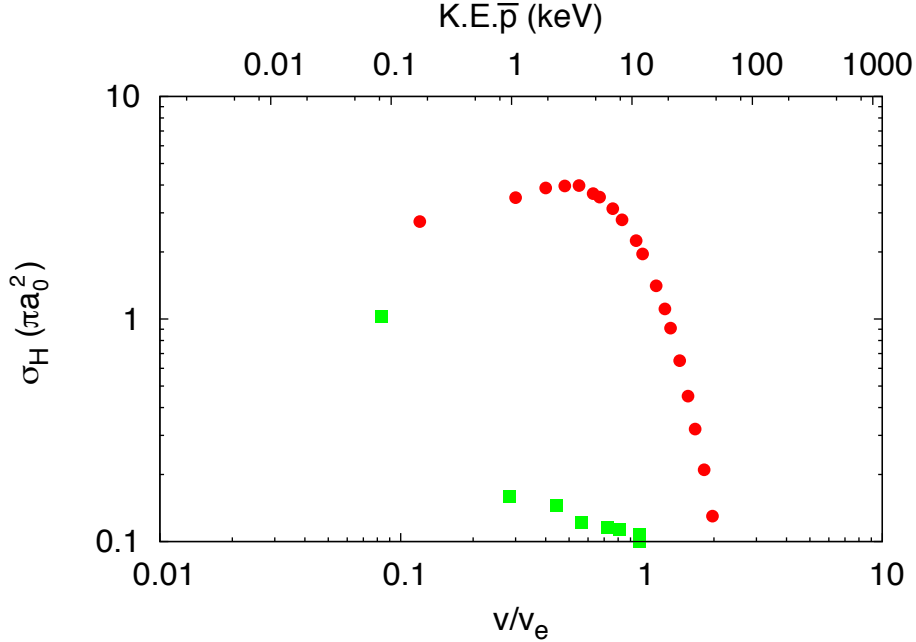
Figure 33: σ_H versus $\overline{p}$ speed and kinetic energy. Cross sections are for collisions with Ps(1S) (circles) and Ps(2S + 2P) (squares) producing $\overline{H}$(1S).

This value is in very good agreement with the result of [Mitroy 1995] (see Fig. 1 of this reference, where the energy is given in the center of mass, about 1.1 eV in our case for a 1 keV $\overline{p}$ beam).

From the figure it is clear that formation of ground state $\overline{H}$ from collisions involving excited states of Ps is depressed, except when v, or equivalently κ, goes to zero, as discussed by Humberston et al. [Humberston 1987]. A similar conclusion was found earlier in a less elaborate calculation by Mitroy and Stelbovics [Mitroy 1994]. Nevertheless, for $\overline{H}^+$ formation, a fraction of the positronium will be excited to the 3D level. In this case, the cross section of reaction (6) is increased by two orders of magnitude [Mitroy 1995], but $\overline{H}$ is produced in the $n_H = 3 - 7$ states. The radiative lifetimes of these states are longer than the transit time of the $\overline{p}$ in the cloud of positronium (about 20 ns), except for the 3P level (life time of 6 ns). From the result of reference [Mitroy 1995] (Fig. 6), we estimate that this process increases the production of 1S $\overline{H}$ by a factor of 3. This factor is not taken into account in the following to get a conservative estimate of the $\overline{H}^+$ production.

A 3D excited state Ps target is proposed for $\overline{H}^+$ formation. The binding energy of the $n_{Ps} = 3$ states is very close to that of $\overline{H}^+$ (from $\overline{H}$) and is around 0.75 eV. This should make the process near-resonant, potentially with a very high cross section. Unfortunately there are no calculations of $\sigma_{\overline{H}^+}$ for this target state, but a calculation has been performed for Ps in the 2S and 2P states by Roy and Sinha [Roy 2008] which shows a dramatic enhancement of the cross section at low energies (below about $K_{Ps} = 5$ eV), with the increase greater as the energy is lowered. For the following estimation we adopt the conservative value $\sigma_{\overline{H}^+(3)} \simeq 100 \times \pi a_0^2 = 8.8 \times 10^{-15} \text{cm}^2$, which is similar to that of reference [Roy 2008] for the 2P positronium state.

We now go on to compute the number of antihydrogen ions that can be produced, $N_{\overline{H}^+}$, from a $\overline{p}$ number, $N_{\overline{p}}$ colliding with a Ps target which has a density, $n = n_{Ps(1)} + n_{Ps(3)}$ formed from a mixture of 1S and 3D states. The target length is L. It can easily be shown that the two succcessive collisions of reaction (6) and (7) result in a $\overline{H}^+$ yield which can be written as follows:

$$N_{\overline{H}^+} = N_{\overline{p}} n_{Ps(1)} n_{Ps(3)} \sigma_{\overline{H}(1)} \sigma_{\overline{H}^+(3)} L^2/2. \tag{12}$$

We suppose that, after the laser excitation, the 1S and 3D states are equally populated. With $n = 10^{12}$ cm^{-3}, $L = 1$ cm, and the cross sections given above, we obtain finally 5 $\overline{H}^+$ per 10^7 $\overline{p}$.

In table 1, page 6, the number of $\overline{H}^+$ per pulse is much lower because of the effective Ps density and the lower $\overline{p}$ number.

This result is very conservative, because i) we have not taken into account the $N_{\overline{H}}$ formation due to the radiative decay of the 3P state ii) for Ps(3D), the cross section is probably considerably greater than for the Ps(2P). A low energy $\overline{p}$ beam is favorable and it the reason why we take 1 keV as the working value in this proposal. A more precise calculation will be done for the $\overline{H}^+$ production cross section as is discussed in the next paragraph.

9.2 $\overline{H}^+$ production cross section calculations

A crucial issue for the project is to estimate for reaction (6) which positronium states (n_{Ps}, l_{Ps}) lead to the largest amount of antihydrogen in the final channel. It is also relevant and of primary importance to look at which states (n_H, l_H) the residual $\overline{H}$ is produced.

In order to produce quantitative and meaningful theoretical predictions for the collisional processes (6) and (7) we propose to work within the framework of the Continuum Distorted Wave-Final State (CDW-FS) model. This approach has been successfully applied in the past to study charge exchange with positronium formation in collisions of positrons with atomic [Fojón 1996, Fojón 1997, Fojón 1998], molecular [Hervieux 2006] and metal cluster [Fojón 2001] targets. In most cases the theoretical predictions compared with success to available experimental data. It is worth mentioning that for the sake of theoretical consistency, the same approach must be used for modelling the two reactions since there are coupled together.

Concerning the process (6) a *three-body* $(\overline{p}, e^+, e^-)$ version of CDW-FS model will be used and partial cross sections for selective initial states of the Ps atom and final states of the residual antihydrogen product will be computed by using a powerful partial-wave technique.

Reaction (7) is by far more involved than the previous one since it implies four particles in mutual interaction $(\overline{p}, e^+, e^+, e^-)$. In the past, a *four-body* version of the (CDW-FS) model has been developed by us in order to study positronium formation in the transfer-excitation reaction of positrons impacting on He-like targets [Hanssen 2000, Hanssen 2001, Fojón 2002]. This model will be adapted to the present situation.

10 Laser excitation of positronium
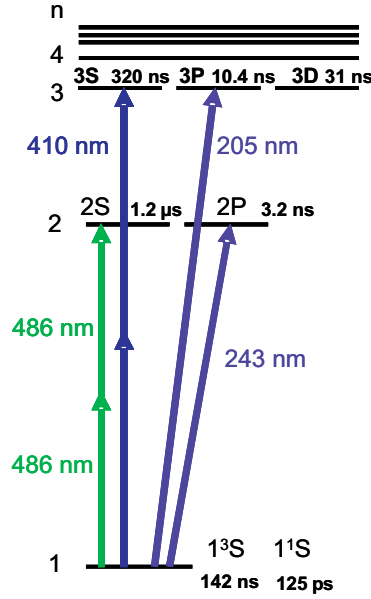
Figure 34: Energy levels of positronium.

In positronium the transition energies are about the half of those in hydrogen. The first optical transitions are depicted in Fig. 34. By comparison with hydrogen the radiative life times and the electric dipoles are twice as large. To excite the positronium, an important difficulty is due to the Doppler effect. Indeed, at a thermal temperature of 300 K, the velocity of the positronium is about 50 kms^{-1}, corresponding to a Doppler shift of 170 GHz for the Lyman-α transition at 243 nm. This requires a very broad band laser and it would be very difficult to excite all the positronium atoms in a thermal ensemble. The solution is to use a Doppler free two-photon excitation with two counter-propagating laser beams: then the first order Doppler effects are opposite for the two beams and cancel. From the 1S level it is possible to excite the 2S level or the 3S/D levels with two photons at 486 nm and 410 nm (see Fig. 34).

The two-photon transition probability is given by:

$$\Gamma_g = \frac{n^2 \omega^2}{\varepsilon_0^2 \hbar^2} \left| \sum_r \frac{\langle e | \mathbf{d}.\varepsilon | \mathbf{r} \rangle \langle \mathbf{r} | \mathbf{d}.\varepsilon | \mathbf{g} \rangle}{\omega - \omega_{rg}} \right|^2 \frac{\Gamma_e}{\left(2\omega - \omega_{eg}\right)^2 + \left(\frac{\Gamma_e}{2}\right)^2} \tag{13}$$

where n is the number of photons per unit volume for each counter-propagating wave, ω the laser frequency, ε the polarisation, $\omega_{ij} = (E_i - E_j)/\hbar$, $\mathbf{d}$ the electric dipole moment operator and Γ_e the natural width of the excited state (we suppose that the natural width of the state $|g\rangle$ is negligible). The summation is made over all the possible states $|r\rangle$ (including the continuum). We introduce the two-photon operator Q_{tp}. For a polarisation along the z axis, Q_{tp} is given in atomic units ($\hbar = \alpha c = m = 1$) by:

$$Q_{tp} = \sum_r \frac{z |r\rangle \langle r| z}{\omega - \omega_{rg}} \; . \tag{14}$$

51

Transition	Hydrogen	Positronium
1S-2S	7.85	62.8
1S-3S	2.14	17.12
1S-3D	5.87	46.98

Table 5: Matrix element $\langle e\,|Q_{tp}|\,g\rangle$ of the 1S-2S, 1S-3S and 1S-3D two-photon transitions in hydrogen and positronium (atomic units).

With this notation, equation (13) becomes:

$$\Gamma_g = \left(\frac{4\pi a_0^2}{mc^2\alpha}\right)^2 \times |\langle e\,|Q_{tp}|\,g\rangle|^2 \times \frac{\Gamma_e I^2}{\left(2\omega - \omega_{eg}\right)^2 + \left(\frac{\Gamma_e}{2}\right)^2}, \tag{15}$$

where I is the power density of the light ($I = n\hbar\omega/c$), a_0 the Bohr radius, α the fine structure constant and m the electron mass. Taking into account the laser bandwidth $\Delta\nu$ (in Hz), the two-photon transition probability is at resonance:

$$\Gamma_g = 2\pi \left(\frac{4a_0^2}{mc^2\alpha}\right)^2 \times |\langle e\,|Q_{tp}|\,g\rangle|^2 \times \frac{1}{\Delta\nu} \times I^2. \tag{16}$$

The value of the first factor of equation (16) is 2.2085×10^{-9} in SI units. In hydrogen, the values of the matrix element of the two-photon operator are well known [Gontier 1971]. Because of the scaling laws between positronium and hydrogen, these matrix elements are eight times larger in positronium (see Table 5).

10.1   Excitation of the 1S-3S transition

The natural width of the 1S-3S line is mainly due to the lifetime of ortho-positronium (142 ns). As a result we have to excite the transition during a shorter time τ. In this case, the laser frequency width is $\Delta\nu = 1/(2\pi\tau)$. To excite a large proportion of atoms we have the condition $\Gamma_g\tau = 1$ and the required laser intensity is:

$$I = \left(\frac{1}{2\pi \left(\frac{4a_0^2}{mc^2\alpha}\right)^2 \times |\langle e\,|Q_{tp}|\,g\rangle|^2 \times 2\pi\tau^2}\right)^{1/2} = \frac{1}{8\pi \left(\frac{a_0^2}{mc^2\alpha}\right) |\langle e\,|Q_{tp}|\,g\rangle|\,\tau}. \tag{17}$$

The energy of the laser pulse $I\tau S$ is independent of the duration τ (S is the section of the laser beam). With $S = 1\text{mm}^2$, we need a pulse energy of about $500\,\mu\text{J}$.

Unfortunately, we have also to take into account of the photo ionization of the 3S level. In a standing wave, the photoionization probability is:

$$\Gamma_{\text{photo}} = 4\pi \times \frac{a_0^2}{mc^2\alpha} \times \gamma_{\text{photo}} \times I, \tag{18}$$

where γ_{photo} is the imaginary part of the light shift of the 3S level in atomic units. In hydrogen, its value is 4.3148 (D. Delande, private communication). In positronium it is eight times larger. Finally the photoionization probability during the laser pulse is:
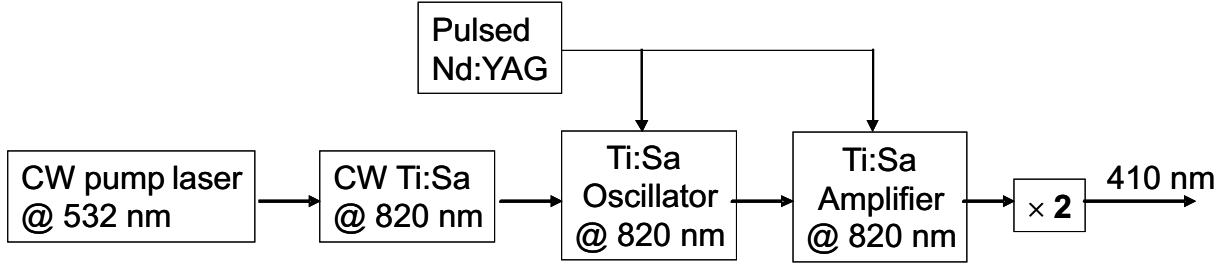
Figure 35: Scheme of the laser system for the excitation of the 1S-3D transition in positronium.

$$\Gamma_{\text{photo}}\tau = \frac{\gamma_{\text{photo}}}{2\,|\langle e\,|Q_{tp}|\,g\rangle|} \simeq 1. \tag{19}$$

In conclusion the photoionization of positronium is very important, and this state cannot be used to promote $\overline{H}^{+}$ formation.

10.2 Excitation of the 1S-3D transition

The case of the 3D excitation is more favorable. In the case of the excitation of the $3D_{5/2}$ fine structure level, equation (17) becomes:

$$I = \frac{1}{8\pi \left(\frac{a_0^2}{mc^2\alpha}\right)\sqrt{0.6}\,|\langle e\,|Q_{tp}|\,g\rangle|\,\tau}. \tag{20}$$

Then the required energy of the laser pulse is reduced to about $235\,\mu\text{J}$. For the 3D level, the coefficient γ_{photo} is 0.4584 in hydrogen and 3.6676 in positronium. Thus, the probability of photoionization during the laser pulse is:

$$\Gamma_{\text{photo}}\tau = \frac{\gamma_{\text{photo}}}{2\sqrt{0.6}\,|\langle e\,|Q_{tp}|\,g\rangle|} \simeq 0.1 \ . \tag{21}$$

In the case of the 3D excitation, the photoionization becomes negligible during the laser excitation.

10.3 Laser system

A schematic of the laser system is shown on Fig. 35. The 410 nm radiation is obtained by frequency doubling in a LBO crystal of a source at 820 nm. This source includes a Ti:Sa oscillator and a Ti:Sa amplifier. The short cavity length of the Ti:Sa oscillator (7 cm) guarantees a typical pulse width of 10 ns and a power of about $500\,\mu\text{J}$. The wavelength of the system is precisely controlled thanks to a continuous wave titanium sapphire laser which seeds the Ti:Sa oscillator. After the amplifier, the pulse energy will be a few mJ to obtain a typical pulse energy of 1 mJ at 410 nm.

11 Capture and cooling of the $\overline{\mathrm{H}}^+$ ion

This section describes the methods and apparatus that are proposed to capture and cool the $\overline{\mathrm{H}}^+$ ions. The ions are first captured and decelerated to 10 eV. Then, they have to be cooled to a few neV. This is very challenging since the temperature has, eventually, to be decreased over ten decades. Since only a few $\overline{\mathrm{H}}^+$ ions per bunch are expected, high efficiency capture and cooling processes are required. Several cascaded devices will be necessary to capture and cool the ions to progressively lower and lower temperatures, and a possible scheme is illustrated schematically in Fig. 36. This involves:

- $\overline{\mathrm{H}}^+$ stopping and capture using a high voltage-biased linear octupole guide and RF quadrupole trap;

- $\overline{\mathrm{H}}^+$ transfer to a segmented linear trap for sympathetic cooling to the 50 mK range by laser cooled Be^+ ions;

- Single $\overline{\mathrm{H}}^+$ transfer to a precision trap for sub-Doppler sympathetic cooling by Doppler side band and Raman side-band cooling before photodetachment of the excess positron.
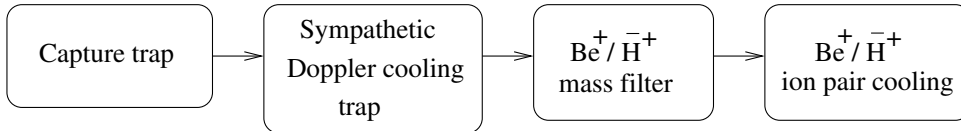
Figure 36: Simplified sketch of the capture and cooling devices.

The feasibility of each step is analyzed, showing that the $\overline{\mathrm{H}}^+$ capture and cooling is possible within a few seconds. In this scheme, the number of cold $\overline{\mathrm{H}}^+$ is reduced to a maximum of one per pulse, since the sub-Doppler cooling can only be performed with a single ion. In case the $\overline{\mathrm{H}}^+$ production rate could be pushed to much more than such a rate, successive transfer processes (third step above) of a single ion between two AD/ELENA pulses may be possible, but this is not taken as the baseline hypothesis.

11.1 $\overline{\mathrm{H}}^+$ beam characteristics

We assume here that antiprotons extracted from ELENA are not stored into an intermediate trap, so that the beam characteristics correspond to those given in section 7. The $\overline{\mathrm{H}}^+$ ions are obtained downstream of the $\overline{\mathrm{p}}$ and Ps interaction region with a kinetic energy in the keV range. The energy spread is mainly determined by that of the incoming $\overline{\mathrm{p}}$. The slow $\overline{\mathrm{p}}$ source ELENA is expected to deliver a beam with a relative momentum spread $\delta p/p \approx 10^{-4}$ at $p = 13.7$ MeV/c. The corresponding longitudinal relative kinetic energy spread is 2×10^{-4} corresponding to $\delta E_c \approx 20$ eV. After deceleration, the transverse divergence is 8 mrad, and the transverse kinetic energy 8 eV (see section 7).

11.2 $\overline{\mathrm{H}}^+$ Capture

For the discussion in this section, we take 1 keV for the kinetic energy of the $\overline{\mathrm{p}}$ as a reference value. The $\overline{\mathrm{H}}^+$ ion bunch is produced in a $(3 \text{ mm})^3$ size volume within 300 ns, with an energy spread δE_c of about 20 eV in the longitudinal direction and 8 eV in the transverse direction. These orders of magnitude allow for efficient injection and trapping in a linear radio-frequency quadrupolar trap (RFQ). Fig. 37 shows a simplified scheme
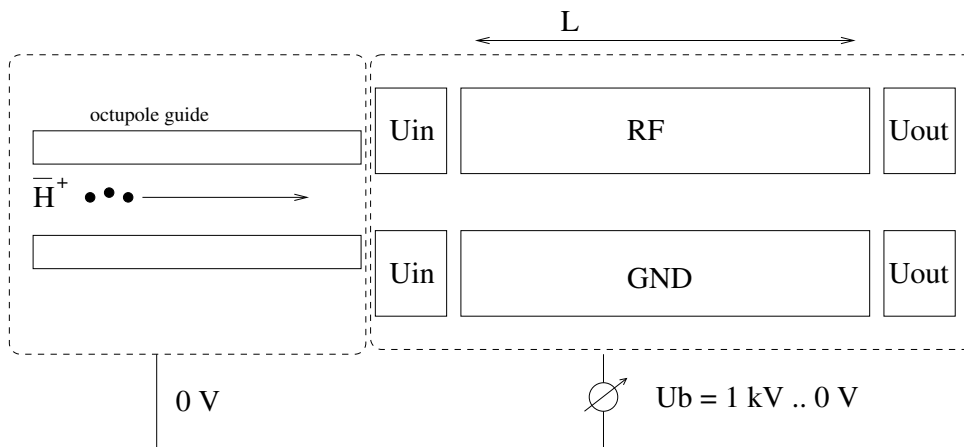
Figure 37: Octupole guide and biased RFQ trap used to decelerate and trap the $\overline{\mathrm{H}}^+$ ion bunch.

of an octupole guide and a biased linear quadrupole trap [Schiller web]. The electrode voltages are defined with respect to a bias voltage $U_b \approx (E_c - \delta E_c)/e = 980$ V to slow down the ions. For an inner diameter $R_0 = 5$ mm, a RF voltage $V_{RF} = 533$ V at 13 MHz, a 40 eV radial potential depth is obtained allowing radial confinement in the trap with a stability parameter $q_x = 0.6$ (see section 11.7). By setting the input electrode voltage U_{in} to U_b, the ions will enter the trap. By setting the output electrode to U_{out} larger than $U_b + (\delta E_c)/e = 1020$ V, all the ions will be reflected at the output. By raising the input electrode voltage to U_{out} at time t_{close} before the ion bunch leaves the trap, the ions will be longitudinally trapped. In order to obtain a high capture efficiency, the ion round-trip time τ in the trap must be longer than both the ion bunch duration $\tau_{bunch} = 150$ ns and the U_{in} raising time that is of order 10 ns. This sets a lower limit on the trap length L. Assuming a flat DC potential along the trap axis and $\tau = 150$ ns, one obtains $L > \tau\sqrt{2\delta E_c/m} = 10$ mm [Bussmann 2006]. These orders of magnitude show that a trap of a few cm length is sufficient.

The capture process has been simulated using SIMION8.0 software to analyse the acceptance of the capture in terms of the trap closure time t_{close} for several input $\overline{\mathrm{H}}^+$ ion bunch durations, and of the kinetic energy spread and angular spread of the incoming $\overline{\mathrm{H}}^+$ beam. The $\overline{\mathrm{H}}^+$ ions are initialized near the trap axis and distributed on a disk of radius $r_i = 1$ mm, with a Gaussian kinetic energy spread of FWHM δE_c, a conical momentum distribution of half-angle θ and an arrival time distribution width δt_a. Fig. 38 shows the dependence of the capture efficiency versus t_{close}, θ and δ_{Ec}, evidencing a nearly 100 % capture efficiency for parameter ranges which cover their expected values. The simulation parameters are given in the figure caption.
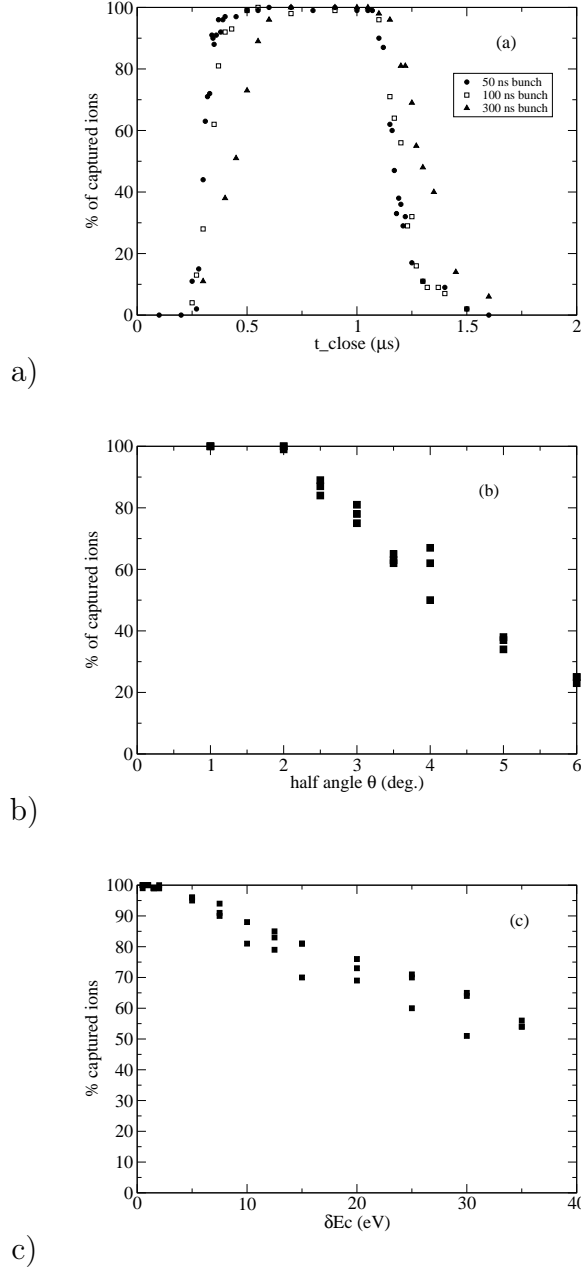
Figure 38: a) $\overline{H}^+$ capture efficiency versus the capture trap closing time t_{close}. The simulation parameters are $E_c = 1\text{keV}$, $\delta E_c = 1$ eV, $U_b = 980\,\text{V}$, $U_0 = 100\,\text{V}$, $\Omega = 2\pi \times 16\,\text{MHz}$, $V_0 = 600\,\text{V}$, $\theta = 1\,\text{degree}$. The octupole voltages are all set to zero Volt; the simulation time is $10\,\mu s$. b) $\overline{H}^+$ capture efficiency versus the input beam half divergence angle θ; $t_{close} = 0.9\,\mu s$. (c) $\overline{H}^+$ capture efficiency versus initial kinetic energy spread δE_c; $t_{close} = 0.9\,\mu s$.

Once the $\overline{H}^+$ ions are trapped, the bias voltage U_b is lowered to ground. Since the ion dynamics in the trap only depend on the electric field, and not on the voltages, the ions remain trapped. In a Paul trap the equilibrium temperature is roughly given by one tenth

of the trap depth because of RF heating, i.e. about 10 eV or a few 10^5 K [Church 1969].

11.3   Sympathetic cooling to mK temperatures

The next step involves cooling the $\overline{\text{H}}^+$ ions. The standard technique of buffer gas cooling using helium that allows ion cooling to room temperature (a few K in a cryogenic environment) does not apply with antimatter. Resistive cooling has been applied in a RF Paul trap to cool protons [Church 1969]. However, the competition between cooling and RF heating results in a temperature only three time smaller when compared to uncooled ions. The only way to cool ions down to a few mK (a few times 10^{-7} eV) is to use sympathetic cooling by laser cooled ions.

11.3.1   Laser Doppler cooling

A number of ion species (^{9}Be$^+$, ^{24}Mg$^+$, ^{40}Ca$^+$, ^{87}Sr$^+$, ^{137}Ba$^+$, ^{171}Yb$^+$) can be directly laser cooled using a cycling transition of width Γ. Under optimum cooling conditions (laser detuning $\delta_L = \Gamma/2$ and laser intensity smaller than, but of the order of, the saturation intensity $I_{sat} = 82$ mW cm^{-2}), the ion cloud temperature is given by $k_B T_D = \hbar\Gamma/2$.

In the case of ^{9}Be$^+$, the transition wavelength is $\lambda = 313$ nm. The width is $\Gamma = 2\pi \times 19.4$ MHz, yielding $T_D = 0.5$ mK. At such low temperatures, the Coulomb repulsion energy dominates the kinetic energy and the ion cloud is organized in a so called Coulomb or Wigner crystal.

11.3.2   Sympathetic cooling

Most of the X$^+$ ionic species, e.g. $\overline{\text{H}}^+$, have no transition allowing for direct laser cooling. Sympathetic cooling consists of simultaneously trapping a laser cooled ion cloud with X$^+$ ions. The combined effect of the trapping potential, of Coulomb interaction and of laser cooling is to cool all the ions. The final temperature is larger than the Doppler limit, T_D, but usually in the 5-100 mK range. Since the trapping potential is steeper for light species, sympathetic cooling results in a kernel made of the lightest ions surrounded by the heavier ones.

Both species have to be simultaneously stable in the RF Paul trap, so they must have similar mass to charge ratios. As a consequence, we will use laser cooled ^{9}Be$^+$ for $\overline{\text{H}}^+$ sympathetic cooling, as demonstrated on H$_2^+$ and HD$^+$ in S. Schiller's group at Düsseldorf University [Blythe 2005].

11.3.3   Sympathetic cooling time

Ion sympathetic cooling has been demonstrated in a large number of experiments with trapping times of the order of a few hours. The characteristic cooling times for initially hot ions is an issue that has not been addressed in detail. Numerical simulations of ion sympathetic cooling dynamics have been published, with sympathetic cooling times in the ms range [Baba 2002, Bussmann 2006]. In the latter reference, the stopping power of a 100 000 ^{24}Mg$^+$ laser cooled ion plasma has been investigated for highly charged ions (HCI) with a mass to charge ratio of $m/q = 2.5$, in a situation comparable to that of the $\overline{\text{H}}^+$/Be$^+$ couple. Stopping times of less than 1 ms are obtained for initial kinetic energies smaller than 0.4 eV.

This order of magnitude makes us optimistic of the feasibility of hot $\overline{H}^+$ sympathetic cooling within 1 s. Nevertheless, this is an important issue for the present project and also for other projects aiming at trapping and cooling highly charged ions (HCI) such as $^{40}Ar^{13+}$ for QED tests by high resolution spectroscopy or for fundamental constant variation tests and optical clock applications [Schiller 2007].

Numerical simulation is a powerful tool to determine the optimum conditions for fast $\overline{H}^+$ ion cooling by a cold Be^+ plasma. The exact Coulomb interaction and the actual potential including the RF time dependence and the associated micro-motion have to be taken into account. This results in simulation times scaling as N^2 where N is the number of ions. Simulation of a few thousand laser cooled ions and a few sympathetically cooled ions during 100 ms is feasible within a reasonable amount of time (one week) using standard clusters of computers. This work has been started recently at LKB.

From the experimental point of view, several projects involving sympathetic cooling of HCI are starting, e.g. at Kastler Brossel laboratory (Paris) and will shed light on this issue.

11.3.4 Sympathetic cooling implementation

The preparation of a Doppler cooled Be^+ cloud requires a few seconds, mainly due to the Be^+ loading time. To save time and reduce $\overline{H}^+$ losses, the $\overline{H}^+$ ions will be loaded from the capture trap into a segmented linear trap with two trapping zones as shown in Fig. 39. The segmented trap will be operated with DC and RF voltages similar to that of the capture trap. A Doppler cooled Be^+ ion cloud made of thousands of ions is prepared in zone B. For a given geometry and RF field, the Be^+ radial trapping depth is 9 times smaller than that of $\overline{H}^+$ (see eq. (22) and (23) in section 11.7). The hot $\overline{H}^+$ ions are injected in zone A. If the trapping depth in zone A is large enough, the $\overline{H}^+$ ions do not interact with the laser cooled Be^+ ions. By slowly (when compared to the sympathetic cooling time) raising zone A base potential U_A, the $\overline{H}^+$ ions will enter zone B, overlap with the Be^+ cloud and be sympathetically cooled [Bussmann 2006]. The expected $\overline{H}^+$ temperature is in the few mK range.
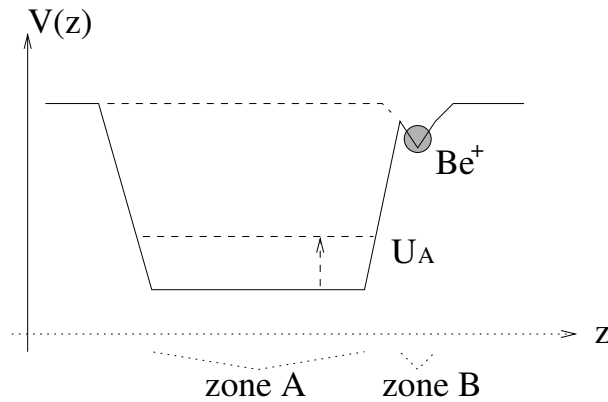

Figure 39: Longitudinal profile of the potential in a segmented ion trap with two trapping zones A and B (see text).

11.4 Cooling to neV energies

11.4.1 Quantum harmonic oscillator

For the free fall studies, the $\overline{H}^+$ ions must have an initial velocity in the 1 ms^{-1} range at most. This corresponds to a *mean kinetic* energy of only 5 neV, well below the temperatures observed in Doppler cooled ion clouds since 1 mK corresponds to 86 neV.

An ultra-cold ion in an harmonic potential must be represented as a quantum harmonic oscillator. For a 1D quantum harmonic oscillator of mass m and eigenfrequency ω, the energy quantum is $\hbar\omega$ and the position, momentum and velocity spreads in the fundamental state $|0\rangle$ are given by $\Delta x = \sqrt{\hbar/2m\omega}$, $\Delta p = \sqrt{m\hbar\omega/2}$ and $\Delta v = \sqrt{\hbar\omega/2m}$. The mean kinetic energy in the fundamental state is $K = \hbar\omega/4$. Assuming a $\overline{H}^+$ is confined with an angular oscillation frequency $\omega = 2\pi\times$ 20 MHz, one obtains $\hbar\omega = 82.4$ neV, $\Delta x = 16$ nm, $K = 20.6$ neV and $\Delta v = 2$ m/s. Finally, the recoil energy for a Be$^+$ ion absorbing a 313 nm photon is $E_{recoil} = h^2/(2m_{Be}\lambda^2) = 8.3$ neV.

These orders of magnitude show that the $\overline{H}^+$ ions have to be prepared in the fundamental state of the harmonic well in which they are trapped. This is not possible using ion clouds and is only possible with a few ions in the trap. The first demonstration of 3D zero-point energy cooling of a trapped ion was performed in 1995 in D. Wineland's group using Raman sideband cooling of a single Be$^+$ ion [Monroe 1995]. This challenging technique has been extended to sympathetic cooling in an ion pair [Barrett 2003], for linear ion chain cooling for high fidelity quantum gate demonstration [Benhelm 2008] and then applied to Be$^+$/Al$^+$ or Mg$^+$/Al$^+$ ion pair sympathetic cooling for optical clock applications [Schmidt 2005, Rosenband 2008].

11.4.2 Raman sideband cooling

A Doppler cooled ion confined in a harmonic trap is an harmonic oscillator with a mean excitation number n of few tens or few hundred vibration quanta ω_{vibr}, depending on the trap stiffness. The first step consists in using resolved sideband Doppler cooling in a trap strong enough that $\omega_{vibr} \approx \Gamma$ [Diedrich 1989]. In the case of Be$^+$ ions, the vibration angular frequencies ω_{vibr} must be in the 20 MHz range. This requires driving RF frequencies around 200 MHz with voltages in the 500 V range in a mm size trap. It has been demonstrated that the ion spends most of the time ($\approx 95\%$) in the lowest vibrational level $n = 0$ [Monroe 1995].

To further cool down the ions, one has to decrease the vibrational number ideally to 0 using Raman sideband cooling. Fig. 40 shows the Be$^+$ electronic energy levels and the vibrational levels corresponding to the confinement in one of the principal directions of the trap. The idea of Raman sideband cooling is to drive stimulated Raman transitions between state $|F = 2, n\rangle$ to $|F = 1, n - 1\rangle$ and spontaneous Raman transitions from $|F = 1, n - 1\rangle$ to $|F = 2, n - 1\rangle$ using so called Raman pulses. As a result, the vibrational number is decreased by one unit. By repeating this procedure, one can prepare the ion in the fundamental vibration level. More precisely, but disregarding the laser polarization configuration and Zeeman sub-levels, the stimulated Raman transition is driven by the counter-propagating beams R$_1$ and R$_2$ with Raman lasers far detuned from the 2S→2P transition to avoid spontaneous emission, with frequencies satisfying the resonance condition $\omega_{R_1} - \omega_{R_2} = \omega_{hfs} + \omega_{vibr}$. The spontaneous Raman transition is driven by the D$_1$ beam. In the Lamb-Dicke regime where $\hbar\omega_{vibr} \gg E_{recoil}$ (or equivalently

$\Delta x \ll \lambda/2\pi$), the spontaneous emission mainly occurs with Δn=0. Raman sideband cooling thus requires high vibration frequencies, i.e. a very steep trapping potential.
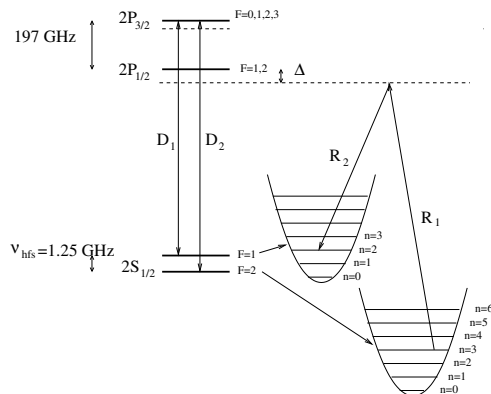
Figure 40: Be^+ energy levels, including the harmonic oscillator energy of the center of mass motion in one of the principal directions of the trap. D_1 and D_2 are the Doppler cooling and repumping beams. R_1 and R_2 are the Raman excitation beams. All optical transitions are near $\lambda \approx 313$ nm. n is the vibrational quantum number.

In an actual trap, the three vibrational eigen-frequencies are different. 3D zero-point energy cooling is achieved by using Raman beams directed at oblique angle to all the principal directions of the trap and by alternating cooling sequences for each vibration mode.

Once the ion pair is cooled to the zero-point energy, the trap stiffness can be adiabatically decreased to $\omega_x \approx 1$ MHz, resulting in a velocity spread below 1 ms^{-1} (kinetic energy of 1 neV or 12 µK).

11.4.3 Raman sideband cooling of an ion pair

The Raman sideband cooling method described above also applies to an ion pair with a laser cooled ion and a sympathetically cooled ion. Both ions are coupled harmonic oscillators with six eigen-frequencies instead of three. In the case of the GBAR experiment, the $\overline{\mathrm{H}}^+$ ion has to be cooled to the zero-point energy at least in the vertical direction.

11.4.4 Raman transition probabilities

Stimulated Raman transition rates are proportional to $\Omega_1\Omega_2^*/\Delta$ where Ω_1 and Ω_2 are the Rabi frequencies for R_1 and R_2 transitions and Δ is the detuning [Moler 1992] (see Fig. 40). With a detuning $\Delta = 12$ GHz and optical powers of a few mW only, the Raman pulses are shorter than 1 ms [Monroe 1995] and the stimulated/spontaneous Raman cycles can be repeated at kHz rates resulting in a fast cooling process.

11.5 Ion pair trap

The ion pair sub-Doppler cooling process requires a much steeper trap than the capture and sympathetic cooling process, since the radial macro motion frequency must be larger than the Be^+ cooling linewidth. A mini RF trap with an inner radius of a few mm and

operated with RF voltages in the 100-200 MHz, 500 V range will be implemented next to the Doppler cooling trap. One $\overline{\text{H}}^+$ ion will have to be extracted from the Doppler cooling trap and injected into a mini RF trap containing a single sub-Doppler cooled Be^+ ion, without heating to much the ions. Single ion shuttling processes have been studied and demonstrated in the frame of quantum computing experiments [Hucul 2008]. The trap confinement potential and the Coulomb interaction will lead to the formation of a ion pair.

In the single ion or ion pair regime, the system will be monitored using high spatial resolution imaging optics ($< 1\,\mu$m) and UV enhanced CCD detectors. The transition from a single Be^+ ion to a $Be^+/\overline{\text{H}}^+$ ion pair will be clearly evidenced by a spatial displacement of the fluorescent Be^+ ion.

11.6   Cooling laser system

Be^+ laser cooling requires cw optical power of a few mW at $\lambda = 313.13$ nm, and a few hundreds of μW detuned by 1.25 GHz corresponding to the ground state hyperfine splitting. No cw laser sources are commercially available at this wavelength, but several solutions exists that can be developed at Kastler-Brossel Laboratory. 313 nm radiation can be produced by frequency doubling a cw dye laser at 626.26 nm [Wagstaff 1979, Larson 1986], or by frequency mixing of a frequency doubled Nd:YAG laser at 532 nm and an IR diode laser at 761.1 nm [Schnitzler 2002]. Recently, taking advantage of periodically poled lithium niobate crystals (PPLN) and highly stable fiber laser sources, new solutions have been demonstrated. For instance, the 626 nm dye laser can be replaced by the sum frequency mixing of two fiber lasers at 1550 nm and 1051 nm [Wilson 2011] resulting in up to 750 mW at 313 nm. Alternatively, high efficiency and cost-effective frequency quintupling of a single fiber laser at 1565.65 nm leading to 100 mW of optical power has been demonstrated [Vasilyev 2011]. The fiber laser is first frequency doubled at 782.83 nm in a single pass PPLN crystal. The fundamental and second harmonic are mixed in a second single pass PPLN crystal to produce the third harmonic at 521.88 nm. Sum frequency mixing of the second and third harmonic in a BBO crystal produces about 2 mW of optical power at 313.13 nm in a single pass configuration. By using a singly resonant enhancement Fabry-Perot cavity at 782.83 nm, up to 100 mW can be obtained. The laser frequency is stabilized by locking its third harmonic on a saturated absorption line near 521.88 nm in an iodine cell. The required frequency modulations (to produce a 1.25 GHz side band for Be^+ repumping and side bands for frequency stabilization) are produced using a phase modulator at the fundamental wavelength.

11.7   Linear quadrupole trap

Fig. 41 shows a linear quadrupole trap made of four parallel cylindrical electrodes. For an inner trap radius R_0, a quasi-quadrupolar field is obtained with the optimum cylinder radius $R = 1.147\,R_0$ [Denison 1971]. The radial confinement is due to the quadrupolar RF field. The stability parameter is given by

$$q_x = q_y = \frac{2qV_0}{m\Omega^2 R_0^2} \tag{22}$$
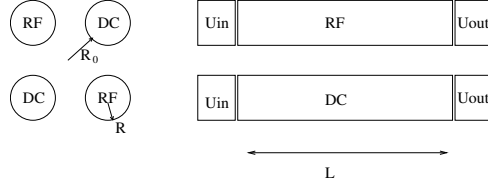
Figure 41: Typical geometry of a linear quadrupole trap.

where m and q are the ion mass and charge, $\Omega/2\pi$ is the RF field frequency and V_0 is the voltage difference between the quadrupole electrode pairs. For $0 \leq q_x \ll 0.9$, it results in an effective harmonic trapping potential with a depth given by

$$\Psi_x^{RF} = \Psi_y^{RF} = \frac{q_x V_0}{8} \tag{23}$$

and a radial oscillation frequency given by

$$\omega_x^{RF} = \omega_y^{RF} = \frac{\Omega q_x}{2\sqrt{2}}. \tag{24}$$

Given the stability parameter q_x and the trap depth Ψ_x^{RF}, the trap operation conditions are obtained by setting V_0 and Ω following

$$V_0 = 8\Psi_x^{RF}/q_x \tag{25}$$

$$\Omega = \sqrt{16q\Psi_x^{RF}/(mR_0^2 q_x^2)}. \tag{26}$$

With m=1.67 x 10^{-27} kg, q=1.6 x 10^{-19} C, R$_0$=5 mm, q_x=0.6 and Ψ_x^{RF}=40 V, one gets very reasonable orders of magnitude of V_0=533 V, Ω=13 MHz and ω_x^{RF}=2.8 MHz.

The longitudinal confinement is due to the end electrode DC voltage U_{out} and has a depth directly given by U_{out}. If the quadrupole electrode length is large compared to the inner radius r, the longitudinal DC potential close to the center of the trap is quasi-harmonic with a small curvature that can be written $m\omega_z^2 z^2/2$ where ω_z is the longitudinal oscillation frequency. The radial dependance of this DC potential is $-m\omega_z^2(x^2+y^2)/4$. With a long enough quadrupole electrode (say 10 cm), the longitudinal oscillation frequency can be made much smaller than the radial one, resulting in stable trapping.

11.8   Photodetachment at 313 nm

The last cooling steps of the $\overline{\mathrm{H}}^+$ ions involves first sympathetic cooling by laser cooled Be$^+$ ions and then Raman sideband cooling of a Be$^+$/$\overline{\mathrm{H}}^+$ ion pair. During these cooling steps, the $\overline{\mathrm{H}}^+$ ions will be illuminated by the cooling laser light at $\lambda = 313$ nm. It is thus important to evaluate the photodetachment probability at 313 nm from the data available for the H$^-$ ion.

The photodetachment cross section of H$^-$ has been evaluated and measured in the 1-3 eV photon energy range [Chandrasekhar 1958, Smith 1959]. From the published values $\sigma_{298.5\,\mathrm{nm}} = 1.83 \times 10^{-17}$ cm^2 and $\sigma_{357.0\,\mathrm{nm}} = 2.30 \times 10^{-17}$ cm^2, one finds $\sigma_{313\,\mathrm{nm}} \approx 2.0 \times 10^{-17}$ cm^2.

The Be^+ cooling transition saturation intensity is $I_{sat} = 2\pi^2 \hbar c\Gamma/3\lambda^3 = 82\,\text{mWcm}^{-2}$. The cooling laser beam flux is typically $I = 0.5$ mWmm^{-2}, corresponding to a photon flux $\Phi = I/hc = 7.85\ 10^{14}$ photon mm^{-2} s$^{-1} = 7.85\ 10^{16}$ photon cm^{-2} s^{-1}. The product $\sigma_{313\ nm}\Phi$ is 1.5 s^{-1}. This order of magnitude shows that UV driven photodetachment is an important issue that limits to about 500 ms the sympathetic cooling times during which the $\overline{H}^+$ ions can be immersed in the Be^+ plasma, so special care has to be taken for the Be^+ cooling laser beam. A cooling time of 500 ms or less is taken as a tentative hypothesis in table 1, page 6, where a cooling efficiency of 70 % has been assumed.

If it turns out that long cooling times are needed for the first cooling step, the 313 nm photodetachment probability will be reduced using the following solutions:

- Since the light $\overline{H}^+$ ions are expected to be located on the trap axis at the centre of the Be^+ cloud, a doughnut beam (TEM 01 Laguerre-Gaussian mode) can be used to cool the ions with no light on the beam axis.

- The Be^+ laser cooling efficiency is much higher than the Coulomb crystal RF heating rates. Consequently, the cooling laser can be applied with a duty-cycle of less than 50 %.

- For the last cooling step (capture by a single laser cooled Be^+ ion and Raman sideband cooling of the ion pair), the cooling laser can be tightly focused on the Be^+ ion with a beam waist of a few µm, smaller than the typical equilibrium distance between the ions. In such a configuration, the $\overline{H}^+$ ion coupling to the 313 nm cooling laser is minimized.

11.9   Work plan

The above sections show that $\overline{H}^+$ capture and cooling down to the µK regime is feasible. Nevertheless, the precise design of the capture, Doppler cooling and sub-Doppler cooling traps requires intense numerical simulations to optimize the trap geometry and operating conditions and the transfer protocols. The trapping potential will be simulated using SIMION8 software whereas ion cloud dynamic simulation will be obtained from LKB developed code.

From the experimental point of view, the different trap and protocols will be validated using standard matter i.e. protons that can easily be produced at low energy from H_2 molecules using standard ion sources, and that have the same charge and mass as $\overline{H}^+$.

12 Photodetachment of the excess positron of $\overline{\mathrm{H}}^+$

In order to perform the measurement of the free fall of the $\overline{\mathrm{H}}$ atom, the last step is to photodetach the excess positron of the $\overline{\mathrm{H}}^+$ ion. In this section, we discuss the resulting momentum kicks on the ion due to the photon absorption and the positron emission, and the consequences on the laser system to be used in order to reach the foreseen precision of the measurement. As described in the previous sections, the production of $\overline{\mathrm{H}}^+$ ions is made by accumulating enough positrons that are then sent onto a small porous silicate target to produce a dense cloud of positronium with which the antiprotons interact. The assumed accumulation time of the positrons used to form the Ps target is several minutes. Part of this time is available to photodetach the $\overline{\mathrm{H}}^+$ ions produced. The technique we describe here is to do the photodetachment very close to threshold, leading to a very low cross section, by using a sufficiently powerful laser system to limit the resulting recoil to facilitate the measurement with the desired precision.

12.1 Effect of the absorption of the photon

We assume that the $\overline{\mathrm{H}}^+$ ions are trapped and cooled down to a temperature of about 20 µK. This temperature corresponds to a typical speed of about 1 ms^{-1} or a potential energy corresponding to a change of about 10 cm in altitude. The binding energy of the H$^-$ (or $\overline{\mathrm{H}}^+$) ion is 0.76 eV (1.64 µm wavelength). When the ion absorbs a 1 eV photon for example, it gets a 1 eV/c momentum kick, and recoils with 0.3 ms^{-1} speed ($v_{recoil} = p_{recoil}/m_H$). A two photon photodetachment would avoid this recoil but the rate is quite low, of order 10^{-10} s^{-1}(Wcm^{-2})$^{-2}$ [Crance 1985]. However a 15 cm free fall (the typical size we will keep for this discussion) takes 0.17 s (if g=ḡ !), so this recoil causes only a few cm horizontal translation and can be accommodated for the detection. In conclusion, a two-photon photodetachment process is not necessary; it is enough to shoot the photodetachment laser beam horizontally.

12.2 Detachment of the positron

When the positron is emitted, its kinetic energy is equal to the excess energy of the photon ΔE (the photon energy minus the binding energy). The plot below (figure 42) gives the atom recoil speed in m s^{-1} as a function of the excess energy of the photon in eV. One can see that the laser wavelength must be adjusted to better than a few µeV above threshold to get a speed of order of the initial temperature. However, the detachment cross-section strongly decreases close to the threshold. An optimum must be found between a small recoil velocity and a large enough photodetachment rate.

The detachment cross section is known to be very large at the maximum [Crance 1985], and it varies as $\Delta E^{3/2}$ [Lykke 1991] at threshold (6069 cm^{-1}). By connecting these two pieces of information, one can get an approximate pessimistic normalization of the cross section at threshold (figure 43): $\sigma \approx 3.8 \times 10^{-16} \Delta E(\mathrm{eV})^{3/2}$cm^2.

For $\Delta E = 1$ µeV, $\sigma \approx 3.8 \times 10^{-25}$ cm^2. With a 1 W cw laser beam focused on a surface S $= (10\,\mu\mathrm{m})^2$ covering the $\overline{\mathrm{H}}^+$ trapping volume, the detachment rate per ion will be more than 30 kHz per ion: $rate = (N\overline{\mathrm{H}}^+ \times \sigma \times P_{laser})/(S \times E_\gamma)$. With a laser shot duration of 150 µs, 99 % of the ions formed will be detached. The start time is given both by the
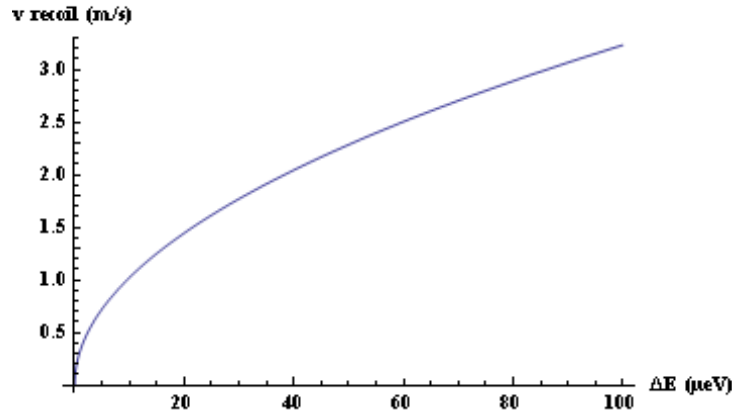
Figure 42: Atom recoil speed versus excess photon energy.

laser shot time and by the detection of the annihilation of the emitted positron.
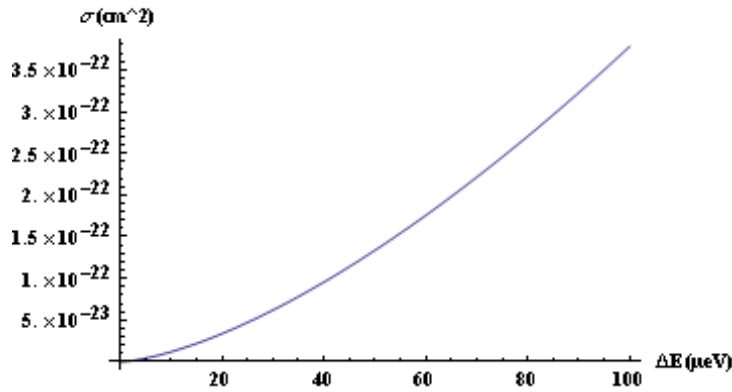
Figure 43: Photodetachment cross section versus energy above threshold.

12.3   Description of the laser system

The 1.64 µm laser radiation will be produced by an optical parametric oscillator (OPO) pumped by a fiber laser at 1064 nm. A non-linear crystal in the OPO converts one photon at 1.064 µm in two photons at the wavelengths of 1.64 µm (called the signal) and 3.03 µm (the idler). This laser source is commercially available (Argos model 2400 from Aculight). The non-linear crystal is a MgO:PPLN (Periodically-Poled Lithium Niobate) placed in a ring cavity which is resonant with the signal at 1.64 µm. The signal frequency is controlled thanks to an etalon placed inside the cavity and to a piezoelectric translator to scan the cavity length. For a pump power of 15 W the CW output power is 2 W for the signal and the idler. The modulation of the intensity of the 1.64 µm radiation will be made with an acousto-optic modulator.

13 Measurement of the free fall of the $\overline{\text{H}}$ atom

In this section we discuss the measurement of the free fall of the $\overline{\text{H}}$ after the photo detachment of the excess positron, following [Walz 2004]. As we will see, the cooling temperature and the energy of the photodetached positron are critical parameters, because there is a strong correlation between the measured $\bar{\text{g}}$ and the initial velocity of the atom. As a consequence, the height of the free fall is also a key parameter to be optimized for the experimental setup and the control of uncertainties.

13.1 Measurement uncertainties

In the first stage of the free fall experiments, $\bar{\text{g}}$ will be measured by determining the time interval between the photodetachment of the excess positron of the $\overline{\text{H}}^+$ ion and the arrival time of the $\overline{\text{H}}$ atom on an annihilation plane, by using the classical relationship:

$$z = \frac{1}{2}\bar{\text{g}}t^2 + v_{z0}t + z_0 \tag{27}$$

where z is the vertical position of the annihilation plane, v_{z0} and z_0 are the vertical velocity and the initial vertical position of the atom after the photodetachment, $t = t_1 - t_0$, t_0 being the photodetachment time, and t_1 the annihilation time. In this equation, only t_0 and t_1 are measured for each event. The horizontal trajectory will be discussed in section 13.4 where the detector design is discussed. It has no direct effect on the measurement of $\bar{\text{g}}$.

We fix the origin of the vertical coordinate to be the mean position of the atoms at t_0: $< z_0 >= 0$. As described in section 12, the photodetachment proceeds with a horizontal laser shot, so that we can also assume that the mean value of the initial velocity is $< v_{z0} >= 0$. Since z_0 and v_{z0} are not measured event by event, the measured value of $\bar{\text{g}}$ is: $\bar{\text{g}}_m = 2z/t^2$.

13.2 Rough evaluation of the statistics needed

We assume in a first step that the uncertainties on z_0 and v_{z0} obey $\Delta z_0, \Delta v_{z0} t \ll z$. Then, for each measurement, we have:

$$\frac{\Delta \bar{\text{g}}}{\bar{\text{g}}} \simeq \sqrt{\left(\frac{\Delta z}{z}\right)^2 + \left(\frac{2\Delta t}{t}\right)^2} \tag{28}$$

with, to first order:

$$\begin{cases} \Delta t &= \sqrt{(\Delta t_0)^2 + (\Delta t_1)^2} \\ \Delta z &= \sqrt{(\Delta l)^2 + (\Delta z_0)^2 + (\Delta v_{z0}t)^2} \end{cases} \tag{29}$$

where we have introduced Δl, the uncertainty on the position of the annihilation plane. In the Paul Trap, the $\overline{\text{H}}^+$ ions are very well localized, to a few µm. The position of the annihilation plane can be measured and stabilized to better than $100\,\text{µm}$, so that Δl and Δz_0 are negligible for a measurement of $\bar{\text{g}}$ at the percent level ($|z|$ is taken to be 15 cm, see below). The term Δv_{z0} has two sources: the initial velocity (expressed with the equivalent

temperature T) of the atom (see section 11), and the recoil of the photodetached positron. For an isotropic emission, we would have:

$$\Delta v_{z0} = \sqrt{\frac{kT}{m_H} + \frac{2m_e\Delta E}{3m_H^2}} \tag{30}$$

where k is the Boltzmann constant, m_H the mass of the antihydrogen atom, m_e the mass of the positron, and ΔE the energy of the emitted positron. However, with a horizontally polarized laser beam, the positron is preferentially emitted in the horizontal plane [Hall 1968] and we get:

$$\Delta v_{z0} = \sqrt{\frac{kT}{m_H} + \frac{2m_e\Delta E}{5m_H^2}}. \tag{31}$$

With N measurements, one gets an uncertainty on $\bar{g}$ of about:

$$\frac{\Delta\bar{g}}{\bar{g}} \simeq \frac{1}{\sqrt{N}}\sqrt{\left(\frac{kT}{m_H}\right)\left(\frac{t}{z}\right)^2 + \left(\frac{2m_e\Delta E}{5m_H^2}\right)\left(\frac{t}{z}\right)^2 + \left(\frac{2\Delta t}{t}\right)^2} \tag{32}$$

To equalize the first two terms in the right hand side, with an assumed $10\,\mu$K temperature, ΔE should be adjusted to better than $2\,\mu$eV. Taking $\Delta E = 1\,\mu$eV, the first term contributes to an uncertainty of 33 % and the second to 16 %. As was shown in section 12, the start time of the free fall can be known with a precision better than $150\,\mu$s. The time of the annihilation of the $\overline{\text{H}}$ atom can easily be measured to a better precision, so that the last term is negligible. Given these values, one gets an uncertainty of 37 % for one event, so one needs about 1500 fully detected annihilations to reach a 1 % precision on $\bar{g}$.

13.3 Simulation

This rough analysis has to be refined with a simulation, because the typical vertical initial velocity at $10\,\mu$K temperature is 0.3 m/s, and $< v_{z0} > t \sim 5$ cm, which cannot be neglected in comparison with $|z| = 15$ cm. The situation would be worse with a smaller value of $|z|$. This value is chosen low to limit the size and cost of the detector. One can see typical trajectories of atoms after photodetachment in Fig. 44.

Fig. 45 shows the arrival position in the annihilation plane. Fig. 46 shows the reconstructed time t and $\bar{g}$. The origin of the coordinate system is the mean initial position of the $\overline{\text{H}}$ atoms. The vertical coordinate is positive upwards.

Although the statistical uncertainty on the mean value of $\bar{g}$ is consistent with the 1 % estimate, the correlation between t and $< v_{z0} >$ induces a strong bias on the measured $\bar{g}$. However, this bias can be corrected for:

- The sensitivity to the value of $\bar{g}$ remains at the percent level. In Fig. 47 a) and b), one sees the reconstructed acceleration with a true value fixed at -9.71 m/s^2 and -9.91 m/s^2 in the simulation. The mean value shifts with roughly the same amplitude.
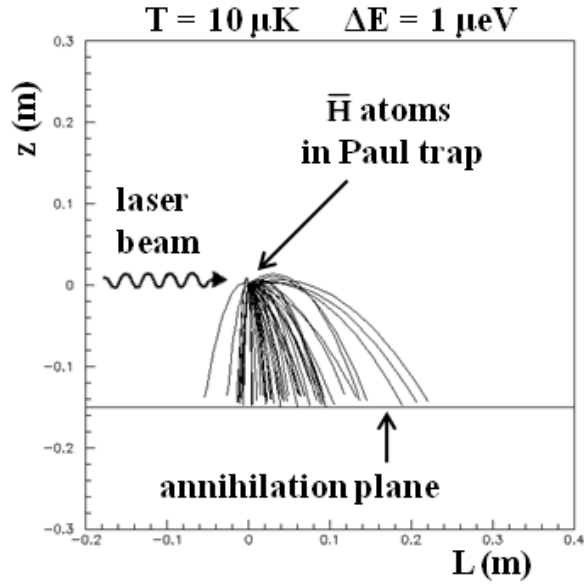
Figure 44: Typical trajectories of atoms after photodetachment (projection on the vertical plane containing the photodetachment laser beam). L is the coordinate in the horizontal plane in the direction of the photodetachment laser beam.
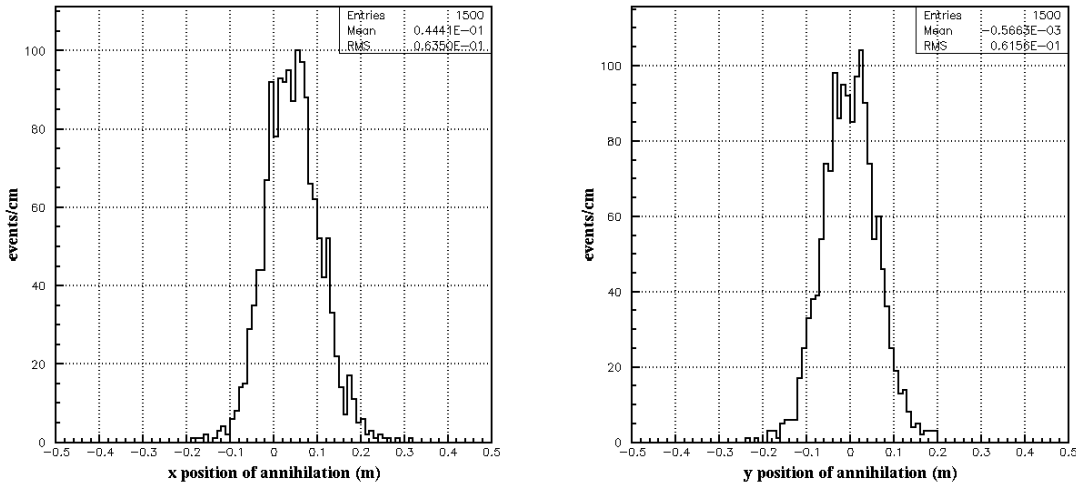
Figure 45: Arrival position in the annihilation plane: x is the direction of the laser beam. The shift due to the recoil from the photon absorption is clearly seen.

- The bias dependence upon the initial temperature is not too large (see Fig. 47 c) and d)). The bias dependance on T is about 0.05 ms^{-2} per µK. If one knows the initial temperature to better than 1 µK, the induced additional uncertainty on $\bar{g}$ is about 0.5 %. As was shown in section 11, the velocity distributions in x, y and z directions are determined by the confining potential well geometry in the Paul trap in the final stage of the cooling, and so the equivalent temperature can be

68
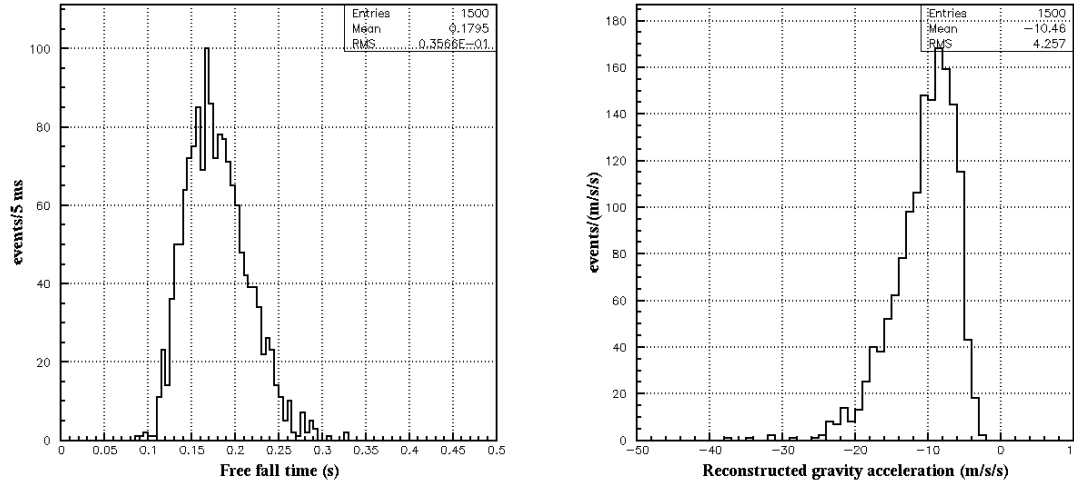
Figure 46: Measurement of the free fall time and acceleration.

determined to a few %. These numbers show that a 15 cm free fall is close to a minimal choice.

- With a movable annihilation plane, a set of measurements at different heights will show a smaller bias (see Fig. 48) and will allow to disentangle systematic effects.

13.4 Detection

13.4.1 Detector requirements

A free fall "event" is characterized by:

- The photodetachment laser shot which gives the start time of the free fall.

- The emission of the positron from the $\overline{\text{H}}^+$ ion and its subsequent annihilation. Because of the high RF fields in the Paul trap, the positron is ejected with a very high velocity in an unknown direction. The detection of one of the two 511 keV gammas from its annihilation could also be used to define the start of the event with a better precision than the laser illumination duration.

- The annihilation of the positron and of the antiproton of the $\overline{\text{H}}$ atom at the end of the free fall. Two 511 keV gammas are emitted, and in 95 % of the cases the proton-antiproton annihilation produces a set of charged and neutral pions, with 99 % of the latter decaying into two high energy gamma rays.

To characterize an event and perform the $\bar{\text{g}}$ measurement, it is sufficient to measure the following quantities:

- The laser shot time.
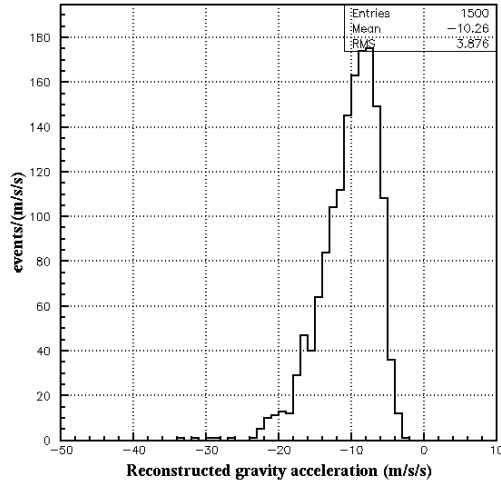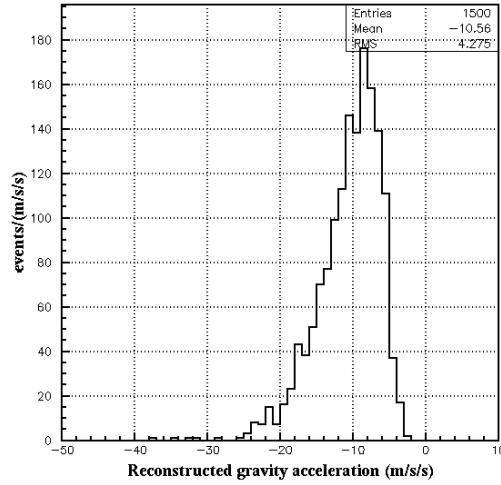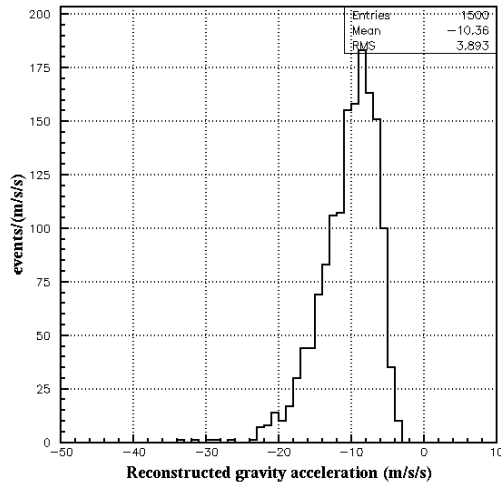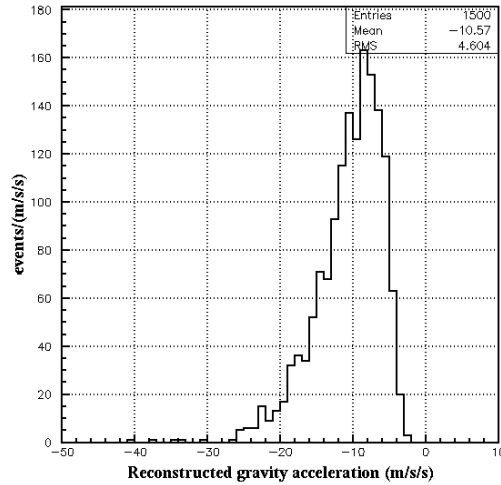
Figure 47: a) True $\bar{g}$ = -9.71 m/s^2 ; T = 10 µK. b) True $\bar{g}$ = -9.91 m/s^2 ; T = 10 µK. c) True $\bar{g}$ = -9.81 m/s^2 ; T = 8 µK. d) True $\bar{g}$ = -9.81 m/s^2 ; T = 12 µK.

- The trajectories of the charged particles. Small Time Projection Chambers (TPC's) can be placed around the vacuum vessel to minimize the number of necessary channels, to eliminate cosmic background.

- The annihilation time. Plastic scintillator counters around the TPC's are well suited to detect the emitted charged pions and provide the annihilation time with high precision.

The basic requirements for those detector elements are listed in the following paragraphs. A detailed simulation will be needed to precisely fix their characteristics.

Before discussing the various detectors, a word has to be said on the cosmic background. In order to eliminate this background, the free fall events need to be clearly
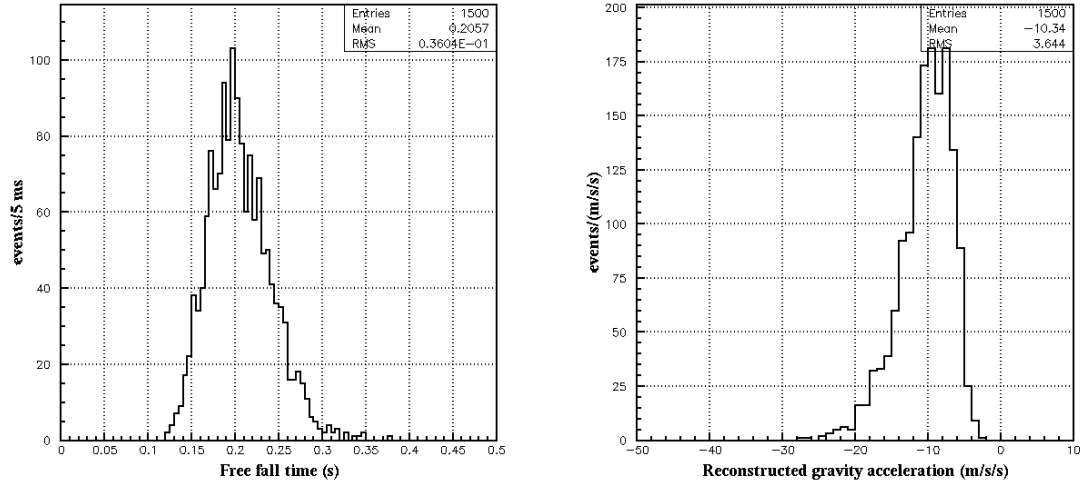
Figure 48: Measured free fall time and acceleration for a height of 20 cm.

identified. A sufficient signature is the detection of at least two non-back-to-back charged particles, essentially pions, with trajectories crossing at the annihilation plate with a few mm precision. The detection of one of the emitted gammas in coincidence with the start time of the free fall would be an additional clear signature, but cannot be done with high efficiency without a dedicated detector (like a crystal calorimeter).

Assuming a 0.2 m² annihilation plate area, the number of cosmic ray events in this time window is below 10 before any geometrical and energy cut. The width of the time distribution of true events is about 40 ms, so the background will be negligible after simple reconstruction cuts, and it can be measured easily.

Note that particles accompanying the $\overline{\mathrm{H}}^+$ ions ($\overline{\mathrm{H}}$, e⁺, Ps, γ) do not produce background to the free fall events, since the photodetachment happens after the cooling of the $\overline{\mathrm{H}}^+$ ions, which takes more than a ms.

13.4.2 Experimental setup

A sketch of the experimental setup is shown in Fig. 49.

The various elements characteristics are indicative. They will be determined more precisely at the technical design stage, and are given to get a realistic costing and implementation of the experiment.

- The vacuum chamber.

  To avoid spurious annihilations with the residual gas in the chamber, the capture/cooling of the $\overline{\mathrm{H}}^+$ ions and the free fall experiment must be performed in ultra-high vacuum. That is another reason to limit the size of the chamber in addition to cost considerations. To allow for free fall heights of 15 and 20 cm, and for the insertion of the Paul trap, the cylindrical chamber height can be taken to be 35 cm. Its diameter, 40 cm, is chosen large enough to fit a 35 cm diameter annihilation plate in order to accept atoms with large initial horizontal velocities (see Fig. 45).
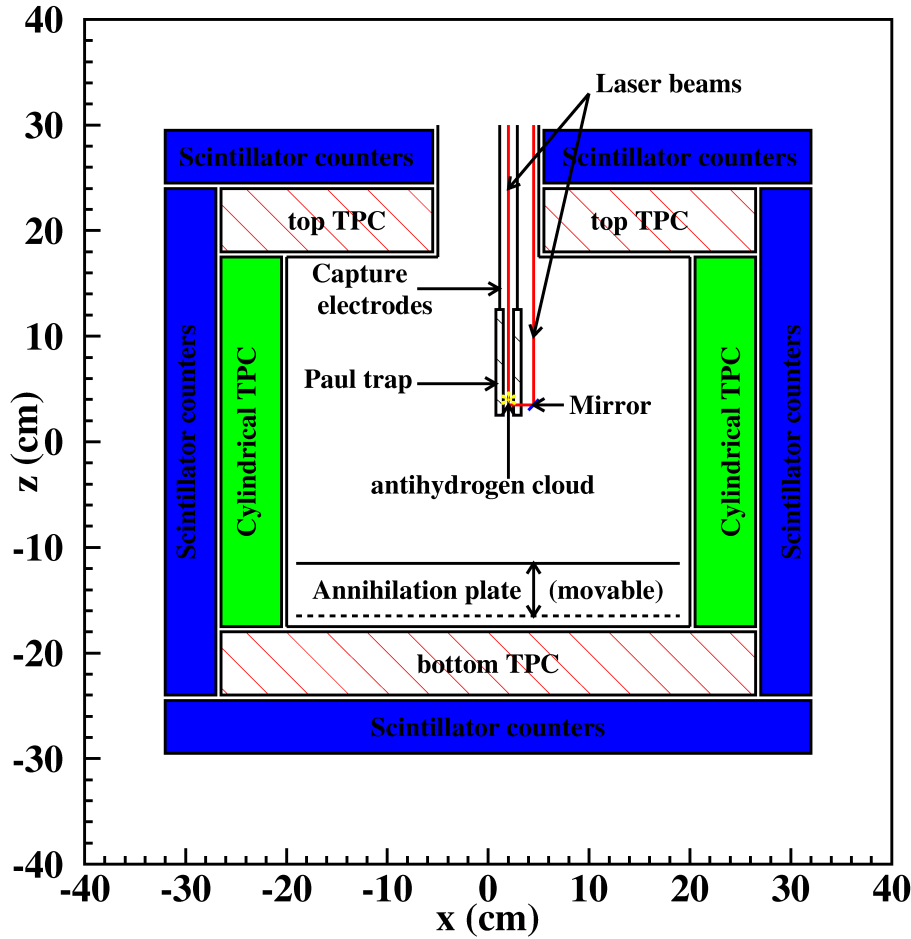
Figure 49: A sketch of the experimental setup. A description of the elements is in the text.

- The Paul trap.

  In order to minimize the vertical velocity, the Paul trap axis is vertical and the electrode length is about 10 cm (see section 11). The Paul trap is segmented, and after cooling, ions are centered on the axis about 1 cm above the bottom end of the trap. The support structures for the Paul trap, the Be ovens and the ionizing e⁻ guns can be made very thin and are not drawn. The vertical axis of the Paul trap is displaced by 2 cm with respect to the annihilation plate center to partly compensate for the mean shift due to the recoil of the anti-atom after the absorption of the photodetachment photon.

  In order to signal the presence of the ion pair (Be^+ - $\overline{H}^+$) in the Paul trap before the photodetachment laser shot, the fluorescence emitted by the ions during cooling will be detected with imaging optics and registered by a CCD camera. The setup can be adapted from what has been realized in [Dubessy 2010]. This instrumentation is not in vacuum, and a reentrant window is needed, at about 7 cm distance from the

Paul trap and of 10 cm diameter. It is perpendicular to the plane of Fig. 49.

- The entrance tube.

To allow for the injection of the $\overline{\mathrm{H}}^+$ ions and of the 4 laser beams (one for photodetachment, one for Beryllium cooling, two for side band Raman cooling), also for pumping purposes, a 10 cm diameter entrance tube is needed at the top of the chamber. One of the mirrors to deflect the laser beams is shown in the sketch of the experimental setup. Two other ones (not shown) in a different plane are needed to accommodate the contra-propagating laser beams for the sideband Raman cooling. The $\overline{\mathrm{H}}^+$ beam (not shown) enters with a small angle with respect to the vertical axis to allow the insertion of a mirror for the vertical laser beam for the Beryllium cooling. Another mirror (not shown) is needed for cooling. The drift tube for $\overline{\mathrm{H}}^+$ ions is drawn.

- The annihilation plate.

The annihilation plate should be movable to allow for measurements at different heights.

- The Time Projection Chambers.

Small Time Projection Chambers cover as much as possible of the solid angle to detect and reconstruct the trajectories of at least two of the charged pions with very high efficiency. A possible schematic arrangement of the top chambers is shown on Fig. 50 with the cylindrical chamber. The bottom TPC (not shown) can cover the whole surface.

Each TPC is 6 cm wide with three rows of $1 \times 1\,\mathrm{cm}^2$ pads spaced by 2 mm. The rows are 0.75 cm from each other to measure three points per track. For few 100 MeV/c pions, multiple scattering in the vacuum chamber walls is significant (position deviations of $\sim 50\,\mu\mathrm{m}$ and angular deviation of ~ 40 mrad at 300 MeV/c), so that it is enough to aim at a few $100\,\mu\mathrm{m}$ space resolution per point. In addition, the precision needed at the annihilation plate is only a few mm, so that such a resolution is adequate. Since typical drift velocities of electrons in a TPC are 1-15 $\mathrm{cm}\mu\mathrm{s}^{-1}$ depending on the gas mixture and on the applied voltages, the start time should be known with a precision of ~ 5 ns to reach the desired spatial resolution.

- The plastic scintillator counters.

Thick (a few cm) plastic scintillator counters cover the detector chamber. They are used to detect charged tracks and some of the gamma rays from positron and antiproton annihilations (both at the start and at the end of the free fall), and to measure the time of the annihilation with the needed precision of a few ns. The form and the geometrical shapes of the counters have to be optimized to cover most of the solid angle to maximize the acceptance.

Note: In the great event that anti-atoms move upwards rather than downwards, the TPC's would allow the detection of the annihilations at the top of the chamber!
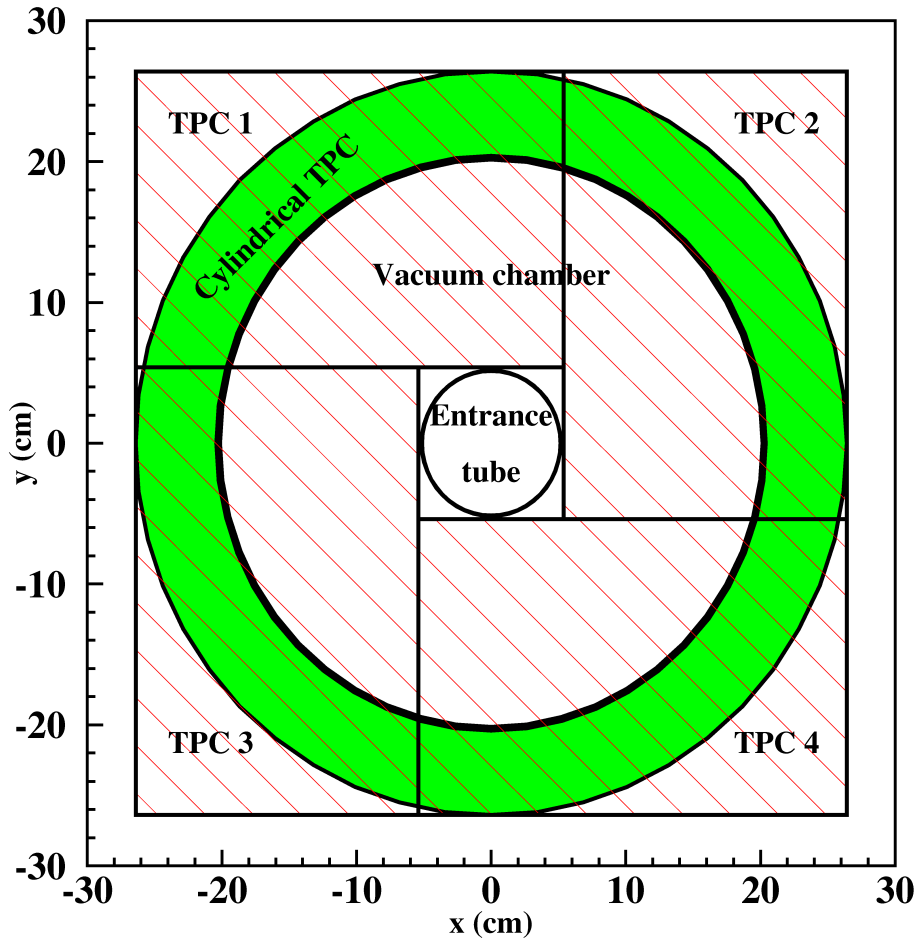
Figure 50: Possible arrangement of TPC's around the chamber. Four identical chambers (hatched rectangles) surround the entrance tube. The cylindrical TPC below is shown in green.

13.4.3 Detection acceptance and efficiency

A major limitation factor for the detection efficiency would seem to be the geometry of the Paul trap (see Fig. 41, page 61, in section 11). Indeed, if $\overline{H}$ atoms hitting one of the electrodes during their fall would annihilate, only 37 % of all $\overline{H}$ atoms would survive. This is not the case, because the atoms are very slow, and a large fraction of them (about 75 %) will be reflected rather than annihilated by the electrodes (see section 13.4.4 below). So the loss for the detection amounts only to 0.75 * (1 - 0.37) = 16 %. In order not to get a bias on the $\bar{g}$ measurement from these reflections, the electrodes must be polished and be precisely vertical. In that case, reflections are specular and the vertical speed is not affected.

As can be seen from table 6, in 93.3 % of the cases, the $\overline{H}$ annihilation directly produces at least 2 non-back-to-back charged pions (back-to-back tracks have to be removed for the cosmic background suppression). Taking a 98 % efficiency to detect a track in a TPC (i.e. 3 points measured), and taking into account the dead solid angle at the top of the

74

vacuum chamber, about 90 % of the annihilations can be reconstructed.

Annihilation channel	Fraction (%)
$\pi^+\pi^-$	0.4
$\pi^+\pi^-$ n π^0 (n $\geq$ 1)	48.3
$2\pi^+2\pi^-$ n π^0 (n $\geq$ 0)	40.0
$3\pi^+3\pi^-$ n π^0 (n $\geq$ 0)	5.0

Table 6: $\bar{\text{p}}$ p annihilation modes with at least 2 charged pions.

The measurement of the time with the plastic scintillator counters can be done with more than 99 % efficiency.

The overall detection efficiency can thus be estimated to: $\epsilon = (1 - 0.16) * 0.90 * 0.99 = 75\%$. A 65 % value is assumed to take into account uncertainties in this estimation, losses due the instrumentation, the supports and the reentrant window which are not included in the present simulation.

13.4.4 Quantum effects

The behavior of a single atom approaching a surface cannot be treated classically. Quantum effects are not negligible: a significant fraction of slow $\overline{\text{H}}$ atoms can be reflected from the surface rather than annihilated. This effect can be avoided to a large extent, or even be used to get a higher precision on $\bar{\text{g}}$. This is discussed in detail in section 14. Since these effects depend upon the nature of the surface, the material for the annihilation plate has to be properly chosen.

Quantum effects also have an important consequence on acceptance: a large fraction of the anti-atoms hitting an electrode of the Paul trap will be reflected because they are still very slow. One can see in Fig. 52, page 79, that for an incident $\overline{\text{H}}$ atom of ~ 0.3 ms^{-1} velocity, i.e. $0.045 \, \text{m}^2\text{s}^{-2}$ kinetic energy per unit mass, the reflection probability is close to 70 %, depending on the material.

13.4.5 Additional constraints

Although the $\overline{\text{H}}$ atom is neutral, and since the gravitational force is so weak, one must check whether its polarizability and its magnetic moment are small enough to allow the free fall measurement. One assumes here the same electromagnetic properties of the anti-atom as those of the atom.

a) Constraint on the electric field:

The hydrogen atom polarizability is $\alpha = 8.4 \times 10^{-30} \, \text{m}^3$. In the presence of an electric field $\vec{E}$, it feels a force (with ϵ_0 the permittivity of vacuum):

$$\vec{F} = (\vec{p}.\overrightarrow{\nabla})\vec{E} = \alpha\epsilon_0(\vec{E}.\overrightarrow{\nabla})\vec{E}. \tag{33}$$

In order to be entitled to neglect it, one needs $\|\vec{F}\| < 10^{-3}\|m\vec{g}\|$, this leads to the condition:

$$\|(\vec{E}.\overrightarrow{\nabla})\vec{E}\| < 2 \times 10^{11} \, \text{V}^2\text{m}^{-3}. \tag{34}$$

Within the Paul trap (see section 11 for the definiton of V_0 and R_0), one has (x and y are the coordinates in the horizontal plane, and $\vec{R}$ is the vector of components $(x, y, 0)$):

$$V \simeq V_0 \frac{x^2 - y^2}{2R_0^2}, \tag{35}$$

$$(\vec{E}.\vec{\nabla})\vec{E} \simeq -\frac{V_0^2}{R_0^4}\vec{R}, \tag{36}$$

$$\|(\vec{E}.\vec{\nabla})\vec{E}\| \sim \frac{V_0^2}{R_0^3}. \tag{37}$$

At the capture time, $V_0 \simeq 500\ V$, but at the end of the cooling and before the photodetachment, the potential well is adiabatically decreased to about 25 V. This leads to (with $R_0 = 5\,\mathrm{mm}$):

$$\|(\vec{E}.\vec{\nabla})\vec{E}\| \sim 5 \times 10^9\ \mathrm{V^2 m^{-3}}. \tag{38}$$

Moreover, the force is mainly in the horizontal plane, so the condition (34) is largely satisfied.

b) Constraint on the magnetic field:

The potential energy of an atom H in an external magnetic field is the sum of the electron and proton contributions: $V = -(\vec{M}_e + \vec{M}_p).\vec{B}$ where $\vec{M}_e$ and $\vec{M}_p$ are the magnetic moments of the electron and of the proton. The latter can be neglected, so that the resulting force is: $\|\vec{F}\| = \|-\vec{\nabla}V\| \simeq \mu_B \| - \vec{\nabla}B\|$, where μ_B is the Bohr magneton. The condition $\|\vec{F}\| < 10^{-3}\|m\vec{g}\|$ reads:

$$\|\vec{\nabla}B\| \ll 2 \times 10^{-6}\ \mathrm{Tm^{-1}}. \tag{39}$$

Although not very stringent, this condition will impose some care in the design of the experimental environment.

14 Perspective: Quantum effects in free fall experiments

In this section, we discuss quantum features related to the uncertainty analysis in measuring gravitational properties of atoms as well as to possible longer term improvements in the accuracy profiting from quantum effects. We start with the analysis of the classical free fall measurement discussed in Section 13 and investigate the limitations caused by the quantum uncertainty in the initial vertical velocity. We then account for a second major quantum effect that is the quantum reflection of $\overline{\mathrm{H}}$ atoms from the detection surface due to the Casimir-Polder/van der Waals (CP/vdW) atom-surface potential [Casimir 1948, Friedrich 2002, Voronin 2005-1, Voronin 2005-2]. We also show how these limitations can be overcome. We then present ideas, analogous to those developed for measuring gravitational quantum states of ultracold neutrons (UCN) [Nesvizhevsky 2002, Nesvizhevsky 2003, Nesvizhevsky 2005], which could be used in the future to improve the accuracy of the measurement, by turning the quantum motion of atoms from a drawback to an advantage [Voronin 2011].

14.1 Quantum limitations in the classical experiment

When an antihydrogen atom is produced by photodetachment (Section 12), it leaves the ion trap (Section 11) with a vertical velocity which has a null average and a dispersion Δv_{z0}. The horizontal velocity does not affect directly the precision of the measurement, but the dispersion of the vertical velocity component has a major impact on this precision.

For this discussion, let us assume that $\overline{\mathrm{H}}$ atoms in the trap have been cooled down to the quantum limit of the ground state (zero or nearly zero temperature), and that the photodetachment process does not degrade the velocity dispersion thus attained. It follows that the initial distribution is the Gaussian wave packet which corresponds to the ground state of the harmonic ion trap. The product of the initial velocity dispersion Δv_{z0} (along the vertical direction) and the initial altitude dispersion Δz_0 is thus given by the minimum in the Heisenberg relation

$$m\Delta v_{z0}\Delta z_0 = \hbar/2. \tag{40}$$

With the numbers discussed in Section 11, in particular with an oscillation frequency $\omega/2\pi \simeq 500$ kHz in the harmonic ion trap, the typical dispersions are $\Delta v_0 \simeq 0.3$ ms^{-1} and $\Delta z_0 \simeq 0.1\,\mu$m.

The measurement of the gravity acceleration $\bar{\mathrm{g}}$ has then to be extracted from the classical free fall time t, which corresponds to the solution of the equation (40) $z = z_0 + v_{z0}t + \bar{\mathrm{g}}t^2/2$ where z is the vertical coordinate of the annihilation plate, z_0 and v_{z0} the initial vertical position and vertical velocity (with mean values equal to 0 and the dispersions Δz_0 and Δv_{z0} discussed in section 13). The accuracy in the extraction of the value of $\bar{\mathrm{g}}$ thus depends on the initial dispersions as well as on the counting statistics. In particular, the dispersion of the initial velocity has a major impact on the accuracy of this estimation.

In order to minimize this impact, a natural solution is to increase the height $|z|$ of free fall. This strategy is however limited by the associated increase in the size of the experimental installation and therefore in the cost of the experiment. A natural number

for characterizing this optimization of the design of the experiment is the ratio $\Delta v_{z0}^2 / 2g|z|$ of initial kinetic energy to the initial potential energy of the atoms (for $|z| = 15$ cm and $\Delta v_{z0} = 0.3$ ms^{-1}, this ratio is 0.03. This ratio will also play a key role in the discussion of the effect of quantum reflection. This effect and the associated systematics will be discussed in the next subsection. Note that the relative dispersion of the initial potential energy $g\Delta z_0/g|z|$ has a much smaller value with the typical numbers given above.

At this point, we have to consider possible solutions to reduce the velocity dispersion and thus improve the accuracy of the estimation of $\bar{g}$. One solution could be to produce angularly collimated atoms by using a spatially-shaped trap analogous to that developed for manipulating UCNs in the GRANIT experiment [Barnard 2008, Baessler 2009].

14.2   Quantum reflection of atoms from the Casimir potential

Quantum reflection is a generic phenomenon for matter waves in a rapidly varying potential. It has been observed in particular for atoms experiencing an attractive Casimir potential in the vicinity of a solid surface [Shimizu 2001, Pasquini 2004]. A fraction of the cold $\overline{\mathrm{H}}$ atoms falling onto the detection plate should be reflected before touching it [Voronin 2005-1, Voronin 2005-2]. This clearly affects the free fall measurement and solutions have to be designed for this potential problem.

Accurate evaluation of the Casimir potential is a crucial ingredient in the calculation of quantum reflection. Here, we use general expressions which have been developed for atoms above surfaces, and are written in terms of the atomic polarizabilities and of the reflection amplitudes associated with the material surface [Messina 2009, Canaguier 2011]. In Fig. 51 we plot the results of these calculations performed for $\overline{\mathrm{H}}$ atoms and three model surfaces having different reflection properties for electromagnetic fields: perfect mirror (black curve), silicon plate (blue) and silica plate (red) [Gérardin 2011]. For the sake of readability, the rapidly varying potentials have been divided by an asymptotic factor C_4/d^4 (d is the distance from the surface) obtained at long distances for the perfect mirror. The coefficient C_4 has a value of 73.60 atomic units for $\overline{\mathrm{H}}$ atoms (calculated with the same polarizability as for H atoms). The three curves have the same asymptotic forms C_4/d^4 at long distances and C_3/d^3 at short distances, with a crossover at a distance of the order of 40 nm. The values of the coefficients are smaller and smaller when going from a perfect mirror to the poorer electromagnetic reflectors silicon and then silica. The dashed lines in Fig. 51 represent the rational approximations often used for describing the variation of the potential. Note that they appear as not so good approximations of the exact variation laws plotted as solid lines.

Then the Schrödinger equation has to be solved by numerical methods. The quantum reflection is deduced by taking into account the annihilation of $\overline{\mathrm{H}}$ atoms when they touch the material surface, using a method similar to that in [Voronin 2005-1, Voronin 2005-2]. The results are shown in Fig. 52 for the reflection of atoms on the same model mirrors used for Fig. 51 (and with the same color codes). For these calculations, the initial dispersions of the atomic motion are disregarded and the reflection probability is drawn as a function of the parameter $g|z|$ ($|z|$ the free fall height) which thus measures the kinetic energy per unit mass of atoms incident on the detection plate. Several striking features appear in Fig. 52. Firstly, significant values are obtained for the quantum reflection probability R, which reaches for example ~ 32 % on silica, ~ 20 % on silicon, ~ 14 % on a perfect mirror for $|z| = 0.1$ m (R is smaller if $|z|$ is larger). Secondly, this probability has a larger value
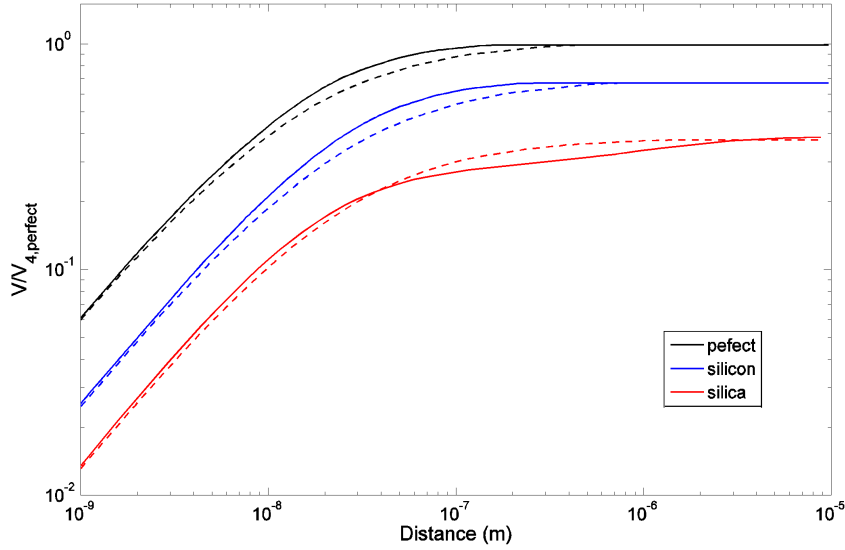
Figure 51: Casimir potential divided by the asymptotic form obtained at long distances for the perfect mirror ($V/V_{4,\mathrm{perfect}}$) for $\overline{\mathrm{H}}$ atoms above perfect, silicon or silica mirrors
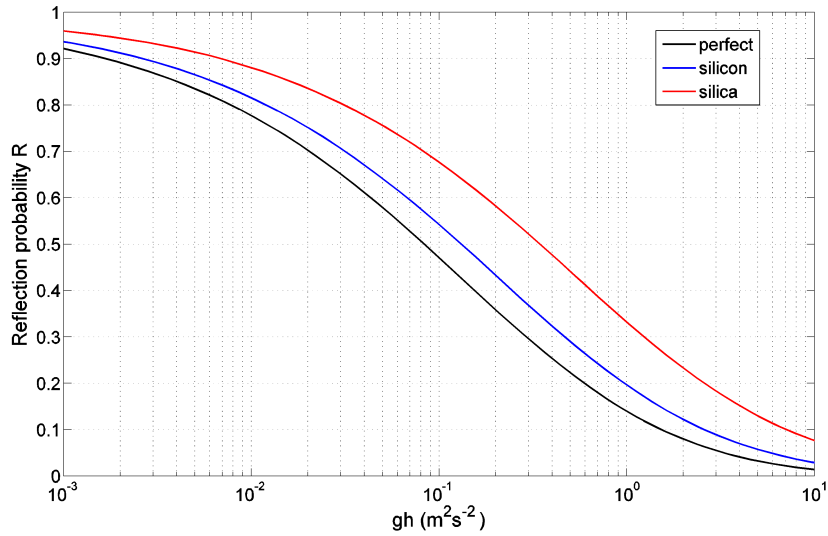
Figure 52: The quantum reflection probability R for antihydrogen atoms above perfect, silicon or silica mirrors as a function of the kinetic energy per unit mass of incident atoms.

when evaluated for a weaker Casimir potential (that is also for a weaker reflection for electromagnetic waves). This counter-intuitive feature may be understood by analyzing the non-adiabatic coupling which leads to quantum reflection; for a weaker potential, this coupling becomes efficient at closer and closer distances from the surface, and the Casimir potential is steeper and steeper when the atom approaches the surface [Gérardin 2011].

We now discuss the consequences for the free fall experiment described in the preceding section, as well as the solutions for the potential problems:

1. First, a fraction R of the freely falling atoms is reflected back from the detection plate, and bounces back to their initial position before returning again to the plate. This reflection diminishes the number of atoms by a factor $T = 1 - R$ and then the relative uncertainty on $\bar{g}$ by a factor $1/\sqrt{1-R}$ (the uncertainty is dominated by statistics).

2. With the mean time of free fall denoted $<t> = \sqrt{2|z|/\bar{g}}$, the next times of arrival onto the plates will be $3<t>$, $5<t>$ and so on. If not taken into account, these bouncing atoms would seriously bias the estimation of $\bar{g}$, but it is easy to discard them from the detection procedure.

3. A more subtle effect would affect the measurement if it were not accounted for. The dependence of the reflection probability versus the energy of atoms favors the higher energy atoms in the distribution of detected atoms. In order to correct for this bias, a model will be developed and the distribution of detected atoms corrected in the estimation of $\bar{g}$.

Using this model, it will be possible to free the measurement of potential spurious effects due to quantum reflection, at least when the atomic motion is described classically. However, this classical description is still an approximation. A model will also be developed to take into account the fact that the initial state of the freely falling atoms is a coherent wave packet, rather than a classical distribution of incoherent motions. Depending on the output of the model, either the validity of the semi classical statistical description will be assessed, or a full quantum treatment of motion will be developed to correct the estimation of $\bar{g}$ of any potential inaccuracy.

14.3 Spectroscopy of the gravitational quantum levels of the $\overline{\text{H}}$ atom - a long term prospect

The disturbing quantum effects appearing in the classical free fall measurements discussed above could be converted into an advantage if a proper quantum-mechanical experiment were designed. To this purpose, we have to trap $\overline{\text{H}}$ atoms in gravitational quantum states above a horizontal mirror [Nesvizhevsky 2002, Nesvizhevsky 2003, Nesvizhevsky 2005, Voronin 2011], thanks to the combined effect of the gravitational field of the Earth and quantum reflection. $\overline{\text{H}}$ atoms would thus be settled in quasi-stationary gravitational states "bouncing" on the material surface for a long storage time which has been evaluated to be $\tau = 0.1s$ for a perfect mirror [Voronin 2011], and may be even longer for a silicon or silica surface [Gérardin 2011]. An important parameter governing the lifetime of gravitational states is the ratio of the spatial scales, characteristic for the gravitational and Casimir interaction potentials, $l_{grav} = \sqrt[3]{\hbar^2/2m^2g} = 5.87\,\mu\text{m}$ and $l_{CP} = \sqrt{2mC_4} = 0.027\,\mu\text{m}$ respectively. The hierarchy of these scales $l_{CP} \ll l_{grav}$ allows us to treat $\overline{\text{H}}$ under the combined effect of gravitational and CP/vdW interaction potentials as a quantum bouncer [Nesvizhevsky 2002, Nesvizhevsky 2003, Nesvizhevsky 2005, Voronin 2011] with a modified boundary condition. The corresponding wave functions are given by the Airy function $\psi_n(d) \propto Ai\left(\frac{z}{l_{grav}} - \lambda_n\right)$, were d is the distance to the surface, and λ_n an eigenvalue, which determines the corresponding energy $E_n = mgl_{grav}\lambda_n$. The boundary condition consists of matching the Airy function with the wave function

of an atom undergoing a quantum reflection in the intermediate region $l_{CP} \ll d \ll l_{grav}$. The eigenvalues λ_n thus differ from those for a pure quantum bouncer by a complex shift which describes the antiatom-wall interaction. The shift and widths of *all* lowest quantum states are the *same*. It follows that the effect of the antiatom-wall interaction does not affect the frequencies of transition between different states in the first order of the (small) interaction parameter. For instance, the computed transition frequency between the first and the second state is $\omega_{12}/2\pi = 254.54$ Hz. The other frequencies can be deduced from the results given in table 7.

n	λ_n^0	E_n^0 (peV)	z_n^0(µm)
1	2.338	1.407	13.726
2	4.088	2.461	24.001
3	5.521	3.324	32.414
4	6.787	4.086	39.846
5	7.944	4.782	46.639
6	9.023	5.431	52.974
7	10.040	6.044	58.945

Table 7: The eigenvalues, energies and classical turning points for a pure quantum bouncer.
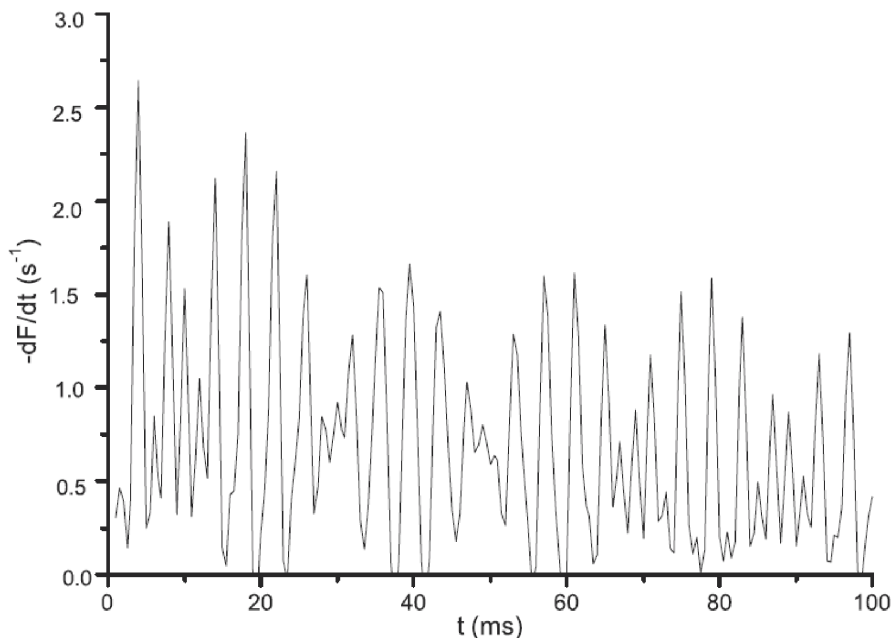
Figure 53: Evolution of the annihilation rate of $\overline{\mathrm{H}}$ atoms for a superposition of the 3 lowest gravitational states.

A quantum experiment consists of measuring either the frequency of transition between the lowest gravitational quantum states, and/or in measuring the spatial/velocity

distribution of the antiatom density in a position sensitive detector in analogy to the experiments with UCN [Voronin 2011, Baessler 2009, Nesvizhevsky 2010], either the annihilation rate of $\overline{\text{H}}$ atoms in the bulk mirror as a function of time as shown in Fig. 53 [Voronin 2011]. As all relevant parameters of the gravitational experiments with UCN are precisely, or approximately, equal to those with $\overline{\text{H}}$ atoms, we could directly apply all developments achieved so far with UCN to experiments with $\overline{\text{H}}$ atoms. Moreover, some features of $\overline{\text{H}}$ reflection from a surface favor $\overline{\text{H}}$; in particular, requirements to mirror parameters such as roughness are largely relaxed as $\overline{\text{H}}$ does not directly "touch" surface while reflecting from it. The characteristic size of a mirror for a quantum experiment is equal to $\Delta v_0 \tau \sim 3\,\text{cm}$, or a few times larger if longer storage times could be achieved [Gérardin 2011]. For a 10 cm mirror, the width of quantum states is about 16 times smaller than the distance ω_{12} between neighbor low quantum states, so that a typical accuracy would be a few times higher than this value.

A quantum experiment needs a compact experimental setup, which limits the cost to construct it. The accuracy of a quantum experiment is limited by statistics. In particular, an additional development is needed on loss-free delivery of a high phase-space density of $\overline{\text{H}}$ to the entrance of the gravitational quantum trap. This work will be coordinated with the developments on the $\overline{\text{H}}^+$ trap. Provided no significant dilution in the $\overline{\text{H}}$ phase-space density, a measurement of $\bar{\text{g}}$ with an accuracy better than 10^{-3} is feasible. No major systematic effects are expected.

15 Overall layout and space requirements

The GBAR experiment is foreseen as a user of the second antiproton beam of the new ELENA facility. A schematic drawing of its possible implantation in the AD hall is presented in Fig.54. The experimental setup comprises three main areas:

- The slow positron production unit;

- The positron and antiproton preparation area;

- The antihydrogen reaction chamber and gravity measurement chamber.
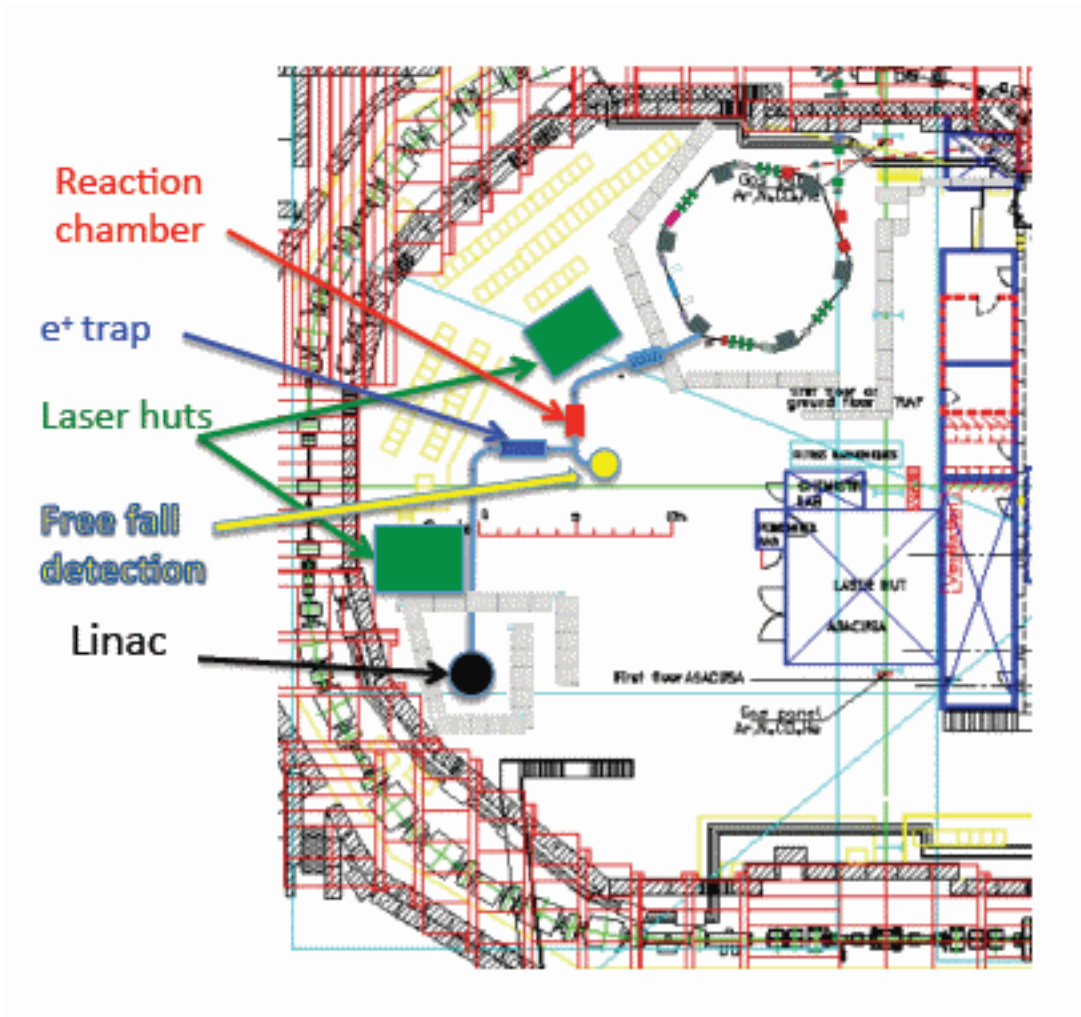
Figure 54: General layout of the GBAR experiment within the AD/ELENA hall. The experimental setup schema has been superimposed on part of a drawing extracted from [Eriksson 2010].

The slow positron production unit comprises the items detailed in sections 4, 5, 6. They are organized to minimize surface occupation. All the relevant equipment is surrounded by steel reinforced concrete (52 % steel) to provide protection against X rays. A dedicated ventilation device will be needed to evacuate the ozone produced by the linac

and remove it from the AD hall. A water cooling system has to be installed in the vicinity to cool down the linac, the magnets of the positron source and the cryocooler compressors used for the positron moderation and the positron trap.

The slow positrons are guided using a 0.01 T magnetic field to the positron storage trap. The guiding device uses magnetic elements already realized for the SOPHI setup in Saclay. The positron storage trap is the one made by the RIKEN Atomic Physics Laboratory. It is presently installed at Saclay in the framework of the CEA-CNRS-RIKEN development program [Pérez 2010] to optimize its trapping efficiency with the linac-based positron source.

The positron and antiproton preparation area consists of the existing RIKEN MRT trap and the antiproton extraction beam line from ELENA complemented with the 100 to 1 keV decelerator and buncher.

The two beams are guided towards a reaction chamber to form positronium, antihydrogen and $\overline{\mathrm{H}}^+$ ions. There is enough room to allow the use of the neutral beam of antihydrogen atoms for dedicated measurements.

The $\overline{\mathrm{H}}^+$ ions are extracted from the antiproton and antihydrogen beam and guided to the gravity measurement chamber using magnetic devices. The end part of the experiment comprising the reaction chamber and the gravity measurement chamber are placed in a clean temperature controlled room, not shown. Within this experimental room, there is a set of magnetic coils designed to compensate the Earth's magnetic field and the stray field from the other components of the experiment. Two laser huts contain the laser systems needed by the experiment. The complete setup occupies about 150 m^2. In addition, a control room has also to be installed outside the hall.

16 Organization, cost estimate, schedule and risk assessment

16.1 Physics tasks

16.1.1 Work packages

The physics tasks detailed in sections 4 to 14 are subdivided in work packages that are listed in Table 8 together with the corresponding main objects to be built.

	Work package	Content
1	Production of fast e^+	e^- Linac, e^+/e^- separator, target
2	Production of slow e^+	W and solid Ne moderator, transport beam line
3	e^+ accumulation	RIKEN trap, in/out bunchers
4	Ps formation and excitation	e^+/Ps converter, Ps excitation lasers
5	$\overline{p}$ deceleration - ELENA interface	Drift tube, fast HV switch, $\overline{p}$ buncher
6	Production of $\overline{H}$ and $\overline{H}^+$	Reaction chamber, in/out beam lines, $\overline{H}^+$ spectrometer
7	$\overline{H}^+$ cooling	Capture and Paul traps, Be^+ cooling, lasers
8	Free fall measurement detector	Chamber, TPCs, scintillators, electronics
9	Quantum states detection	Annihilation plate, feedback piezo...
10	Slow control and DAQ	Automated and centralized slow control, DAQ system
11	Miscellaneous items	Installation at CERN

Table 8: Work packages definitions.

16.1.2 Monitors and detectors

Each work package also comprises a set of detectors to monitor its performances or to measure physical quantities. A short description is given below.

1. Production of fast e^+: the electron current is monitored with a torus around the beam pipe of the linac, which is triggered with a clock unit whose signal is distributed to the rest of the apparatus for synchronization.

2. Production of slow e^+: the slow e^+ beam is monitored upstream of the accumulation trap. A thin target can be inserted on the beam trajectory. The slow positrons convert into two back-to-back 511 keV photons that are counted with a scintillator. Alternatively, an MCP equipped with a phosphor screen can be inserted in the beam line to image the beam spot and measure the charge integral and pulse width. The energy spectrum can also be monitored with a retarding grid set at a few volts above ground.

3. e^+ accumulation: the measurement of plasma modes can monitor the plasma parameters in a non-destructive way by adding a small voltage excitation on one electrode. Alternatively, the electron and positron plasmas can be monitored when

ejecting them onto a downstream MCP, also equipped with a phosphor screen for imaging.

4. Ps formation and excitation: the orthopositronium yield can be monitored using the SPPALS technique [Cassidy 2008], i.e. by measuring with a fast crystal the annihilation gamma ray time spectrum in order to extract the 142 ns lifetime component. The Ps density inside the converter tube may be deduced from the detection of fluorescence photons when the Ps cloud is illuminated by the excitation lasers.

5. $\overline{p}$ deceleration - ELENA interface: the beam emittance will be determined in the preparation phase. The antiprotons that do not interact and traverse the positronium target may be detected during data taking, providing a monitor of their flux.

6. Production of $\overline{H}$ and $\overline{H}^+$: the neutral $\overline{H}$ flux can be determined easily through interaction of this beam with scintillators. The $\overline{H}^+$ production cross section, a major intermediate measurement of the experiment, will be measured in the same way. The antiproton, $\overline{H}$ and $\overline{H}^+$ particles can be steered in different directions.

7. $\overline{H}^+$ cooling: in order to evaluate the efficiency of the capture of ions, a first simple test will be to keep them a few ms, and then to eject them axially towards an MCP. In a second step, this detector can be removed in order to detect the fluorescence of beryllium, giving information on the state of the ions. A camera, with its collimation lens in a reentrant window, and a photodetector with collimation lenses under another angle may be used.

16.2   Work sharing

The work sharing is given in Table 9 with the names of the institutes coordinating, and participating in the work packages.

	Work package	Coordination	Participation
1	Production of fast e^+	IRFU	
2	Production of slow e^+	IRFU	Swansea, Tokyo U. of S.
3	e^+ accumulation	RIKEN	IRFU, CSNSM, Swansea
4	Ps formation and excitation	IRFU	LKB, ETHZ
5	$\overline{p}$ deceleration - ELENA interface	CSNSM	U. of Tokyo (Komaba)
6	Production of $\overline{H}$ and $\overline{H}^+$		Tokyo U. of S.
7	$\overline{H}^+$ cooling	LKB	ILL
8	Free fall measurement detector	ETHZ	IRFU
9	Quantum states detection	ILL	Lebedev
10	Slow control and DAQ	IRFU	Swansea

Table 9: Work packages coordination.

16.3   Cost estimate

The cost estimates for the various elements are based on previous applications for funding or on similar experiments, and are summarized in Table 10. R & D costs already obtained, for instance for the demonstrator linac and positron source or positron trap, are not included and amount to 1900 k€. A complementary 15% of the identified costs is added for contingencies bringing the total cost at an estimated 5640 k€.

	Work package	Cost (k€)
1	Production of fast e^+	2000
2	Production of slow e^+	260
3	e^+ accumulation	240
4	Ps formation and excitation	490
5	$\bar{p}$ deceleration - ELENA interface	80
6	Production of $\overline{H}$ and $\overline{H}^+$	200
7	$\overline{H}^+$ cooling	340
8	Free fall measurement detector	500
9	Quantum states detection	300
10	Slow control and DAQ	270
11	Miscellaneous items	220
	Sub Total	4900
	Contingencies	740
	Total	5640

Table 10:   Work packages estimated costs.

16.4   Risk Analysis

The GBAR experiment consists of an assembly of setups, each being based on an extrapolation of existing devices or techniques. Thus, the risks for each element are lowered.

16.4.1   Production of fast positrons

The main parameters required for the Linac are explained in section 4: 10 MeV energy and 0.2 mA average current with $2\,\mu$s pulse length at 300 Hz repetition rate. These parameters have been deduced from a simulation for fast positron production that agrees with the flux measured with our demonstrator. Linacs with such parameters are in the catalog of several firms. Our experience with the SELMA demonstrator has shown that industrial linacs are adequate for the purpose of the experiment. However, close cooperation with the provider must be established, and a detailed reception procedure must be agreed upon. In particular, the slow control of the linac must be compatible with the rest of the experiment, and the beam parameters and stability must all be measurable

at the time of reception. We have now learnt how to proceed along these lines. The help of CERN specialists would of course be useful. A backup solution, in case this new linac is too expensive, would consist in modifying some elements of the present demonstrator, for instance upgrading to a more powerful magnetron, using a solid state modulator and a higher current cathode, and increasing the number of accelerating cells in order to reach an intermediate energy of 7 MeV. The price to pay would be a reduction of a factor 2 in the rate of useful fast positrons. However, manpower will be needed to fulfill such an upgrade, and the linac will not be available for experiments during this work.

The limiting point of the fast positron source is the cooling of the primary target as recently pointed out in [O'Rourke 2011]. The 1 mm thick tungsten target of our demonstrator is cooled with a water flow. It is easily able to sustain the 700 W beam without damage to the tungsten moderator located 1 mm behind it. The temperature of the holder reaches 80°C when running at full power. In fact the primary target acts as a shield for this moderator. The risk seems thus minimal when increasing the beam power to the required 2 kW. An alternative solution to avoid excessive heating is to use a thin target oriented at small angle with respect to the incident beam direction as described in [Pérez 2004].

16.4.2   Production of slow positrons

The question is whether the tungsten moderator will reach a 5×10^{-4} efficiency when the MeV fast positrons are incident upon it. Based on our present experience, we estimate that a 10^{-4} efficiency will be attainable easily. Efficiencies up to 10^{-3} were obtained by Muramatsu et al. [Muramatsu 2005] using a ^{22}Na source. With the MeV positrons from the linac, we estimate that a decrease to an efficiency of 5×10^{-4} is foreseeable by carefully annealing the tungsten meshes after chemical etching.

Solid neon moderators are routinely used with radioactive sources with efficiencies in the $3 - 10 \times 10^{-3}$ range. We suppose that the neon based moderator we will develop will reach an efficiency of 10^{-3}, when including transport losses. It is cooled to 6 K with a 1 W cryocooler. The SOPHI setup was designed specifically in order to reduce the incident power from the electron beam well below 1 W. The major challenge for this moderator is to succeed in adapting the 0.2 T magnetic field from the SOPHI coils to the 10 mT transport beam line while keeping the high efficiency. A careful simulation is thus necessary to assess the transport efficiency. If the transport line were in a magnetic field of 0.2 T, as could be envisaged with high critical temperature superconductors, this problem would be much simplified.

While tungsten meshes or solid neon moderators provide higher efficiencies, the energy distribution of the emitted slow positrons is wider compared to a tungsten foil. This may result in a loss of efficiency to fill the accumulation trap. With a simple buncher as described in section 6.2, the efficiency to obtain a pulse width shorter than the bounce time inside the trap depends on the width of the energy distribution of the slow positrons at the exit of the moderator. A simulation with a 0.7 eV width and a focal point located 13 m downstream of the moderator shows that 70% of the pulse is reduced from $2\,\mu$s to 80 ns, i.e the bounce time in the trap.

In our test facility in Saclay, a 13 m long line operates without problem at 10 mT. However some care must be taken in order to minimize the number of angles in the beam trajectory and discontinuities in the guiding magnetic field since this degrades the beam

quality, which may reduce the efficiency to enter the accumulation Penning trap due to the magnetic mirror present at the entrance of the trap.

16.4.3   Positron accumulation

Penning-Malmberg traps are routinely operated with success to store up to 10^9 positrons [Jorgensen 2005]. For the present project, we will need to store several 10^{10} such particles. The RIKEN trap that is being used in our collaboration was shown to easily confine 2×10^{10} electrons with a lifetime of 4000 s [Mohamed 2008]. The principle of the accumulation of positrons has been tested with a radioactive β^+ source at RIKEN. The extrapolation using a linac shows that this device should be able to accumulate also 2×10^{10} positrons. Such a test is underway at Saclay. In order to obtain higher numbers, it will be necessary to increase the electrode insulation from 3 kV up to 10 kV.

It has been shown that a fast extraction is possible for a plasma of 1.3×10^{10} electrons using a HV pulse on the confining electrodes (see section 6). However when more particles will be confined, it may be more efficient to use a dedicated buncher at the exit of the trap, as demonstrated in [Cassidy 2006]. Such a setup is readily available in the present collaboration and will also be tested.

In the event that this accumulation scheme, using electron cooling, fails, it is possible to adapt the classical Greaves-Surko setup to the pulsed positron beam, using an extra buffer gas trap for cooling such as experienced in ATHENA [Jorgensen 2005] and ALPHA [ALPHA 2010].

16.4.4   Positronium formation and excitation

The $e^+/$ Ps converter solution consisting of the F type of porous silicate (see section 8) has been shown to sustain a positron areal density up to 10 times smaller than the baseline for GBAR. It remains to demonstrate that under the nominal flux the conversion efficiency will stay the same and stable. Laser irradiation may provide a substantial increase in the yield of $\overline{H}^+$ via excitation of Ps. The studies at UCR (section 8) have also shown that the F type converter does not suffer from such irradiation. It will become possible to test these performances at the nominal positron flux for GBAR when more than 10^{10} positrons are confined in the positron trap and ejected in a short pulse at Saclay. A small test facility is under construction there on a beam line extension of the demonstrator positron source. It will provide a test bench for study of other converter types. In the mean time, the ETHZ slow positron beam already used successfully to characterize our converters will remain available.

The lasers for Ps excitation will be tested at the LKB laboratory, and installed first at the exit of the positron accumulation trap in Saclay, where a Ps converter will form a dense Ps target when the positrons are ejected from the trap, allowing systematic studies to be performed.

16.4.5   Antiproton deceleration - ELENA interface

The deceleration of the antiproton bunch from the ELENA beam follows a scheme developed for the SPIRAL1/LIRAT experiment decelerating ^{6}He ions of 20 keV and for the ISOLTRAP experiment at the CERN-ISOLDE facility, where a 60 kV deceleration is needed. The extrapolation to 100 kV seems thus feasible. In case this voltage cannot be

switched in a few tens of nanoseconds, a lower voltage can be accommodated with the rest of the deceleration being obtained by inserting a thin metallic foil as discussed in section 7, at the price of a small loss in the antiproton flux. Such a $\overline{p}$ deceleration setup may be duplicated for similar use on the other ELENA extraction beam lines.

16.4.6 Production of $\overline{H}$ and $\overline{H}^+$

The difficult point here is to accommodate efficient focusing for the positron, antiproton and laser beams at the location of the positronium converter, i.e. a 1 mm diameter, while keeping a low intensity magnetic field. Careful design, based on accurate simulations using standard techniques of beam transport, is needed. Space should be reserved for experiments using the neutral $\overline{H}$ beam, such as for instance in flight spectroscopy of antihydrogen.

16.4.7 $\overline{H}^+$ cooling

The $\overline{H}^+$ bunch capture by a linear RF quadrupole trap has been simulated numerically using the well known SIMION8.0 software. The capture efficiencies do not dramatically depend on the capture trap parameters, so we are confident that the capture process will work with a near 100% efficiency.

$\overline{H}^+$ ions are very fragile ions that can only survive a fraction of a second under excellent vacuum conditions. Using ultra-high vacuum pumping techniques (ion pump, getter pumps, Titanium sublimation pumps, and cryogenic conditions), the pressure will be maintained below the 10^{-11} mb range, so the ions should not undergo collisions during the capture and cooling process.

The sympathetic cooling of initially hot $\overline{H}^+$ ions is one of the main challenges of the project and makes it very interesting for the ion trapper community that is federated in the COST-IOTA action (http://www.cost-iota.org/). Since buffer gas cooling (by collisions) is prohibited in order not to annihilate the $\overline{H}^+$ ions, the only solution to reach μK temperatures is sympathetic cooling using laser pre-cooled Be^+ ions. The long range Coulomb interaction between ions is contact-less and no annihilation is expected. Sympathetic cooling of an ionic species by laser-cooled ions has been observed in many atomic physics laboratories, and applied to molecular ion studies, quantum logic experiments and in the field of optical clocks. Sympathetic cooling times have not been studied systematically. In the case of the above mentioned applications, the ions are created from room temperature atoms with a kinetic energy of about 25 meV, and sympathetically cooled in a few ms. The captured $\overline{H}^+$ ions will have a kinetic energy two or three orders of magnitude larger so that longer cooling times are expected and still have to be evaluated. The LKB group has developed a simulation code taking into account the actual trapping field, the Be^+ laser cooling process and the Coulomb interaction to systematically evaluate the $\overline{H}^+$ sympathetic cooling times as a function of the Be^+ ion cloud properties (ion number, ion cloud shape) and as a function of the initial $\overline{H}^+$ kinetic energy in a near future. From the experimental point of view, the capture and sympathetic cooling process will be first studied and optimized using standard matter, either on H^+, H_2^+ or highly charged ions using standard ion sources to mimic the $\overline{H}^+$ bunch. The knowledge to be acquired during those experiments will fully benefit to the present project.

16.4.8 Free fall measurement detector

The free fall experiment is based on measuring the start and the annihilation times. The event rate is extremely low with respect to usual high energy physics experiments, with very small background. The TPC technology used for the T2K experiment [T2K 2011] is our baseline option at present. Detailed simulations are needed to judge if other techniques such as planes of MicroMegas chambers would be adequate. The expected background from cosmic rays should be easily rejected from reconstruction in the TPC. Thus redundancy in the event signature, for instance with the detection of the 511 keV photons from the two emitted positrons per event, seems unnecessary. On the other hand acceptance and efficiency must be maximized. At present the $\overline{\text{H}}^+$ cooling time is not known and may exceed several seconds. Hence it may prove necessary to use cryogenic vacuum techniques in order to minimize annihilations.

16.4.9 Quantum states detector

The detection of quantum states is based on successful experience at ILL with Ultra Cold Neutrons. The technology to control the surface of the annihilation plate and its vibrations is well established. This plate must be located about $50\,\mu$m below the location of the $\overline{\text{H}}^+$ ion at rest. In order to limit the loss in statistics because of solid angle coverage, the plate must be very close to the ion. Techniques already used with UCN may prove even easier with the neutral $\overline{\text{H}}$ atom, by taking advantage of the quantum reflection process right after photodetachment of the ion, i.e. when the atom is still very slow.

16.5   Schedule and Milestones

Table 11 shows a rough schedule for the different work packages assuming a start of the project in 2012. The end of each work package is marked by a milestone that is recalled in the description below.

1. The Linac is installed at its final location in the AD hall and fully operational, i.e. including concrete shielding, regulated water cooling and ozone extraction. This step will be preceded by measurements of the Linac parameters, such as the energy spectrum and beam intensity at nominal repetition rate. The target assembly, including the tungsten moderator holder is included in a vacuum chamber next to the Linac beam pipe.

2. After the choice for the best solution for positron moderation, for instance, between tungsten meshes or solid neon, the rate, energy spectrum and beam emittance of slow positrons is measured at the end of the transport line, i.e. outside the concrete shielding of the linac.

3. After successful tests at Saclay of the e^+ accumulation scheme with several 10^{10} stored e^+ and further development of positronium target formation and excitation, the trap and target are installed at CERN and connected to the slow e^+ beam line.

4. The density of the positronium target is measured with a value of $\approx 10^{12}$ cm$^-$3. Its excitation to the 3D level is obtained.

5. After tests on an ion beam line, the $\overline{\text{p}}$ deceleration setup is installed on the ELENA extraction beam line. Antiproton beam parameters are measured.

6. Installation at CERN of the reaction chamber. Positronium formation and excitation is checked. $\overline{\text{H}}$ and $\overline{\text{H}}^+$ production cross sections are measured.

7. $\overline{\text{H}}^+$ cooling techniques are first tested with H_2^+ ions in the LKB laboratory. Then installation in the detection chamber follows at CERN. $\overline{\text{H}}^+$ is captured, cooled and the proof of crystallization is obtained through visualization of the atom spot position.

8. Detectors are tested with cosmic rays and possibly existing beams before assembly around the detection chamber. The first stage of the free fall experiment can be performed.

9. Quantum states detection will be undertaken if systematic effects limit the precision of the simple free fall method.

10. After global conception of the slow control and DAQ, each step of the build-up of the apparatus is monitored.

Schedule Gantt chart (█ = dark blue, ░ = light blue / long term prospect):

	2012 S1	2012 S2	2013 S1	2013 S2	2014 S1	2014 S2	2015 S1	2015 S2	2016 S1	2016 S2	2017 S1	2017 S2
WP - 1 Production of fast e$^+$												
Design specification and tender	█	█										
Reception at CERN					█							
Operation						█	█	█	█	█	█	█
WP - 2 Production of slow e$^+$												
Design specification and tender	█	█										
Qualification and testing			█	█	█							
CERN installation						█						
Operation							█	█	█	█	█	█
WP - 3 e$^+$ accumulation												
R&D work	█	█	█	█								
Qualification and testing					█							
CERN installation						█						
Operation							█	█	█	█	█	█
WP - 4 Ps formation and excitation												
R&D work	█	█	█	█	█							
CERN installation							█					
Operation								█	█	█	█	█
WP - 5 $\overline{p}$ deceleration - ELENA interface												
Design specification and tender		█	█									
Qualification and testing				█	█	█						
CERN installation							█					
Operation								█	█	█	█	█
WP - 6 Production of $\overline{\overline{H}}$ and $\overline{\overline{H}}^+$												
R&D work	█	█										
Design specification and tender			█	█								
Qualification and testing					█	█	█	█	█			
CERN installation										█		
Operation											█	█
WP - 7 $\overline{H}^+$ cooling												
R&D work	█	█	█	█	█	█	█	█	█	█		
CERN installation											█	
Operation												█
WP - 8 Free fall measurement detector												
R&D work	█	█	█	█								
Design specification and tender			█	█								
Qualification and testing						█	█	█	█			
CERN installation										█		
Operation											█	█
WP - 9 Quantum states detection												
R&D work	█	█	█	█	█	█	█					
Qualification and testing					█	█	█	█	█	█		
CERN installation											░	
Operation												░
WP - 10 Slow control and DAQ												
Design specification and tender	█	█	█	█								
Qualification and testing					█	█	█	█				
Operation									█	█	█	█

Table 11: Schedule (S1 and S2 represent semesters; light blue is for the long term prospect).

References

[AEGIS 2007] AEGIS collaboration. *Proposal for the AEGIS experiment at the Cern Antiproton Decelerator (Antimatter Experiment: Gravity, Interferometry, Spectroscopy)*, CERN-SPSC-2007-017.

[AIRIX 1993] J. de Mascureau et al., *Diagnostics development for high current electron accelerators at CESTA*, Proceedings of the 1993 IEEE Particle Accelerator Conference, 2115 (1993).

[ALPHA 2010] G.B. Andresen et al., *Trapped antihydrogen*, Nature **468** (,) 2010673.

[Amoretti 2004] M. Amoretti et al., *The ATHENA antihydrogen apparatus*, Nucl. Inst. Meth. B **518** (,) 2004679.

[Andresen 2008] G.B. Andresen et al., *Compression of antiproton clouds for antihydrogen trapping*, Phys. Rev. Lett. **100** (,) 2008203401.

[ASACUSA 2010] Y. Enomoto et al., *Synthesis of cold antihydrogen in a cusp trap*, Phys. Rev. Lett. **105** (,) 2010243401.

[Baba 2002] T. Baba, I. Waki, *Sympathetic cooling rate of gas-phase ions in a radio-frequency-quadrupole ion trap*, Appl. Phys. B **74**, (2002) 375.

[Baessler 2009] S. Baessler, *Gravitationally bound quantum states of ultracold neutrons and their applications*, J. Phys. G **36**, (2009) 104005.

[Baessler 2011] S. Baessler, M. Beau, M. Kreuz, V.N. Kurlov, V.V. Nesvizhevsky, G. Pignol, K.V. Protasov, F. Vezzu, A.Yu. Voronin, *The GRANIT spectrometer*, Compt. Rend. Acad. Sci., accepted (2011).

[Barnard 2008] J. Barnard, V.V. Nesvizhevsky, *Analysis of a method for extracting angularly collimated UCNs from a volume without losing density inside*, Nucl. Instrum. Meth. A **591**, (2008) 431.

[Barrett 2003] M. D. Barrett, B. DeMarco, T. Schaetz, V. Meyer, D. Leibfried, J. Britton, J. Chiaverini, W. M. Itano, B. Jelenkovic, J. D. Jost, C. Langer, T. Rosenband, D. J. Wineland, *Sympathetic cooling of $^9Be^+$ and $^{24}Mg^+$ for quantum logic*, Phys. Rev. A **68**, 042302 (2003).

[Benhelm 2008] Jan Benhelm, Gerhard Kirchmair, Christian F. Roos, Rainer Blatt, *Towards fault-tolerant quantum computing with trapped ions*, Nature Phys. **4**, 463 (2008).

[Blythe 2005] P. Blythe, B. Roth, U. Fröhlich, H. Wenz, S. Schiller, *Production of ultracold trapped hydrogen molecular ions*, Phys. Rev. Lett. **95**, 183002 (2005).

[Bordag 2001] M. Bordag, U. Mohideen, V.M. Mostepanenko, *New developments in the Casimir effect*, Phys. Rep. **353**, (2001) 1.

[Bussmann 2006] M. Bussmann, U. Schramm, D. Habs, V.S. Kolhinen, J. Szerypo, *Stopping highly charged ions in a laser-cooled one component plasma of $^{24}Mg^+$ ions*, Int. J. Mass. Spectrom. **251**, 179 (2006).

[Canaguier 2011] A. Canaguier-Durand et al, *Casimir interaction between a dielectric nanosphere and a metallic plane*, Phys. Rev. A **83**, (2011) 032508.

[Casimir 1948] H.B.G. Casimir, D. Polder, *The influence of retardation of the London-van der Waals forces*, Phys. Rev. **73**, (1948) 360.

[Cassidy 2006] D.B. Cassidy, S.H.M. Deng, R.G. Greaves and A.P. Mills, Jr *Accumulator for the production of intense positron pulses*, Rev. Sci. Instrum. **77**, (2006) 073106.

[Cassidy 2008] D. B. Cassidy and A. P. Mills *Interactions between positronium atoms in porous silica*, Phys. Rev. Lett. **100**, (2008) 013401.

[Cassidy 2010] D. B. Cassidy, P. Crivelli, T. H. Hisakado, L. Liszkay, V. E. Meligne, P. Perez, H. W. K. Tom and A. P. Mills, Jr. *Positronium cooling in porous silica measured via Doppler spectroscopy*, Phys. Rev. A **81**, (2010) 012715, D. B. Cassidy SLOPOS-12 (1-6 August 2010 Magnetic Island, Australia).

[Cassidy 2011] D. B. Cassidy, T. H. Hisakado, H. W. K. Tom, and A. P. Mills, Jr., *Photoemission of positronium from Si*, Phys. Rev. Lett. **107**, (2011) 033401.

[Chandrasekhar 1958] S. Chandrasekhar, D. D. Elbert, *On the continuous absorption coefficient of the negative hydrogen ion*, Astrop. J. **128**, (1958) 633.

[Chen 1985] D. M. Chen, K. G. Lynn, R. Pareja, B. Nielsen, *Measurement of positron reemission from thin single-crystal W(100) crystals*, Phys. Rev. B **31**, (1985) 4123.

[Church 1969] D.A. Church, H. G. Dehmelt, *Radiative cooling of an electrodynamically contained proton gas*, J. Appl. Phys. **40**, (1969) 3421.

[CPLEAR 1999] CP LEAR collaboration, *Tests of the Equivalence Principle with neutral kaons*, Phys. Lett. B**452**, (1999) 425.

[Crance 1985] M. Crance, M. Aymar, *Two-photon detachment of H^-,. A model calculation*, J. Phys. B: At. Mol. Phys **18**, (1985) 3529.

[Crivelli 2010] P. Crivelli, U. Gendotti, A. Rubbia, L. Liszkay, P. Perez, C. Corbel *Measurement of the orthopositronium confinement energy in mesoporous thin films*, Phys. Rev. A **81**, (2010) 052703.

[Denison 1971] D. R. Denison, *Operating parameters of a quadrupole in a grounded cylindrical housing*, J. Vac. Sci. Tech. **8**, (1971) 266.

[Diedrich 1989] F. Diedrich, J. C. Bergquist, W. M. Itano, D. J. Wineland, *Laser cooling to the zero-point energy of motion*, Phys. Rev. Lett. **62**, (1989) 403.

[Dubessy 2010] R. Dubessy,*Réalisation, étude et exploitation d'ensembles d'ions refroidis par laser stockés dans des pièges micro-fabriqués pour l'information quantique*, PhD thesis, Université Paris-Diderot, 12 Octobre 2010.

[Dzyaloshinskii 1960] I.E. Dzyaloshinskii, E.M. Lifshitz, L.P. Pitaevskii, *The general theory of van der Waals forces*, Adv. Phys. **10**, (1960) 165.

[Ebel 1987] F. Ebel, W. Faust, C. Hahn, S. Langer, H. Schneider, *Production of positrons with the Giessen 65 MeV LINAC*, Appl. Phys A **44**, (1987) 119.

[Eriksson 2010] T. Eriksson et al., *ELENA - An Updated Cost and Feasability Study*, CERN-BE-2010-29 OP.

[Fojón 1996] O. A. Fojón, R. D. Rivarola, R. Gayet, J. Hanssen and P. A. Hervieux, *Continuum-distorted-wave-final-state-approximation in positron-hydrogenic atom (ion) collisions with positronium formation*, Phys. Rev. A **54**, (1996) 4923.

[Fojón 1997] O. A. Fojón, R. D. Rivarola, R. Gayet, J. Hanssen and P. A. Hervieux, *High-energy positronium formation in positron-hydrogenic ion collisions: scaling laws*, J. Phys. B **30**, (1997) 2199.

[Fojón 1998] O. Fojón, J. Hanssen, P. -A. Hervieux, R. Rivarola and R. Gayet, *Inner-shell contribution to electron capture in positron-alkali collisions*, J. Phys. B **31**, (1998) 1313.

[Fojón 2001] O. Fojón, R. Rivarola, J. Hanssen and P. -A. Hervieux, *Positronium formation in positron-simple metal cluster collisions*, J. Phys. B **34**, (2001) 4279.

[Fojón 2002] O. A. Fojón, R. D. Rivarola, J. Hanssen and P. -A. Hervieux, Photonic Electronic and Atomic Collisions (XXII ICPEAC)Proceedings, Rinton Press (2002)

[Friedrich 2002] H. Friedrich, G. Jacoby, C.G. Meister, *Quantum reflection by Casimir - van der Waals potential tails*, Phys. Rev. A **65**, (2002) 032902.

[Gabrielse 1986] G. Gabrielse et al., *First capture of antiprotons in a Penning trap: a kiloelectronvolt source*, Phys. Rev. Lett. **57**, (1986) 2504.

[Gabrielse 1999] G. Gabrielse et al., *Precision mass spectroscopy of the antiproton and proton Using simultaneaously trapped particles*, Phys. Rev. Lett. **82**, (1999) 3198.

[Gabrielse 2011] G. Gabrielse et al., *Adiabatic cooling of antiprotons*, Phys. Rev. Lett. **106**, (2011) 073002.

[Ganic 2002] D. Ganic, Gan Xiaosong, Gu Min, M.Hain, S. Somalingam, S. Stankovic, T. Tschudi, *Generation of doughnut laser beams by use of a liquid-crystal cell with a conversion efficiency near 100%.* Optics Letters **27**, 1351 (2002).

[Gérardin 2011] A. Gérardin, R. Guérout, A. Lambrecht, V.V. Nesvizhevsky, S. Reynaud, A.Yu. Voronin, *Quantum reflection of antihydrogen on a material surface*, to be submitted (2011).

[Gerola 1995] D. Gerola, W. B. Waeber, M. Shi, and S. J. Wang, *Quasidivergency-free extraction of a slow positron beam from high magnetic fields*, Rev. Sci. Instrum. **66**, (1995) 3819.

[Gidley 1999] D. W. Gidley, W. E. Frieze, T. L. Dull, A. F. Yee, E. T. Ryan, H.-M. Ho *Positronium annihilation in mesoporous thin films*, Phys. Rev. B **60**, (1999) 5157.

[Gidley 2001] D. W. Gidley, K. G. Lynn, M. P. Petkov, M. H. Weber, J. N. Sun, A. F. Yee, *Depth-profiled positron lifetime spectroscopy of thin insulation films*, In New Directions in Antimatter Chemistry and Physics, ed. CM Surko, FA Gianturco, pp. 151-71. Dordrecht, The Netherlands: Kluwer Acad. Publ.

[Gontier 1971] Y. Gontier and M. Trahin, *On the multiphoton absorption in atomic hydrogen*, Phys. Lett. **36A**, (1971) 463.

[Hall 1968] J.L. Hall and M.W. Siegel, *Angular dependence of the laser photodetachment of the negative ions of carbon, oxygen and hydrogen*, J. Chem. Phys. **48**, (1968) 943.

[Hanssen 2000] J. Hanssen, P. -A. Hervieux, O. Fojón and R. Rivarola, *Transfer excitation in collisions of positrons with He and alkaline-earth metals*, J. Phys. B **33**, (2000) 3093.

[Hanssen 2001] J. Hanssen, P. -A. Hervieux, O. Fojón and R. Rivarola, *Positronium formation in positron-metastable-helium collisions*, Phys. Rev. A **63**, (2001) 012705.

[Heinzen 1990] D.J. Heinzen, D.J. Wineland, *Quantum-limited cooling and detection of radio-frequency oscillations by laser cooled ions*, Phys. Rev. A **42**, (1990) 2977.

[Herfurth 2001] F. Herfurth et al., *A linear radio frequency ion trap for accumulation, bunching and emittance improvement of radioactive ion beams*, Nuc. Inst. Meth. in Physics Research A **469**, (2001) 254.

[Hervieux 2006] P. -A. Hervieux, O. Fojón, C. Champion, R. D. Rivarola and J. Hanssen, *Positronium formation in collisions of fast positrons impacting on vapour water molecules*, J. Phys. B **39**, (2006) 409.

[Higaki 2002] H. Higaki et al., *Electron cooling of high energy protons in a multiring trap with a tank circuit monitoring the electron-plasma oscillations*, Phys. Rev. E **65**, (2002) 046410.

[Howell 1982] R. H. Howell, R. A. Alvarez, and M. Stanek, *Production of slow positrons with a 100-MeV electron linac*, Appl. Phys. Lett. **40**, (1982) 751.

[Howell 1987] R. H. Howell, I. J. Rosenberg, M. J. Fluss, *Production and use of low-energy, monoenergetic positron beams from electron linacs*, Appl. Phys. A **43**, (1987) 247.

[Huang 1997] X.-P. Huang et al, *Steady-state confinement of non-neutral plasmas by rotating electric fields*, Phys. Rev. Lett. **78**, (1997) 875.

[Hucul 2008] D. Hucul, M. Yeo, S. Olmschenk, C. Monroe, W. K. Hensinger, J. Rabchuk, *On the transport of atomic ions in linear and multidimensional ion trap arrays*, Quantum Information and Quantum Computation **8**, (2008) 501.

[Hulett 1989] L. D. Hulett, Jr, T. A. Lewis, D. L. Donohue, S. Pendyala, in "Positron Annihilation", Proc. ICPA-8 (World Scientific, Singapore 1989), p.586

[Humberston 1987] J.W. Humberston, M. Charlton, F.M. Jacobsen, and B.I. Deutch, *Antihydrogen formation in collisions of antiprotons with positronium*, J. Phys. B **20**, (1987) L25.

[Jorgensen 2005] L.V. Jørgensen et al., *New source of dense, cryogenic positron plasmas* Phys. Rev. Lett. **95**, (2005) 025002.

[Kadyrov 2002] A.S. Kadyrov and I. Bray, *Two-center convergent close-coupling approach to positron-hydrogen collisions*, Phys. Rev. A **66**, (2002) 012710.

[Kuppens 1998] S. Kuppens, M. Rauner, M. Schiffer, K. Sengstock, W. Ertmer, F.E. van Dorsselaer, G. Nienhuis, *Polarization-gradient cooling in a strong doughnut-mode dipole potential.* Phys. Rev. A **58**, (1998) 3068.

[Kuroda 2005] N. Kuroda et al., *Confinement of a large number of antiprotons and production of an ultra-slow antiproton beam*, Phys. Rev. Lett. **94**, (2005) 023401.

[Kuroda 2008] N. Kuroda et al., *Radial compression of an antiproton cloud for production of intense antiproton beams*, Phys. Rev. Lett. **100**, (2008) 203402.

[Kuroda 2010] N. Kuroda et al., *Development of MUSASHI, a mono-energetic ultra-slow antiproton beam source* proceedings of IPAC 2010 (2010) THPEC058

[Larson 1986] *Sympathetic cooling of trapped ions: A laser-cooled two-species nonneutral ion plasma.* D.J. Larson, J.C. Bergquist, J.J. Bollinger, W.M. Itano, D.J. Wineland, Phys. Rev. Lett. **57**, (1986) 70.

[Lennard 1932] J.E. Lennard-Jones, *Processes of adsorption and diffusion on solid surfaces*, Trans. Faraday Soc. **28**, (1932) 333.

[Ley 1985] R. Ley, K. D. Niebling, A. Osipowics, A. Picard, G. Werth, in "Positron Annihilation", Proc. ICPA-7 (World Scientific, Singapore 1985), p.996

[Liszkay 2008] L. Liszkay et al. *Positronium reemission yield from mesostructured silica films*, Appl. Phys. Lett. **92**, (2008).

[Liszkay 2009] L. Liszkay, C. Corbel, L. Raboin, J.-P. Boilot, P. Perez, A. Brunet-Bruneau, P. Crivelli, U. Gendotti, A. Rubbia, T. Ohdaira, R. Suzuki*Mesoporous silica films with varying porous volume fraction: Direct correlation between ortho-positronium annihilation decay and escape yield into vacuum*, Appl. Phys. Lett. **95**, (2009) 124103.

[Liszkay 2010] L. Liszkay,*Positronium for antihydrogen production* page 297 in: Physics With many Positrons, Proceedings of the International School of Physics "Enrico Fermi", course CLXXIV, edited by A. Dupasquier, A. P. Mills, Jr., R. S. Brusa, IOS Press, Amsterdam, Oxford, Tokyo, Washington DC, 2010.

[Lunney 2009] D. Lunney et al., *COLETTE a linear Paul-trap beam cooler for the on-line mass spectrometer MISTRAL*, Nuc. Inst. Meth. in Physics Research A **598**, (2009) 379.

[Lykke 1991] K.R. Lykke, K.K. Murray, W.C. Lineberg, *Threshold photodetachment of H⁻*, Phys. Rev. A **43**, (1991) 6104.

[Mariazzi 2008] S. Mariazzi, A. Salemi, R. S. Brusa *Positronium cooling into nanopores and nanochannels by phonon scattering* Phys. Rev. B **78**, (2003) 085428.

[Merrison 1997] J.P. Merrison et al., *Hydrogen formation by proton impact on positronium*, Phys. Rev. Lett., **78**, (1997) 2728

[Messina 2009] R. Messina et al, *Dispersive interactions between atoms and nonplanar surfaces*, Phys. Rev. A **80,** (2009) 022119.

[Mills 2002] A.P. Mills, M. Leventhal, *Can we measure the gravitational free fall of cold Rydberg state positronium?*, Nucl. Inst. Meth. in Physics Research B **192**, (2002) 102.

[Mills 1985] A. P. Mills, Jr., L. Pfeiffer, *Velocity spectrum of positronium thermally desorbed from an Al(111) surface* Phys. Rev. B **32**, (1985) 53.

[Mitroy 1994] J. Mitroy and A.T. Stelbovics, *Formation of antihydrogen from antiproton collisions with positronium*, J. Phys. B: At. Mol. Opt. Phys. **27**, (1994) L79.

[Mitroy 1995] J. Mitroy, *Formation of antihydrogen by the charge-transfer reaction*, Phys. Rev. A **52**, (1995) 2859.

[Miyamoto 1980] K. Miyamoto, *Plasma Physics for nuclear fusion*, Publisher MIT, Cambridge, MA (1980)

[Mohamed 2008] T. Mohamed, *Successful production of non-neutral electron plasma of high density in the multi-ring trap*, Plasma Devices and Operations **16**, (2008) 181.

[Mohamed 2011] T. Mohamed, H. Imao, N. Oshima, A. Mohri, Y. Yamazaki, *Fast electron accumulation and its mechanism in a harmonic trap under ultrahigh vacuum conditions*, Phys. Plasmas, **18** (2011) 032507.

[Mohri 1998] A. Mohri et al., *Confinement of Nonneutral Spheroidal Plasmas in Multi-Ring Electrode Traps*, Jpn. J. Appl. Phys., **37**, (1998) 664.

[Mohri 2002] A. Mohri et al., Europhys. Conf. Abstr. 26B (2002) paper 2.033

[Moler 1992] K. Moler, D. S. Weiss, M. Kasevich, S. Chu, *Theoretical analysis of velocity-selective Raman transitions.* Phys. Rev. A **45**, 342 (1992).

[Monroe 1995] C. Monroe, D. M. Meekhof, B.E. King, S.R. Jefferts, W. M. Itano, D. J. Wineland, *Resolved-sideband Raman cooling of a bound atom to the 3D zero-point energy.* Phys. Rev. Lett. **75**, 4011 (1995).

[Muons, Inc] Muons, Inc., Innovation in Research, 552 N. Batavia Avenue, Batavia, IL 60510, http://www.muonsinc.com/

[Muramatsu 2005] M. Muramatsu, T Ohdaira and R. Suzuki, *Reemission of Positrons from Mesh and Powder Moderators*, Jpn. J. Appl. Phys. **44**, (2005) 6283.

[Nagashima 1995] Y. Nagashima et al. *Thermalization of free positronium atoms by collisions with silica-powder grains, aerogel grains, and gas molecules* Phys. Rev. A **52**, (1995) 258.

[Nagashima 1998] Y. Nagashima Y, Morinaka Y, Kurihara T, Y. Nagai, T. Hyodo, T. Shidara, K. Nakahara *Origins of positronium emitted from SiO_2*, Phys. Rev. B **58**, (1998) 12676.

[Nesvizhevsky 2002] V.V. Nesvizhevsky, H.G. Börner, A.K. Petukhov, H. Abele, S. Baessler, F.J. Ruess, Th. Stöferle, A. Westphal, A.M. Gagarski, G.A. Petrov, A.V. Strelkov, *Quantum states of neutrons in the Earth's gravitational field*, Nature **415**, (2002) 297.

[Nesvizhevsky 2003] V.V. Nesvizhevsky, H.G. Börner, A.M. Gagarski, A.K. Petukhov, G.A. Petrov, H. Abele, S. Baessler, G. Divcovic, F.J. Ruess, Th. Stöferle, A. Westphal, A.V. Strelkov, K.V. Protasov, A.Yu. Voronin, *Measurement of quantum states of neutrons in the Earth's gravitational field*, Phys. Rev. D **67**, (2003) 102002.

[Nesvizhevsky 2005] V.V. Nesvizhevsky, A.K. Petukhov, H.G. Börner, T.A. Baranova, A.M. Gagarski, G.A. Petrov, K.V. Protasov, A.Yu. Voronin, S. Baessler, H. Abele, A. Westphal, L. Lucovac, *Study of the neutron quantum states in the gravity field*, Europ. Phys. J. C **40**, (2005) 479.

[Nesvizhevsky 2010] V.V. Nesvizhevsky, *Near-surface quantum states of neutrons in the gravitational and centrifugal potentials*, Physics-Uspekhi **53**, (2010) 645.

[Nieto 1991] Nieto and T. Goldman. *The arguments against antigravity and the Gravitational Acceleration of Antimatter*, Phys. Rep. **205**, (1991), 221.

[O'Rourke 2011] B. E. O'Rourke, N. Hayashizaki, A. Kinomura, R. Kuroda, E. J. Minehara, T. Ohdaira, N. Oshima, and R. Suzuki, *Simulations of slow positron production using a low-energy electron accelerator*, Rev. Sci. Inst. **82**, (2011) 063302.

[Oshima 2000] N. Oshima et al., *A new positron accumulator with electron plasma*, Riken Review **31**, (2000) 65.

[Oshima 2003] N. Oshima et al., *Development of a cold HCI source for ultra-slow collisions*, Nucl. Inst. Meth. B **205,** (2003) 178.

[Oshima 2004] N. Oshima et al., *New scheme for positron accumulation in ultrahigh vacuum*, Phys. Rev. Lett. **93**, (2004) 195001.

[Pakvasa 1989] S. Pakvasa, W. Simmons, T. Weiler. *Test of equivalence principle for neutrinos and antineutrinos*, Phys. Rev. D **39**, (1989) 1761.

[Paridaens 1990] J. Paridaens, D. Segers, M. Dorikens, L. Dorikens-Vanpraet, *Pulse stretching at the linac-based slow-positron beam of the Ghent University*, Nucl. Inst. Meth. A**287** (,) 1990359 and Nucl. Inst. Meth. A**295** (,) 199039.

[Pasquini 2004] T.A. Pasquini et al, *Quantum reflection from a solid surface at normal incidence*, Phys. Rev. Lett. **93**, (2004) 223201.

[Pérez 2004] P. Pérez and A. Rosowsky, *Intense source of slow positrons*, Nucl. Inst. Meth. A **532**, (2004) 523.

[Pérez 2005] P. Pérez and A. Rosowsky, *A new path toward gravity experiments with antihydrogen*, Nucl. Inst. Meth. A **545,** (2005) 20.

[Pérez 2007] P. Pérez et al. *A new path to measure antimatter free fall*, CERN-SPSC-2007-038, CERN-SPSC-I-237, December 2007

[Pérez 2007-2] P. Pérez et al., Proceedings of the Eleventh International Workshop on Slow Positron Beam Techniques for Solids and Surfaces, Orléans, France, 9-13 July 2007, M-F. Barthe and C. Corbel (Eds.)

[Pérez 2008] P. Pérez et al., *A Scheme to Produce a Dense Positronium Plasma for an Antihydrogen Experiment*, Appl. Surf. Sci. **255**, (2008) 1, P. Pérez et al., *A scheme to produce the antihydrogen ion $\bar{H}^+$ for gravity measurements*, AIP Conference Proceedings Volume 1037, Proceedings of the Workshop on Cold Antimatter Plasmas and Application to Fundamental Physics, Okinawa, Japan, 20-22 February 2008, Y. Kanai and Y. Yamazaki (Eds.).

[Pérez 2010] P. Pérez et al., ANR Programme Blanc, projet POSITRAP, 2010.

[Rohde 2001] H. Rohde, S. T. Gulde, C. F. Roos, P. A. Barton, D. Leibfried, J. Eschner, F. Schmidt-Kaler and R. Blatt, *Sympathetic ground-state cooling and coherent manipulation with two-ion crystals.*, J. Opt. B **3**, S34 (2001).

[Rosenband 2008] T. Rosenband, D. B. Hume, P. O. Schmidt, C. W. Chou, A. Brusch, L. Lorini, W. H. Oskay, R. E. Drullinger, T. M. Fortier, J. E. Stalnaker,. S. A. Diddams, W. C. Swann, N. R. Newbury, W. M. Itano, D. J. Wineland, J. C. Bergquist, *Frequency ratio of Al^+ and Hg^+ single-ion optical clocks; metrology at the 17th decimal place.*, Science **319**, 1808 (2008).

[Roy 2008] S. Roy and C. Sinha, *Formation of negative hydrogen ion in positronium-hydrogen collisions*, Eur. Phys. J. D **47**, (2008) 327.

[Saito 1999] H. Saito, T. Hyodo, *Quenching of positronium by surface paramagnetic centers in ultraviolet- and positron-irradiated fine oxide grains*, Phys. Rev. B **60**, (1999) 11070.

[Saito 2002] F. Saito, Y. Nagashima, L. Wei, Y. Itoh, A. Goto, *A high-efficiency positron moderator using electro-polished tungsten meshes*, Appl. Surf. Sci. **194**, (2002) 13.

[J. Scherk 1979] J. Scherk, *Antigravity: a crazy idea?*, Phys. Lett. B**88**, (1979) 265.

[L.R. Scherk 1979] L.R. Scherk, *An improved value for the electron affinity of the negative hydrogen ion*, Canadian Journal of Physics **57**, (1979) 558.

[Schiller 2007] S. Schiller, *Hydrogenlike highly charged ions for tests of the time independence of fundamental constants*, Phys. Rev. Lett. **98**, (2007) 180801.

[Schiller web] http://www.exphy.uni-duesseldorf.de/

[Schmidt 2005] P. O. Schmidt, T. Rosenband, C. Langer, W. M. Itano, J. C. Bergquist, D. J. Wineland, *Spectroscopy using quantum logic.*, Science **309**, (2005) 749.

[Schnitzler 2002] H. Schnitzler, U. Fröhlich, T.K.W. Boley , A.E.M. Clemen, J. Mlynek, A. Peters, S. Schiller, *All-solid-state tunable continuous-wave ultraviolet source with high spectral purity and frequency stability*, Appl. Opt. **41**, (2002) 7000.

[Shimizu 2001] F. Shimizu, *Specular reflection of very slow metastable Neon atoms from a solid surface*, Phys. Rev. Lett. **86**, (2001) 987.

[Schultz 1988] P. J. Schultz, K. G. Lynn *Interaction of positron beams with surfaces, thin films and interfaces* Rev. Mod. Phys. **60**, (1988) 701.

[Sivukhin 1966] D. Sivukhin, Review of Plasma Physics, Vol. 4, edited by A.M. Leontovich (Consultants Bureau, New York, 1966).

[Smith 1959] S. J. Smith, D. S. Burch, *Photodetachment cross section of the negative hydrogen ion*, Phys. Rev. Lett. **2**, (1959) 165.

[Soininen 1991] E. Soininen, A. Schwab, K. G. Lynn *Positron-induced Auger-electron study of the Ge(100) surface - Positron thermal desorption and surface condition*, Phys. Rev. B **43**, (1991) 10051.

[Stoeffl 1999] W. Stoeffl, P. Asoka-Kumar, and R. Howell, *The positron microprobe at LLNL*, Appl. Surf. Sci. **149**, (1999) 1.

[Suzuki 1998] R. Suzuki, T. Ohdaira, A. Uedono, Y. Koo Cho, S. Yoshida, Y. Ishida, T. Ohshima, H. Itoh, M. Chiwaki, T. Mikado, T. Yamazaki, S. Tanigawa, *Investigation of Positron Moderator Materials for Electron-Linac Based Slow Positron Beamlines*, Jpn. J. Appl. Phys. **37**, (1998) 4636.

[Tanaka 1991] H. Tanaka and T. Nakanishi, *Slow positron production using an 18 MeV electron linac*, Nucl. Inst. Meth. B **62,** (1991) 259.

[T2K 2011] *Time projection chambers for the T2K near detectors*, N. Abgrall et al., Nucl. Inst. Meth. A **637**, (2011) 25.

[Vasilyev 2011] S. Vasilyev, A. Nevsky, I. Ernsting, M. Hansen, J. Shen, S. Schiller *Compact all-solid-state continuous-wave single-frequency UV source with frequency stabilization for laser cooling of Be^+ ions*, Appl. Phys. B **103**, (2011) 27.

[Voronin 2005-1] A.Yu. Voronin, P. Froelich, B. Zygelman, *Interaction of ultracold antihydrogen with a conducting wall*, Phys. Rev. A **72**, (2005) 062903.

[Voronin 2005-2] A.Yu. Voronin, P. Froelich, *Quantum reflection of ultracold antihydrogen from a solid surface*, J. Phys. B **38**, (2005) 301.

[Voronin 2011] A.Yu. Voronin, P. Froelich, V.V. Nesvizhevsky,*Gravitational quantum states of antihydrogen*, Phys. Rev. A **83**, (2011) 032903.

[Wagstaff 1979] *A second-harmonic, ring dye laser for the generation of continuous-wave, single-frequency UV radiation.* C.E. Wagstaff, M.H. Dunn, J. Phys D. **12**, (1979) 355.

[Walz 2004] J. Walz and T. Hänsch. *A proposal to measure antimatter gravity using ultracold antihydrogen atoms*, General Relativity and Gravitation **36**, (2004) 561.

[Weber 2010] T. R. Weber, J. R. Danielson, and C. M. Surko, *Electrostatic beams from tailored plasmas in a Penning-Malmberg trap*, Phys. Plasmas **17**, (2010) 123507.

[Weber 2011] T. R. Weber, J. R. Danielson, and C. M. Surko, *Electrostatic beams from a 5 T Penning-Malmberg trap*, Rev. Sci. Inst. **82**, (2011) 016104.

[Wilson 2011] A. C. Wilson, C. Ospelkaus, A. P. VanDevender, J. A. Mlynek, K. R. Brown, D. Leibfried, D. J. Wineland, *A 750 mW, continuous-wave, solid-state laser source at 313 nm for cooling and manipulating trapped 9Be+ ions*, arXiv:1105.5356.

[Wu 2007] Y. C. Wu, Y. Q. Chen, S. L. Wu, Z. Q. Chen, S. J. Wang, R. G. Greaves, *High moderation efficiency positron beamline*, Physica Status Solidi C **4**, (2007) 4032.

[Yu 2003] R. S. Yu, T. Ohdaira, R. Suzuki, K. Ito, K. Hirata, K. Sato, and Y. Kobayashi, Jun Xu *Positronium time-of-flight measurements of porous low-k films*, Appl. Phys. Lett. **83**, (2003) 4966.